Modeling of localized deformation in high and ultra-high performance fiber reinforced cementitious composites

by

Marta Miletić

B.S., University of Zagreb, 2009
M.S., University of Zagreb, 2011

AN ABSTRACT OF A DISSERTATION

submitted in partial fulfillment of the requirements for the degree

DOCTOR OF PHILOSOPHY

Department of Civil Engineering
College of Engineering

KANSAS STATE UNIVERSITY
Manhattan, Kansas

2016

Abstract

A low ratio between the compressive strength of concrete and its cost makes concrete one of the most widely used construction materials in civil engineering. Despite of a very good response to compressive stress, concrete exhibits a low tensile strength and limited tensile strain capacity. Adding short discrete fibers to a cementitious matrix can significantly improve its performance under tensile stress, thus ultimately exhibiting a ductile behavior. Nevertheless, in spite of their beneficial properties fiber reinforced cementitious composites remain underutilized in engineering practice. One of the main reasons for this is a lack of an adequate characterization of the tensile behavior as well as a lack of analysis methods that would allow engineers to incorporate fiber reinforced structural concrete elements into their design. Therefore, this dissertation has four key objectives: 1) to computationally model a stress-strain response of high performance fiber reinforced cementitious composites in uniaxial tension and uniaxial compression prior to macro-crack localization, 2) to develop and perform a diagnostic strain localization analysis for high performance fiber reinforced cementitious composites, the results of which can characterize effects of fibers on failure precursors, 3) to devise and perform an experimental program for characterization of ultra-high performance fiber reinforced cementitious composites, and 4) to characterize a full-fledged behavior including stress-strain and stress-crack opening displacement responses of ultra-high performance fiber reinforced cementitious composites in uniaxial tension.

To quantify effects of fibers on onset of strain localization in fiber reinforced cementitious composites a combined computational/analytical models have been developed. To this end, linear-elastic multi-directional fibers were embedded into a cementitious matrix. The resulting composite was described by different types of two-invariant non-associated Drucker-

Prager plasticity models. In order to investigate effects of a shape of a yield surface and hardening type linear and nonlinear yield surfaces, and linear and nonlinear hardening rules were considered. Diagnostic strain localization analyses were conducted for several plane stress uniaxial tension and uniaxial compression tests on non-reinforced cementitious composites as well as on high performance fiber-reinforced cementitious composites. It was found that presence of fibers delayed the inception of strain localization in all tests on fiber-reinforced composites. Furthermore, presence of fibers exerted a more significant effect on the strain localization direction and mode in uniaxial compression than in uniaxial tension.

The main objective of experimental program was to facilitate characterization of the post-cracking tensile behavior of ultra-high performance fiber reinforced cementitious composites. To this end, five different mixes of fiber-reinforced cementitious composites were cast, whereby volumetric fiber content, fiber shape and water to binder ratio were the experimental variables. Two testing methods were adopted, a direct uniaxial tension test and four-point prism bending test. Two different post-cracking behaviors were observed in direct tension tests, softening and strain hardening accompanied with multiple cracking. On the other hand, the response from prism bending tests was less scattered.

Several different inverse analyses were carried out to predict stress-strain and stress-crack opening displacement responses in uniaxial tension based on the prism bending tests. The analyses resulted in worthy correlations with the experimental data, thus suggesting that the prism bending test is a viable alternative to a much more challenging to perform direct tension test for ultra-high performance fiber reinforced composites.

Modeling of localized deformation in high and ultra-high performance fiber reinforced cementitious composites

by

Marta Miletić

B.S., University of Zagreb, 2009
M.S., University of Zagreb, 2011

A DISSERTATION

submitted in partial fulfillment of the requirements for the degree

DOCTOR OF PHILOSOPHY

Department of Civil Engineering
College of Engineering

KANSAS STATE UNIVERSITY
Manhattan, Kansas

2016

Approved by:

Major Professor
Dr. Dunja Perić

Copyright

Abstract

A low ratio between the compressive strength of concrete and its cost makes concrete one of the most widely used construction materials in civil engineering. Despite of a very good response to compressive stress, concrete exhibits a low tensile strength and limited tensile strain capacity. Adding short discrete fibers to a cementitious matrix can significantly improve its performance under tensile stress, thus ultimately exhibiting a ductile behavior. Nevertheless, in spite of their beneficial properties fiber reinforced cementitious composites remain underutilized in engineering practice. One of the main reasons for this is a lack of an adequate characterization of the tensile behavior as well as a lack of analysis methods that would allow engineers to incorporate fiber reinforced structural concrete elements into their design. Therefore, this dissertation has four key objectives: 1) to computationally model a stress-strain response of high performance fiber reinforced cementitious composites in uniaxial tension and uniaxial compression prior to macro-crack localization, 2) to develop and perform a diagnostic strain localization analysis for high performance fiber reinforced cementitious composites, the results of which can characterize effects of fibers on failure precursors, 3) to devise and perform an experimental program for characterization of ultra-high performance fiber reinforced cementitious composites, and 4) to characterize a full-fledged behavior including stress-strain and stress-crack opening displacement responses of ultra-high performance fiber reinforced cementitious composites in uniaxial tension.

To quantify effects of fibers on onset of strain localization in fiber reinforced cementitious composites a combined computational/analytical models have been developed. To this end, linear-elastic multi-directional fibers were embedded into a cementitious matrix. The resulting composite was described by different types of two-invariant non-associated Drucker-

Prager plasticity models. In order to investigate effects of a shape of a yield surface and hardening type linear and nonlinear yield surfaces, and linear and nonlinear hardening rules were considered. Diagnostic strain localization analyses were conducted for several plane stress uniaxial tension and uniaxial compression tests on non-reinforced cementitious composites as well as on high performance fiber-reinforced cementitious composites. It was found that presence of fibers delayed the inception of strain localization in all tests on fiber-reinforced composites. Furthermore, presence of fibers exerted a more significant effect on the strain localization direction and mode in uniaxial compression than in uniaxial tension.

The main objective of experimental program was to facilitate characterization of the post-cracking tensile behavior of ultra-high performance fiber reinforced cementitious composites. To this end, five different mixes of fiber-reinforced cementitious composites were cast, whereby volumetric fiber content, fiber shape and water to binder ratio were the experimental variables. Two testing methods were adopted, a direct uniaxial tension test and four-point prism bending test. Two different post-cracking behaviors were observed in direct tension tests, softening and strain hardening accompanied with multiple cracking. On the other hand, the response from prism bending tests was less scattered.

Several different inverse analyses were carried out to predict stress-strain and stress-crack opening displacement responses in uniaxial tension based on the prism bending tests. The analyses resulted in worthy correlations with the experimental data, thus suggesting that the prism bending test is a viable alternative to a much more challenging to perform direct tension test for ultra-high performance fiber reinforced composites.

Table of Contents

List of Figures

List of Tables

Acknowledgements

Finishing this doctoral dissertation brings me a mix of satisfaction and nostalgia difficult to describe. Looking back in time, I quickly realize that these four years of research were a memorable stage in my life. Therefore, I want to express my gratitude to those who have contributed the most for my academic, professional and personal growth.

First and foremost, I would like to graciously thank my advisor, Dr. Dunja Perić, for making all of this possible. If it were not for her supervision, support and guidance this dissertation would have never been written. Her willingness to meet and discuss with me on a daily basis will be what I miss the most. It has been an absolute privilege to study under her tutelage.

Special thanks and gratitude are also extended to the members of the supervisory committee: Dr. Nathan Albin, Professor Asad Esmaeily, Dr. Stacey Tucker-Kulesza, and Dr. Xiaojiang Jack Xin. I would like to thank the members of the Department of Civil Engineering at Kansas State University, including faculty, staff and other colleagues from the Department who contributed to a pleasant stay in Manhattan.

The experimental part of this research was carried out at the School of Civil and Environmental Engineering at the University of New South Wales, Australia. Therefore, I would like to graciously thank Professor Stephen Foster for giving me the opportunity to work with him and his research team at the University of New South Wales. His interest, steadfast attitude, and suggestions gave me motivation to develop an important part of this dissertation. Gratitude is extended to Dr. Ali Amin for his conveying knowledge, constant support and friendship.

Furthermore, I would also like to thank the technicians of the School of Civil and Environmental Engineering, Anthony MacKen and William Terry, for helping me with

manufacturing and testing the specimens. In addition, I greatly appreciate the opportunity to mentor and supervise a group of undergraduate students working on their final year honors thesis projects. Thank you to Elwyn Stannard, Henry Nguyen, Munawar Sarker and Simone Wong, for allowing me to develop my skills as a mentor and for providing much welcomed assistance in the laboratory.

Moreover, I would like to thank my friends, whom without I would not have managed to achieve many things. In particular, I owe special thanks to my friends Elvis, Fatemeh, Ginger, and Jan, and for their patience and support and to all those with whom I shared great experiences in Manhattan, and Sydney. I would also like to thank my friends, Ana, Lucija and Sonja, living in Croatia and all others living worldwide who assured me that time and distance are not barriers for true friendship.

Finally, and most importantly, I would like to express my wholehearted gratitude to my mother Jadranka, my father Mladen and my wonderful sister Mladena for their unconditional love, ongoing encouragement and support. I would not have come this far without you.

Dedication

This dissertation is dedicated to my beloved parents, mother Jadranka, father Mladen, and sister Mladena. Your support, encouragement and love helped me to get to another achievement in my life.

Chapter 1 - Introduction

1.1. Background and motivation

Concrete is presently the most widely used construction material worldwide because of its low ratio between its cost and its compressive strength as compared to other available alternatives. Nevertheless, the principal disadvantages of concrete are its low tensile strength and limited tensile strain capacity, which are likely to produce detrimental effects. With a rapid growth of human population, industrialization, and climate changes, the present day concrete structures are often exposed to extreme loads, such as earthquakes, tsunamis, floods, fires, and large-scale unplanned sporting and cultural events, which could lead to catastrophic failures that result in loss of human life and property damage. Therefore, critical efforts are needed to develop sustainable and advanced building materials and placement technologies that can produce long-lasting materials. These materials are required to be increasingly more energy-efficient, environmentally friendly, sustainable, affordable, and resilient. They need to meet multi-hazard/-performance design criteria and be easily produced and incorporated into construction methods and practice.

Low tensile strength of concrete and its limited tensile strain capacity have traditionally been resolved by adding reinforcing steel. It appears that adding steel fibers to a plain concrete could not only replace some of the reinforcing steel, but it could also enhance engineering properties of the resulting fiber reinforced concrete as compared to the plain concrete [1]. Therefore, short discontinuous fibers with high tensile strength have been added to concrete mixes to improve their tensile strength and tensile strain capacities, thus directly improving the resilience, toughness, and durability of concrete structures. The resulting material is known as fiber-reinforced concrete (FRC). Furthermore, a combination of a proper fiber geometry and

specifically tailored cementitious matrix, whereby enhanced bond properties between the fibers and matrix are achieved, leads to a strain-hardening behavior that turns the traditionally brittle material into a ductile material. These types of composites are called high and ultra-high performance fiber-reinforced cementitious composites (HPFRCC and UHPFRCC)([2], [3], [4]).

UHPFRCC has a high potential for accomplishing significant gains in engineering performance and economy, but its adoption into an engineering practice routine has been slow. One of the main reasons for this may be in the absence of understanding of both, the theoretical aspects that describe the post cracking residual strength of UHPFRCC and standardized design procedures that would allow engineers to incorporate UHPFRCC structural elements into their designs. Interest in UHPFRCC is evident from the upsurge of related research activities in the last 15 years, most of which has been of experimental nature ([5], [6]). Thus, significant research related to development of computational and analytical models, as well as design procedures are needed for an accelerated uptake in the engineering practice. This requires test methods that can correctly, and accurately, establish the constitutive behavior of HPFRCC and UHPFRCC.

Essentially, the lack of uptake of this advanced material boils down to a couple of issues. The first one is in that development and implementation a combined analytical-numerical algorithm that can capture a stress-strain response and inception of strain localization in elastic-plastic fiber-reinforced pressure sensitive materials. Strain localization is a ubiquitous feature of elastic-plastic materials that signifies an inception of narrow zones, also known as deformation bands, within which large strains develop while little or no strain occurring outside of these zones. Thus, strain localization can be characterized by a jump in strain rate across the boundary of a deformation or localization band. It is because the strain localization is followed by a

softening response, typically leading to a catastrophic collapse of materials and structures that it is an important failure precursor. Consequently, a complete evaluation of the efficiency of fiber reinforcement in cementitious composites requires that a diagnostic strain localization analysis be performed. Specifically, the analysis affords an improved characterization of the effect of fibers on the failure initiation by providing stress and strain levels at the inception of strain localization as well as orientations of accompanying discontinuities and corresponding strain localization modes. Ultimately, a diagnostic strain localization analysis supplies a quantitative measure of the fiber contribution towards increased resilience and toughness of these important civil infrastructure materials.

The second issue is development of the standardized procedures for the material characterization and design of UHPFRCC, which can accurately establish the constitutive behavior of the material [7]. In order to characterize the tensile behavior of the UHPFRCC, a variety of different test methods has been proposed by engineers and research bodies. They are direct and indirect tension tests. The latter includes prism bending test, round panel test, and cylinder splitting test, which are combined through an inverse analysis. The specific focus of this study was to devise a configuration of direct tensile test that would be suitable for testing an UHPFRCC, conduct direct tension and prism bending tests, and establish their correlation through an inverse analysis. It is important to understand the shortcomings of experimental testing methods to properly perform an inverse analysis.

From the theoretical point of view, a direct tension test is the ideal test for experimental characterization of post-cracking properties of the UHPFRCC because it eliminates a need for inverse analysis of the material response. From the practical point of view, a direct tensile test is challenging, time consuming and more expensive than indirect tensile tests. Specifically, some of

the most common problems associated with a direct tension test are: misalignment of the specimen before and during the test, a gripping arrangement and specimen shape (i.e. ensuring that failure occurs far enough from grips), material imperfections in the specimens that lead to stress concentration, and need for sophisticated equipment ([8], [9], [10]). Many experimental test setups and configurations have been tried and results published but no common agreement in the form of universally accepted standards has been established to date.

The indirect four point bending test on the un-notched prismatic specimen has been proposed as a less expensive and quicker alternative to the direct tension test. Nevertheless, the main disadvantage of the prism bending test is that it is not possible to obtain post-cracking properties in a direct way ([11], [12]). Therefore, to obtain post-cracking properties an inverse analysis is needed. Inverse analysis is a well-known and established procedure for the conventional concrete, but its extension to UHPFRC requires consideration of a large number of parameters that contribute to a post cracking strength. Therefore, this study attempts to further the current scope of understanding of UHPFRCC and FRCC in general, in order to bring its use and benefits to the construction industry and subsequently to the society at large.

1.2. Research objectives

The objectives of this research are directly related to the aforementioned needs and significance. They are listed below in the order in which they are addressed in this dissertation.

▪ Gain a thorough understanding of the theories, concepts and current research in the area of strain hardening steel fiber reinforced cementitious composites.

▪ Develop and implement a combined analytical-numerical algorithm that can:

a) Capture a stress-strain response and inception of strain localization in elastic-plastic fiber-reinforced pressure sensitive materials.

b) Perform a diagnostics analysis of the onset of strain localization in elastic-plastic pressure-sensitive fiber reinforced materials.

▪ Provide quantitative assessments of the effect of fibers on the onset of strain localization, orientation of the accompanying deformation bands and their deformation modes. The ultimate goal is to provide more detailed evaluation of fiber effect on the response of these materials.

▪ Identify specimen geometry and loading arrangement which would ensure a uniform tensile stress field over a large area that is unaffected by the loading arrangement.

▪ Examine the post cracking response of UHPFRCC through a direct tension test and prism bending tests.

▪ Refine, modify and adapt current inverse analysis models to UHPRFCC by comparing their predictions to the experimental data obtained from direct tensile tests.

1.3. Structure of dissertation

This dissertation is composed of six chapters as follows:

Chapter 1: Introduction. This chapter gives an overview of the conducted research. Moreover, it points out the motivation, objectives and the structure of the dissertation.

Chapter 2: Literature Review. This chapter reviews relevant literature and provides background regarding: the historical development of fiber reinforced cementitious composites (FRCC), onset of strain localization, mechanisms of crack formation and propagation, and factors contributing to the strength of FRCC. Furthermore, a brief review of different test

methods that characterize the post cracking behavior of FRCC is provided, with the particular emphasis placed on the uniaxial tension test and prism bending test.

Chapter 3: Strain Localization Analysis in HPRFRCC. This chapter describes fiber effects on the inception of the strain localization, and provides an overview of three different two-invariant Drucker-Prager models. Moreover, stress-strain response and predictions for onset of strain localization are presented and discussed.

Chapter 4: Material Characterization of UHPFRCC. This chapter outlines materials, mix proportions and fiber properties used in the experimental study. Test procedures and results obtained from the uniaxial compression tests and tensile tests are presented as well.

Chapter 5: Inverse Analysis. This chapter presents, analyzes and discusses the results of three different inverse analysis procedures, all of which turned out to be capable of converting the results from prism bending tests to direct tension tests, thus providing the characterization of the post-cracking behavior of UHPFRCC. Accuracy of predictions of different methods is evaluated and discussed.

Chapter 6: Conclusions and Future Perspectives. This chapter presents and discusses major findings and conclusions arising from the research conducted in this study. It also contains recommendations for future research resulting from this study.

Chapter 2 - Literature review

2.1. Fiber reinforced cementitious composite

2.1.1. Introduction

Concrete is a geo-material that is currently the most widely used construction material worldwide. This is so because concrete has a high compressive strength to cost ratio. Perhaps the main disadvantage of concrete is its low tensile strength and limited tensile strain capacity, which are likely to produce detrimental effects.

Present day concrete structures are often exposed to extreme loads, such as earthquakes, tsunamis, floods, fires, and large-scale unplanned sporting and cultural events, which could lead to catastrophic failures that result in loss of human life and rapid deterioration of civil infrastructure systems. Low tensile strength of concrete and its limited tensile strain capacity are traditionally resolved in several ways, such as an addition of the long, reinforcing conventional steel bars and wires, fiber reinforced polymers [13], short discrete fibers [14] or the combination of any former three ([15], [16], [17], [18]).

Research has shown several benefits of a short, discrete steel fiber reinforcement over reinforcement with the conventional steel in some applications. Use of steel fiber reinforced concrete reduces site labor, which is more intensive in the case of conventional steel reinforcement. Once the concrete hardens, the network of fibers functions similarly to traditional rebar reinforcement. Furthermore, fibers are typically distributed throughout a given cross section, whereas reinforcing bars or wires are placed only where required, which makes an area of reinforcement to the area of concrete using steel fibers greater as compared to using a network of reinforcing bars of wires. Moreover, this close spacing of fibers in a cementitious matrix has been shown to be effective in reducing plastic shrinkage cracking, surface permeability, dusting,

wear, etc., which ultimately leads to a reduction in maintenance, and thus to lower overall life cycle costs.

2.1.2. Historical overview

The concept of using fibers in order to enhance material properties of brittle materials is not novel. Since ancient times, mankind has been searching for construction materials with better performance so that taller, longer and better structures could be built. For example, straw and horsehair were used in order to improve tensile properties of the sunbaked bricks.

From today's perspective, the research on fiber reinforced concrete started about 50 years ago, with the pioneering research undertaken in 1960s by Romualdi and Batson [19] and Romualdi and Mandel [20]. Both research studies demonstrated that the tensile properties of concrete, such as strength and crack resistance could be significantly enhanced by providing closely spaced and randomly orientated wire reinforcement. Moreover, in the early stages of research straight steel fibers at relatively low volumetric fiber contents were used to improve tensile properties of a conventional concrete, but with a moderate success. Although the addition of fibers slightly increased the toughness of a cementitious composite, its ductility remained more or less unaffected. Addition of larger volume contents of fibers was mainly prevented by workability problems.

Interest in the material grew rapidly, so the first step in solving workability and fibers bundling problems was decreasing the amount of a coarse aggregate and increasing the quantity of cement. In addition, further progress in workability was accomplished by incorporation of chemical high range water reducing admixtures, also called superplasticizers. The next step towards developing fiber reinforced cementitious composites with the improved tensile

properties was utilization of more refined fibers with enhanced bond properties [21]. Finally, a combination of a proper fiber geometry with specifically tailored cementitious matrix whereby enhanced bond properties between the fibers and matrix are achieved lead to a strain-hardening behavior that turns a traditionally brittle material into a ductile material. This type of FRCC is called high performance fiber-reinforced cementitious composite (HPFRCC) [3]. Finally, in order to create a concrete with an extremely high compressive and tensile strengths a concept of adding a large amount of small fillers, such as silica fume and cement, and short steel fibers gave a birth to reactive powder concrete, also called ultra-high performance fiber reinforced cementitious composite (UHPFRCC) [22].

Some of the examples of modern FRCCs are: slurry infiltrated fiber concrete (SIFCON) [14], engineered cementitious composites (ECC) [6], UHPFRCC [23], and high performance hybrid fiber concrete [24]. The main scope of this research is on HPFRCC and UHPFRCC, and thus their characterization. Some applications, advantages and disadvantages will be presented in the text below. For more details on the history and overview of HPFRCC and UHPFRCC the reader is referred to Naaman [1] and Voo and Foster [5], respectively. Furthermore, an overview of fiber reinforced cementitious composites can be found in Balaguru and Shah[14].

2.1.3. Fibers

Fibers are the crucial constituent of FRCCs. Today, they exist in a wide range of different shapes and sizes, and can be made out of the many different materials. The majority of FRCCs in structural engineering applications contain steel fibers, but fibers can also be made out of a polypropylene, polyethylene, polyester, carbon, glass, natural, acrylic, etc.

In contrast to steel fibers used in the pioneering research in the 1960s, contemporary fibers come in a somewhat deformed shape to improve the mechanical bond between the fiber and cementitious matrix. Some common shapes are, but not limited to: smooth, indented, with hooked ends, paddles, buttons, crimped, coiled, or with other different types of anchorages. Figure 2.1 illustrates the primary geometric forms of fiber reinforcement [25]. The latest concept is the usage of the twisted fibers, that results in excellent material performance as is presented in Naaman [26].

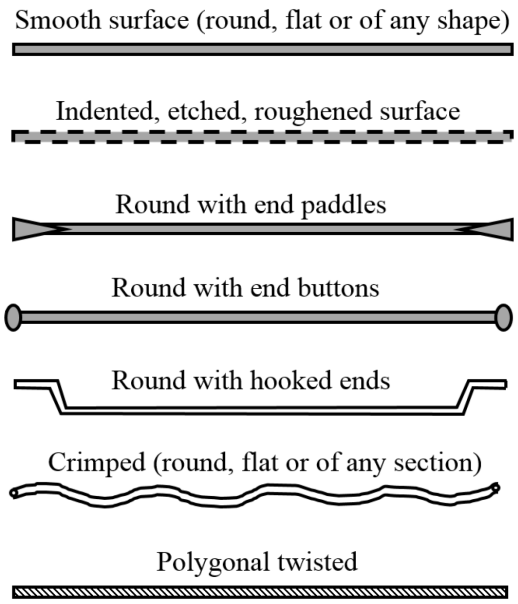

Figure 2.1 Primary geometric shapes and forms of fiber reinforcement (adapted from [25])

Effects of fibers on the material properties of the FRCC depend on the shape and fiber material. For example, short, discrete fibers, also called micro fibers, have lengths ranging from 5-20 mm with an equivalent diameter typically not greater than 0.1 mm, thus having dimensions similar to those of the potential micro-cracks. Therefore, short fibers are mainly used to effectively arrest micro-cracks and their propagation through the FRCC under tensile loading.

Consequently, short fibers are the main reason for the high first-cracking tensile strength of the FRCC. Similarly, long fibers become effective in arresting and postponing the growth of macro-cracks in the FRCC under tensile loading [27]. During an initial loading phase, long fibers effectively capture the propagation of the macro-cracks, which makes them responsible for a strain-hardening and multiple cracking behavior of the FRCC. In the following phase that corresponds to development of a large macro-crack, long fibers bridge the crack, thus producing a smooth softening curve and a non-brittle failure of the material [24]. Figure 2.2 depicts the effects of different fiber sizes on the tensile behavior of the cementitious composite. The same observations concerning the functioning of long and short fibers can be made for both, steel and synthetic fibers [28]. In addition, synthetic fibers are more often used for the control of plastic shrinkage, while steel fibers are mostly used for structural reinforcement. Up to date, a large amount of research has been done on concrete behavior reinforced with different types of fibers, volumetric fiber contents, fiber materials, etc. Reader is referred to Wille et al. [29] for further information about this research. In summary, according to Naaman [26], in order for a fiber to perform well in the FRCC it should have the following properties: a tensile strength that is 20 to 30 times greater than the tensile strength of a matrix, a bond strength between fiber and matrix that is at least as high as the cracking strength of the matrix, and a Young's modulus that is at least three times higher than that of the matrix.

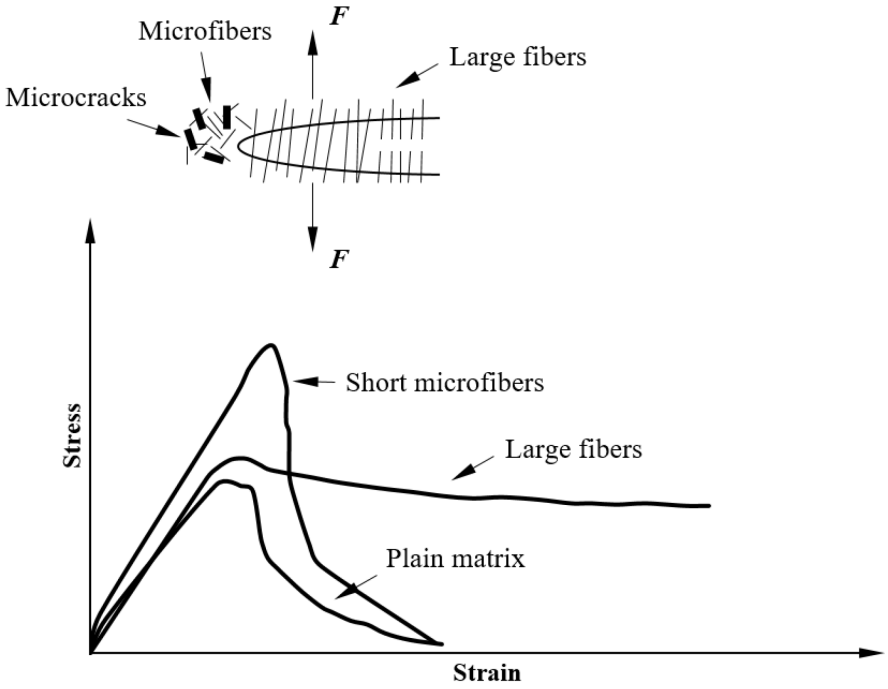

Figure 2.2 Effect of different fiber size on the tensile behavior of the cementitious composite (adapted from [28])

Furthermore, when talking about the fibers in the FRCC, the two most important properties are the fiber aspect ratio, η_f and the volumetric fiber content, χ_f (%). The aspect ratio of a fiber is a measure of the fiber slenderness. In the other words, the aspect ratio is the ratio between the length of a fiber and its diameter. In addition, χ_f is the ratio between the volume of fiber and the volume of the FRCC. Steel fibers, which are mostly used as reinforcing fibers, commonly have a length and a diameter varying between 6-80 mm and 0.15-1.0 mm, respectively. Their aspect ratios range from around 40 to 500 but typically less than 300 [4]. Typical volumetric fiber contents for steel fibers in FRCCs are between 0.25 and 3%. On the other hand, synthetic fibers vary much more in size and their diameter can be as little as 10 μm up to 0.8 mm. Their length is usually between 10-80 mm and they are usually added to the cement matrix in the volumetric fiber contents from 0.5 to 2 %. The coarser fibers normally have the aspect ratio below 100 whereas the aspect ratio of fine fibers can easily exceed 100.

2.1.4. Overview and classification of FRCCs

Classification is an important requirement for all construction materials, including cementitious composites. Before any kind of a classification of the fiber reinforced cementitious composites is presented it is important to point out that there is some confusion in the literature about the terms used to describe different FRCCs. Many authors propose new designations for their material or use an existing designation, but in a different context. Therefore, this section provides the most commonly used classification of FRCCs and define the terms as they are used within the scope of this dissertation.

When classifying traditional non-reinforced concrete, compressive strength is the most widely used design parameter in the construction industry and research [30]. The compressive strength can be used to distinguish among plain concrete (PC), HPFRCC, and UHPFRCC. Characteristic responses of the PC, HPFRCC, and UHPFRCC in uniaxial compression can be seen in Figure 2.3.

In the case of a PC, the compressive strength varies between 20 and 50 MPa. HPFRCC has a slightly enhanced compressive strength, which falls between 50 and 100 MPa, but in the same order of magnitude as PC. However, this does not apply to UHPFRCC. Due to a very dense packing of the particles in the matrix, and heat and mechanical treatment, not only the compressive strength but also the bond between matrix and fibers is significantly improved. Under in-situ conditions, a compressive strength of UHPFRCC can range from 150 to 230 MPa and under laboratory conditions (i.e. precast structural elements) compressive strength up to 800 MPa can be achieved, which is five to ten times greater than that of PC (Table 2.1).

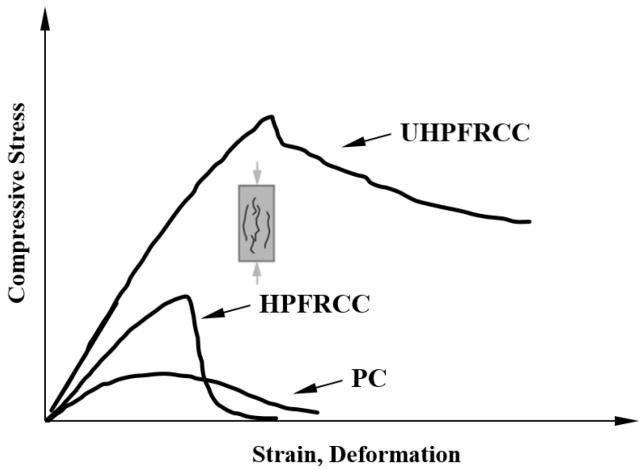

Figure 2.3 Comparison of characteristic responses of PC, HPFRCC, and UHPFRCC in uniaxial compressive stress state (adapted from [31])

It should be noted that the increase in the compressive strength of HPFRCC, and UHPFRCC is primarily due to a specifically tailored cementitious matrix, and only marginally due to the presence of fibers in the matrix. It can be seen from Figure 2.3 that the shape of the characteristic compression responses is not fundamentally changed. In the other words, in both, non-reinforced concrete and FRCCs compressive behavior is characterized by some degree of strain hardening up to the compressive strength, after which a compression softening commences. The compression softening part is influenced fibers. As fiber volumetric content increases, toughness and ductility are increasing as well, but it is not taken into account in design.

Moreover, the addition of fibers into the matrix predominantly influences the tensile behavior of cementitious composites. Therefore, the classification of FRCC materials presented here is based on the tensile behavior only.

The most widely accepted classification of FRCCs is based on their stress–deformation response from a direct tension test and their load–deflection response from prism bending test ([32], [33]). Following this approach, first, the tensile behavior of FRCC under a direct tensile

loading can either be classified as strain softening or strain hardening behavior. The characteristic response of the PC, regular fiber reinforced concrete (FRC), HPFRCC, and UHPFRCC in the uniaxial tension can be seen in Figure 2.4.

It can be seen that the traditional concrete is extremely weak and essentially has no strength in tension. The tensile strength of the PC usually ranges between 2 and 5 MPa (Table 2.1). Moreover, PC has a very brittle response after the tensile strength is reached, which is an undesirable feature for industry application due to the limited display of forewarning prior to a sudden failure. Thus, when it comes to designing concrete structures, the direct tensile strength of the PC is typically disregarded in most of the building codes and standards.

Incorporation of discrete fibers into a plain concrete, as in the case of regular FRC, slightly increases the tensile strength, improves the post-peak response, and transforms the post-peak behavior from the extremely brittle to less brittle. In this case, the failure occurs over one localized macro-crack and it takes place at first cracking stress. Moreover, after the first crack of a matrix, a residual tensile strength of the specimen will never reach the so-called first cracking strength of the matrix, but it vanishes with the further crack opening. This type of tensile behavior is characteristic of the conventional FRCC and can be classified as a strain softening FRCC.

In the case of the strain hardening FRCC, after the first cracking stress of the matrix is reached under the uniaxial tensile load, residual tensile stresses are further increasing. This increase in the residual tensile stresses is accompanied with a multiple micro-cracking distributed within the specimen, which is followed by the delayed stress localization in macro-crack. The extent of the strain hardening depends strongly on the volumetric fiber content, and the type of fibers used [1]. Moreover, in addition to improved post-cracking behavior, the first cracking

stress and tensile strength are considerably increased due to a very densely packed matrix, which improves the bond between the fibers and the cementitious composite. HPFRCC can achieve the direct tensile strength in the range of 5 and 7 MPa [34], while in the case of the UHPFRCC even higher tensile strength can be developed. For example, the study conducted by Graybeal [35] showed that the highest possible tensile strength that can be reached is about 15 MPa (Table 2.1).

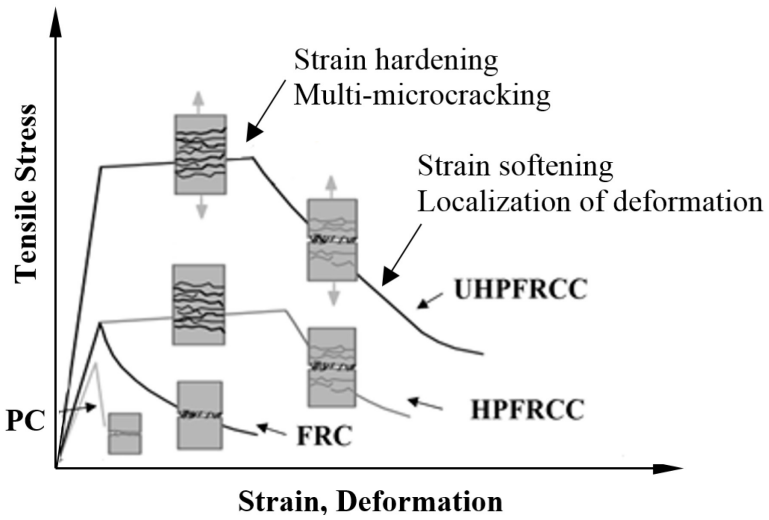

Figure 2.4 Comparison of characteristic responses of PC, FRC, HPFRCC, and UHPFRCC in uniaxial tensile stress state (adapted from [31])

Furthermore, it must be noted, that the flexural behavior differs to that of a direct tension. To complicate matters, although some FRCCs are exhibiting strain softening behavior in direct tension test, they can show a softening or hardening behavior in prism bending test. The strain hardening FRCCs, usually have hardening behavior in prism bending test. This softening and hardening behavior is also called deflection softening and deflection hardening, respectively ([36], [37]). However, it should be emphasized that deflection hardening is heavily dictated by the dimension and the cross-section geometry of a sample. Jiang and Banthia [37] showed that in the case of a thin beam deflection hardening was obtained, while with the increase only in the

beam height, the flexural response changed to a deflection softening. Therefore, deflection behavior of FRCC is not a material property in the strict sense.

For better understanding, Wille et al. [33] proposed the complete classification scheme, based on both stress–deformation response of FRCC from the direct tension test and their load–deflection response from prism bending test, which categorizes cementitious composites into the five different levels of behavior (Figure 2.5). Figure 2.5 contains the following parameters: the first cracking stress $\sigma_{t,f}$, the first cracking strain $\varepsilon_{t,f}$, corresponding Young's modulus E, composite uniaxial tensile strength $\sigma_{t,p}$, the first cracking bending stress $\sigma_{fl,f}$, and peak bending stress $\sigma_{fl,p}$. It is worth noticing that the stress versus strain relationship is only valid prior to a major cracking of a matrix. The post-cracking behavior is defined by the stress versus crack opening relationship. During the multiple cracking phase, the FRCC can be characterized by stress versus strain relationship assuming a smeared crack or plasticity approach [33].

In order to more clearly differentiate between performance levels four and five, energy absorption capacity prior to the tension softening, g is introduced as an evaluation parameter. Experimental results presented herein and by other researchers suggest that fiber reinforced concrete material with performance level five should have a high value of absorption capacity prior to macro-crack localization. Until more experimental data becomes available, a value of g=50 kJ/m^3 is assumed to be a dividing point between the performance levels four and five.

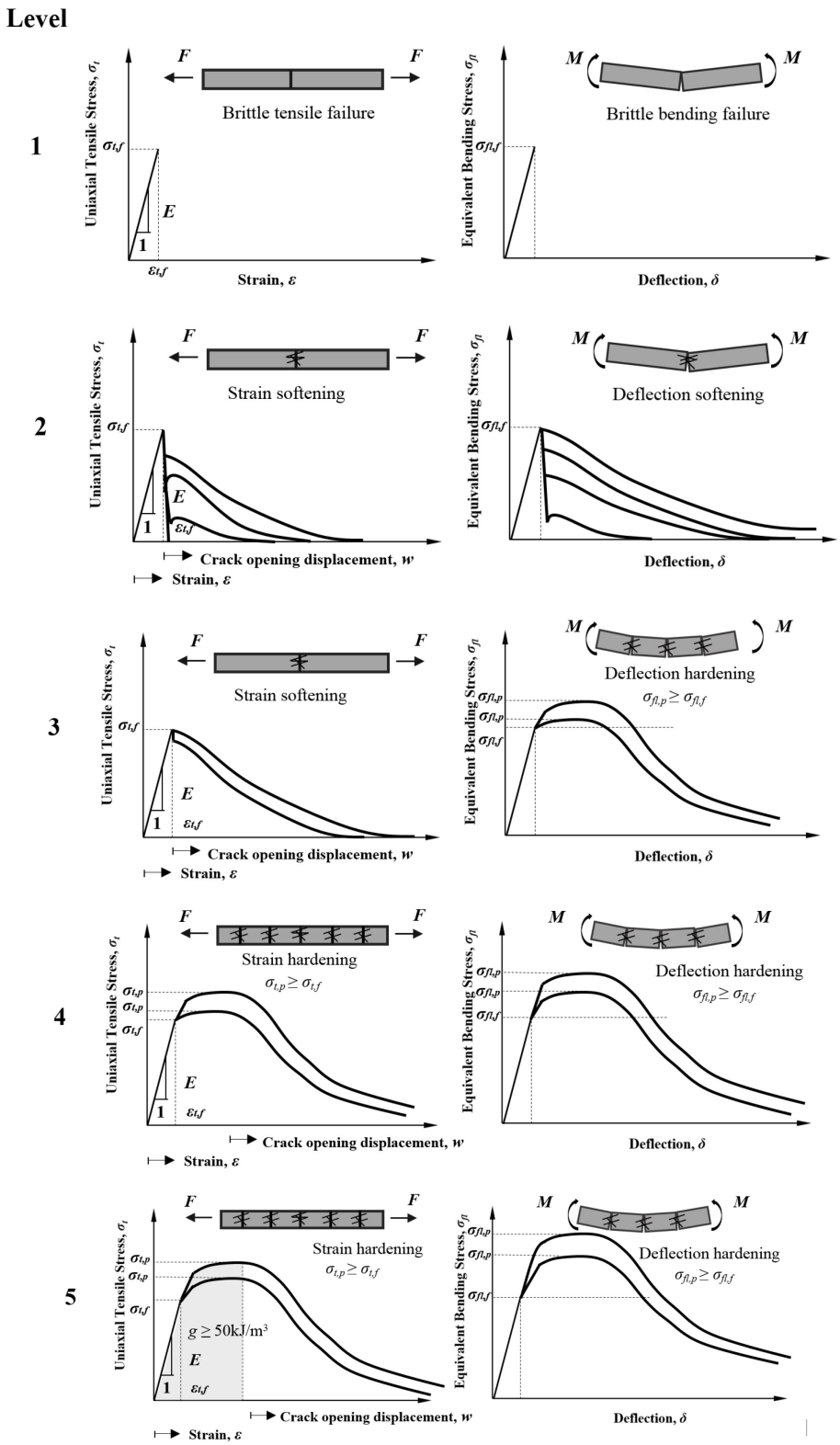

Figure 2.5 Schematic illustration of performance levels of the fiber reinforced cementitious composites (adapted from [33])

Finally, an overview and comparisons of other main material properties of PC, HPFRCC, and UHPFRCC are given in Table 2.1. UHPFRCC can achieve the greatest value of Young's modulus values larger than 40 GPa, followed by the HPFRCC and PC with values greater than 35 and 20 GPa, respectively. Regarding other material properties, such as flexural strength, flexural energy, ultimate tensile strain, porosity, durability, etc. UHPFRCC has remarkably the most superior characteristics in comparison to other concretes. This is due to denser and homogeneous UHPFRCC microstructure which is explained in the text below.

Table 2.1 Comparison of the mechanical properties of different cementitious composites (adapted from [38], [39])

Material Property	Units	PC	HPFRCC	UHPFRCC
Compressive Strength	MPa	20-50	50-100	150-800
Young's modulus	GPa	20-35	35-40	40-75
Tensile Strength	MPa	2-5	5-7	~10
Flexural Strength	MPa	4-8	6-10	15-140
Flexural Energy	J/m^2	130	140	1000-40000
Ultimate Tensile Strain	$x10^{-6}$	100-150	100-150	2000-8000
Porosity	%	20-25	10-15	2-6
Durability	-	Up to 700x lower than UHPFRCC	Up to 400x lower than UHPFRCC	

Material descriptions, properties, and applications of FRCC, HPFRCC and UHPFRCC are be described next.

High Performance Fiber Reinforced Cementitious Composites (HPFRCCs)

HPFRCC is an innovative class of FRCC whose intensive development started around 15 years ago. Its most prominent property, which also distinguishes it from conventional fiber reinforced concrete, is in that it displays strain-hardening behavior in direct tension. Strain

hardening behavior is achieved by a combination of a proper fiber geometry, specifically tailored cementitious matrix and improved bond properties between the fibers and matrix. As a result, HPFRCC is a lot more ductile than plain concrete, and even than conventional steel fiber reinforced concrete, which makes it suitable for a number of structural applications.

Material description, properties, and applications

As mentioned earlier, there is no a definition for the term HPFRCC, but the term HPFRCC will be used herein for the fiber reinforced cementitious composites, which exhibit strain hardening behavior in a direct tension, and have a normal matrix strength, and relatively low volumetric fiber content (≈1.5-2%). Typical HPFRCC matrix design consists of water, cement, fly-ash, and sand, but it does not contain a coarse aggregate because it adversely affects the tensile performance of the FRCCs, and thus its addition to the mix is avoided [40].

Regarding fibers, the most commonly used ones in the HPFRCC mixes are: Torex twisted steel fibers, Dramix® hooked steel fibers, and straight Spectra ultra-high molecular weight polyethylene fibers. Fibers properties are presented in Table 2.2.

Table 2.2 Fiber properties

Fiber Name	Length, l_f (mm)	Diameter, d_f (mm)	Aspect ratio, ηf	Tensile strength (MPa)	Fiber material
Torex	15-50	0.2-0.7	20-250	2470	Steel
Dramix®	30	0.38-0.55	55-80	1100-2300	Steel
Spectra	15-38	0.038	400-1000	2590	Polyethylene

The mechanical properties of HPFRCCs, such as a compressive strength, tensile strength, and Young's modulus, are twice the value of the ones of plain concrete. In particular, Young's

modulus of the HPFRCC varies in the range between 35-40 GPa, while compressive and tensile strengths of HPFRCC range between 50-100 MPa and 5-7 MPa, respectively (Table 2.1).

As in all FRCC, the most noticeable improvement of HPFRCCs is their more ductile behavior in uniaxial tension test (Figure 2.6 a). On the other hand, HPFRCCs show a smooth, post-peak softening behavior (Figure 2.6 b) under a uniaxial compression loading. Moreover, HPFRCCs display a large tensile and compressive strain capacities. For a more detailed description of HPFRCC and more experimental findings reader is referred to Parra-Montesinos [40].

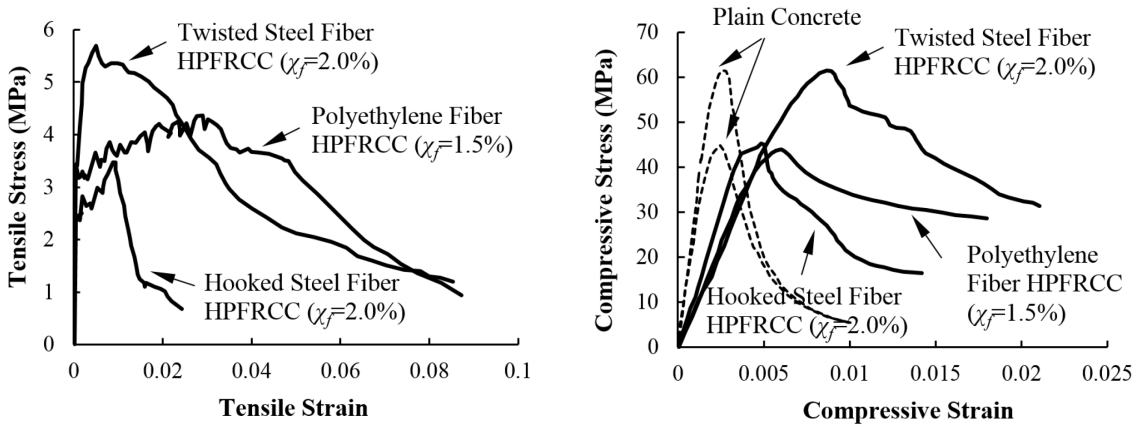

a) Tensile response b) Compressive response

Figure 2.6 a) Tensile, and b) Compressive behavior of HPFRCC with various types of fibers (adapted from [40])

From a practical perspective, the major benefit of HPFRCCs in the comparison with the normal concrete is an upsurge in a shear strength, which enhances overall ductility. In the other words, the larger the shear strength of a material, the lower the need for the confinement reinforcement. Therefore, HPFRCCs are mainly used in the applications, which make use of

these mechanical properties, such as coupling beams [41], [42], low rise structural walls [43], beam-column joints [44], cyclically loaded flexural members [45], etc.

Coupling beams present a classic example of the structural element subjected to large shear stresses and inelastic rotations during seismic events. As a consequence, such coupling beams require rather heavy and intricate shear reinforcement detailing for seismic resistance. In the past decade, the research group from the University of Michigan ([41], [42]), showed that the design of coupling beams can be simplified without compromising their seismic performance, if the HPFRCC is used as a structural material instead of a regular reinforced concrete. This is possible because the mechanical behavior of HPFRCCs, such as post-cracking tensile hardening and compression are similar to that of a well-confined concrete. This relaxation of the reinforcement results in a need for less amount of material, in labor, and construction time. Ultimately, the overall project costs can be significantly reduced.

Another classic example of a structural element, which due to a subjection to large shear forces requires a high amount of complicated reinforcement, is low-rise structural walls. Research conducted by Parra-Montesinos and Kim [43] showed that the usage of the HPFRCC in a construction of the low-rise structural walls increased the damage tolerance even with significantly less shear reinforcement. Furthermore, it was estimated that HPFRCC carried around 70% of the total shear forces.

Moreover, Parra-Montesinos et al. [44] conducted a research on the use of HPFRCC materials as a total replacement of confinement reinforcement in beam-column joints. Results from the study showed that the shear capacity of the joint region and the bond strength between the reinforcement and the cementitious matrix can be increased if HPFRC is used instead of a conventional concrete, even though the connection design did not satisfy minimum anchorage

length requirements specified in the ACI Building Code. This confirms the findings from Chao et al. [46] which indicate that the bond strength between steel rebars and an HPFRCC matrix is significantly better than between steel rebars and plain concrete.

Ultra-High Performance Fiber Reinforced Cementitious Composites

The forerunner of UHPFRCC which we know today is the Ultra High Performance Concrete (UHPC). The latter is a concrete with an exceptionally high compressive strength, development of which started in the late 1970s, and early 1980s with the pioneering work of H.H. Bache and the research group from Portland Cement and Concrete Laboratory [47]. In order to obtain a cementitious composite with a high compressive strength, large amounts of small fine particles (such as fly-ash, silica fume, and cement) were added to a cementitious matrix. The goal of adding small particles to the cementitious composite is to achieve a very dense packing of the particles in the matrix, which should significantly increase the density of the final composite. Moreover, thanks to the addition of the superplasticizers to a mix, even more effective dense particle packing was guaranteed with a sufficient workability even at low water-to-binder ratios of 0.16 to 0.18. Similarly, to the case of the HPFRCCs, the coarse aggregates were eliminated, and strong, small sized aggregates were used instead. The major reason why coarse aggregates were not used in the matrix was in that they make a cementitious matrix more heterogeneous and thus more susceptible to local stress concentrations and crack initiations. In other words, the smaller the aggregate size the better the homogeneity of the cementitious matrix. Moreover, if the aggregate's strength were not satisfactory fracture would pass through the aggregates. This in turn would mean that the high strength of a cementitious binder is not

used to its maximum. For these two reasons hard and small aggregates such as quartz sand or calcined bauxite are usually used.

Although having an outstandingly high compressive strength, UHPC has a noteworthy drawback. With its higher compressive strength, its brittleness is increased as well. In order to improve the ductility of the concrete matrix, a medium sized straight high strength steel fibers were added to the UHPC cementitious matrix, which gave a birth to the UHPFRCC that we know today ([23], [48], [49]). Some of the first experimental studies of this novel material were carried out at the Bourges and Lafarge laboratories in France during the mid-1990s [23]. A more detailed overview of UHPFRCCs can be found in Rossi [50] and Rossi [51].

Material description, properties and applications

As mentioned earlier, there is no exact definition of the UHPFRCCs in the technical literature. Therefore, in this study, the UHPFRCC will be considered to be a composite of an UHPC matrix with a compressive strength exceeding 150 MPa and high strength steel fibers. The addition of fibers in the cementitious matrix overcomes the enhanced brittle behavior of a plain UHPC under tensile loading.

Furthermore, the most common dimensions of the straight steel fibers used in UHPFRCC are 0.2 mm and 13 mm for the diameter and length, respectively. The typical UHPFRCC mixes contain fibers with the volumetric fiber content ranging between 1.5 and 3% due to a workability limitation.

In summary, UHPFRCC is a strain hardening fiber reinforced cementitious composite with a compressive strength exceeding 150 MPa due to a durable homogeneous and a dense packing microstructure. It is characterized by a low water-to-binder ratio, high cement content,

high silica fume content, high dosage of a third generation polymer based superplasticizer, usage of the small, hard aggregates such as quartz sand, and an addition of steel fibers. Moreover, the strength of UHPFRCC can be further improved by mechanical and thermal treatment during curing, such as post-set heat treatment and autoclaving, resulting in better mechanical properties. According to Richard and Cheyrezy [23], there are two types of the UHPFRCCs: RPC-200 and RPC-800. Acronym RPC stands for the reactive powder concrete, which is another name for the UHPFRCCs that can be found in the literature.

RPC-200 is what we know as a regular UHPFRCC. Usually UHPFRCC is subjected to the post-set thermal treatment because it accelerates the pozzolanic reaction and increases the amount of bound water, which finally leads to the enhancement of the microstructure of the hydrates [52]. The effectiveness of the post-set thermal treatment process depends on the temperature applied. This type of UHPFRCC is suitable to be used at the construction site.

Another type of the UHPFRCC, RPC-800 is a UHPFRCC subjected to a mechanical treatment. This type of treatment involves applying compacting pressure to the fresh concrete during setting. Applied pressure expellees the entrapped air and water from the matrix, which increases the density of the composite, and consequently, results in a higher compressive strength. Moreover, RPC-800 requires a heat treatment at significantly higher temperatures than the RPC-200, such as 250-400°C. Because both, the heat treatment with the high temperatures and the mechanical treatment, are complicated to apply in-situ, RPC-800 is used for the precast elements which can be manufactured under controlled laboratory conditions [23].

In the comparison with all other concrete mix designs, from the regular concrete to HPFRCC, UHPFRCC has the best mechanical properties. The most outstanding mechanical property is its extremely high compressive strength. Typical compressive strength of regular

UHPFRCCs, i.e. RPC-200, ranges between 150-230 MPa, while RPC-800 can achieve compressive strengths up to 800 MPa by applying previously mentioned manufacturing techniques and adding steel aggregates to the concrete mix ([23], [38]).

In comparison with the HPFRCC, UHPFRCC has even higher direct tensile strength. It can reach values between 8 MPa and 11 MPa. Moreover, because of the high packing density of the cementitious matrix Young's modulus generally exceeds 40 GPa for the regular UHPFRCCs, while in the case of the RPC-800 it can reach 75 GPa. The high packing density of the cementitious matrix leads to good durability characteristics of the UHPFRCC, because it prevents corrosive agent transport and freezing-thawing problems [53]. Complete detailed comparison of the fiber reinforced cementitious composites and plain concrete will be described in the following section.

In terms of structural applications of the UHPFRCCs, similarly to HPFRCC, due to the addition of the fibers to the matrix and the thereby provided ductility, very light and slender UHPFRCC structures with reduced steel reinforcement can be constructed [54].

These light and thin structures, with a high compressive strength and reduced steel reinforcement are fairly easy to build, thus providing a serious alternative to steel structures. One structural example of where this concept can be used is bridges. The first bridge built from UHPFRCC was the Sherbrooke reactive powder concrete footbridge over the Magog River in Quebec, Canada. It is an innovative pedestrian and bicycle bridge that has been built entirely with UHPFRCC, without any steel rebars [55]. Its superstructure has a 60 m span and carries a 30 mm thick walkway. The superior material strength resulted in a noteworthy decrease in the dead load of the bridge. Construction of the bridge definitely showed a full potential of UHPFRCC at that time. Up to date, UHPFRCC was used in construction of the numerous

pedestrian and highway bridges all around the globe. A complete overview of the bridges built so far in North America (United States and Canada), Europe, and Asia/Australasia using UHPFRCC can be found in Russell and Graybeal [56].

A research on the usage of the UHPFRCC for columns was conducted by Malik and Foster [57]. The study has shown that the UHPFRCCs effectively prevents both spalling of the cover concrete and the buckling of the longitudinal reinforcement to well beyond the peak load. The authors suggested that the elimination of tie reinforcement in RPC columns could be possible, but more test data are needed for the full justification.

Moreover, in substructural applications, UHPFRCC has been proved to be an attractive alternative to construction materials that are exposed to a significant deterioration due to environmental impacts, such as timber, steel, and concrete [39]. In research conducted by [39], precast and prestressed UHPFRCC piles, with the H-shaped cross-section and weight similar to a HP10x57 pile, were subjected to vertical and lateral loads. Test results showed that superior material properties improved constructability, reduced maintenance costs and would enable achievement of a minimum of 75 years long service life.

Apart to bridges and columns, due to its superior material properties, UHPFRCC is a great candidate for utilization in the buildings subjected to extreme environments, such as nuclear facilities, reactors, furnaces, impact resistant military structures, safes, etc. ([23], [58]). In addition, several research studies have been conducted on the potential usage of the UHPFRCC for infrastructure security applications, such as barrier protection systems or as inherent portions of the critical infrastructure. A detailed overview on UHPFRCC with a focus on security applications can be found in Astarlioglu et al. [59].

Furthermore, although UHPFRCC provides many benefits to design and performance, but as with other new and advanced materials, the initial cost and liability issues are currently of concern and usually provide obstacles to the use of these materials in construction.

If the comparison is made merely on the cost per cubic meter of material, the cost of UHPFRCC exceeds the cost of conventional concrete for one order of magnitude, due to concrete mix requirements and raw material availability. Additionally, there may be some initial extra costs due to modification, or purchase of equipment and facilities. New casting methods and procedures, labor training, and familiarization with the material may be necessary and may result in high manufacturing, processing and construction costs [56]. Some of these costs could be decreased for example by substituting expensive material UHPFRCC mixtures with the local and already available raw materials. This could lead to the further development of more economical, efficient, and green UHPFRCC. Moreover, as the technology advances, experience gains, competition grows, and market demands mass production, manufacturing, processing and construction, which may decrease costs as well.

Furthermore, as discussed earlier, UHPFRCC offers unique advantages and higher performance levels that help rationalize the increased initial cost even more. Due to its durability, structures that use UHPFRCC are expected to have a longer service life and require less maintenance than structures built with conventional concrete. A life cycle cost study of two replacement methods for the Eder bridge in Felsberg, Germany was carried out by [60]. The first replacement method used precast UHPFRCC box girders filled with lightweight concrete, while the second replacement method used conventional prestressed concrete bridge members. Both replacement types were subjected to a long-term performance evaluation, which included maintenance, inspection, and monitoring, repair and replacement. The study showed that

although the UHPFRCC-bridge had higher initial costs, its life cycle cost over 100 years would be less than for the normal concrete bridge.

In summary, UHPFRCC is a new material with advanced properties, such as compressive and tensile strengths higher than 150, and 15 MPa, respectively. It is not really conventional concrete anymore. Therefore, it might be a good idea not to think of UHPFRCC as conventional concrete as we know it now. Novel and innovative structural concepts and applications that can utilize the strength and superb performance of this material should be developed. UHPFRCC has a strong potential to help the revitalization of the civil infrastructure, and in the building of new infrastructure that is sustainable, resilient and long-lasting. However, implementation of UHPFRCC in the U.S. has been slow in comparison to Europe and Asia, particularly Australia, China, France, Germany, Iran, and Japan, and rigorous effort is needed in order to accelerate its usage in the U.S. construction industry.

2.2. Numerical modeling of FRCCs

A cementitious composite, including a fiber reinforced cementitious composite in this term as well, is a multi-scale material. Cement, aggregates, water, fibers, and various other additives are mixed together. A mix subsequently hardens, thus forming a solid material. Consequently, cementitious composites materials, structures made from these materials, as well as relevant testing and analysis techniques can be classified into three distinct levels namely micro, macro and structural levels. For example, Figure 2.7 depicts different scales of the observation on the example of the simply supported FRCC beam [61].

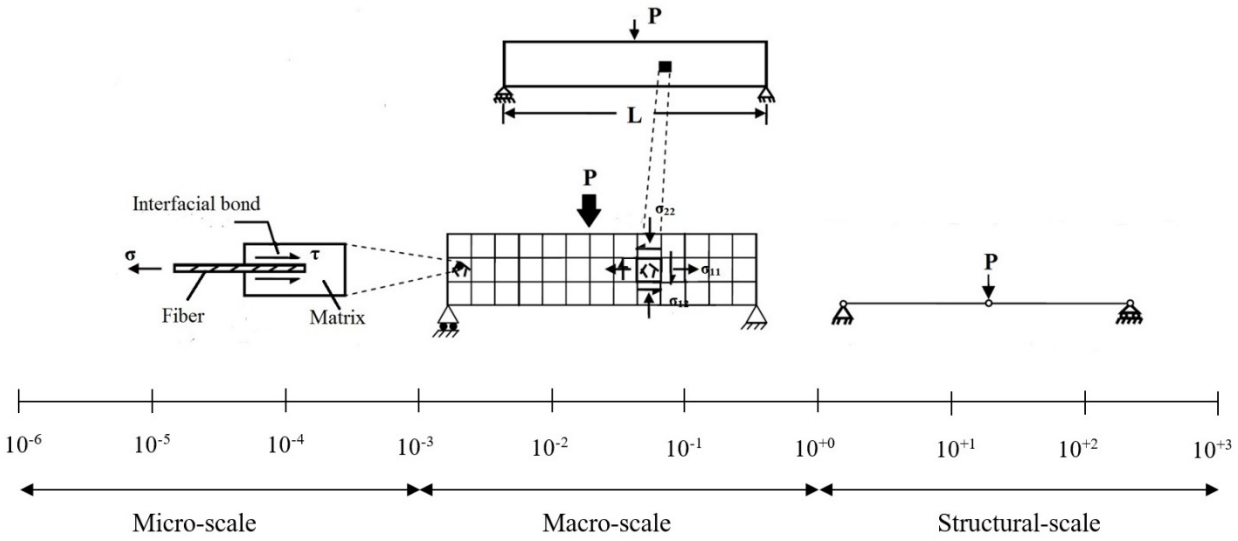

Figure 2.7 Different scales of observation on example of simply supported FRCC beam, units are in meters (adapted from [61])

First, at the micro-scale (10^{-3}-10^{-6} m), all individual constituents of the FRCC, such as aggregate grain, fiber, interfacial bond, pores, etc., can be distinguished from each other. An inception and propagation of matrix micro-cracks and a pullout of fibers that bridge these cracks are some of the essential features at this level of observation. In the other words, a cementitious composite as a matrix, fibers and the interfacial bond between the former two are explicitly modeled. Several methods have been proposed to model FRCC at the micro-scale level. It is because numerical modeling of the FRCC at the micro-scale level does not fall within the scope of this research that the more detailed explanation of the models will not be covered. For the most commonly used methods, such as a representative volume element (RVE) method and discrete modeling method, the reader is referred to Stang et al. [62], Leung and Geng [63], Alwan et al. [64], Sujivorakul [65], and Bolander and Saito [66].

At even larger scale, macro-scale, which ranges from 10^{-1}-10^{-2} m, internal individual constituents of the FRCC are not distinguished from each other anymore. It is assumed that FRCC at this scale has identical properties in each point of the specimen or structure, i.e. FRCC

is considered as a homogeneous material. Inherently, the behaviors of the FRCCs and plain cementitious composites are different from each other. Moreover, strain softening and strain hardening behaviors of the composite play a major role at this scale of the observation. Finally, at a structural scale, up to an order of 10^{+2} and 10^{+3} m, the scale of typical structural components in civil engineering is reached. At this observation level, the responses of interest include load carrying capacity, drift, durability, etc. The pertinent parameters that influence the response at structural-scale include member strength, stiffness, energy dissipation capacity, and ductility [67]. In structural-scale models, each component of a structure is represented using domain level elements that are characterized by load-deflection or moment-curvature responses depending on the type of the component. There are few examples of structural-scale models for HPFRCC including Stang and Olesen [68] who developed closed form moment-rotation relationships for the plastic hinge region in HPFRCC members in pure flexure.

Although modeling of FRCC behavior with the micro-scale model has the advantage that it can simulate a variety of details, it means that micro-scale models require high computational demands which could certainly limit their use in modeling of larger structures. Structural-scale models are able to model larger structures, but their disadvantage is in that they can capture only the overall behavior at the domain level, and do not provide detailed enough information about structural behavior. Finally, macro-scale models are presently more computationally efficient than micro-scale models and can model structural behavior in the continuum finite element simulations. For the previously mentioned reasons, macro-scale modeling of FRCC is chosen in this research.

In the following, an introduction to macro-scale modeling of FRCC materials will be presented. Nice overviews of nonlinear modeling and failure analysis of quasi-brittle materials

can also be found in Jirasek and Patzak [69]. After giving a brief overview of the most commonly used macro-scale models for FRCC, this chapter will focus on the theoretical background and literature review of the strain localization analysis in pressure-sensitive materials.

2.2.1. Macro-scale Models for FRCC

A great diversity of different macro-scale models for modeling concrete and FRCC can be found today. The most commonly used ones are: fracture mechanics, damage mechanics and plasticity models. Cementitious composites and FRCC behave considerably differently when subjected to compressive loads and tensile loads. Thus, in order to an overall constitutive model, which can properly capture both stress states, previously mentioned models can be combined together. This section will present a brief overview of the theory of plasticity.

The classical theory of plasticity consists of the four main components: elastic behavior, a yield condition, a plastic flow rule and a hardening law. The yield condition is a law defining the limit of the elastic domain of an elastic-plastic material under any possible combination of stresses. The yield condition is often graphically represented in the principal stress space by a yield surface. When the stress state reaches the yield surface, any further load increase will produce a permanent deformation. A number of material parameters needed to define the yield surface usually ranges from one to five. One- and two- parameter yield surfaces most often do not fit the experimental data obtained from experiments on pressure sensitive materials. Thus, at the minimum a three parameter- yield surface is needed in order to more realistically model behavior of cementitious composites. A lot of examples of yield functions for concrete and FRCC can be found in the literature, but some worth mentioning are: Chen and Chen [70],

Chang et al. [71], Lade [72], and Grassl [73] for three-parameter yield surfaces; Hsieh et al. [74], Sirijaroonchai [61], for four-parameter yield surfaces; Barzegar and Maddipudi [75] and Pivonka et al. [76] for five-parameter yield surfaces.

A plastic flow rule is the second component of the plasticity theory. The plastic flow rule defines the plastic flow direction for plastic yielding. A flow rule can be associative and non-associative. In the case of associate flow rule a plastic flow direction is perpendicular to the yield surface, because a plastic potential surface coincides with the yield surface. In the case of non-associative plastic flow, a plastic potential and yield surfaces do not coincide to each other. It was found by Smith et al. [77], Grassl [73] that the plastic flow direction of concrete is not perpendicular to the yield surface, and that the associative flow rule over estimates the volumetric response of concrete under triaxial loading conditions. Thus, in order to realistically model the behavior of pressure sensitive materials such as cementitious composites, a non-associative flow rule should be used. More information and examples about the usage of the potential functions for defining non-associative flow rule are presented in Imran and Pantazopoulou [78].

Hardening rule governs growth of a yield surface due to plastic hardening. The three most commonly used hardening rules are: isotropic, kinematic and mixed hardening rules. In the case of an isotropic hardening rule, a yield surface expands equally in all directions, while its center remains fixed.

On the other hand, a kinematic hardening rule indicates a translation of the center of the yield surface in the stress-strain space with the load increase, while the size of the yield surface remains constant. Finally, mixed hardening rule is the combination of the former two, i.e. the yield surface expands and moves together during a hardening process. It is important to note that

these previously mentioned hardening rules can only be distinguished if an unloading takes place, because a stress-strain responses of a material subjected to the monotonic loading for these models can be equal. Original development and derivation of hardening rules can be found in Hill [79] for isotropic; Prager [80] for kinematic; and Hodge [81] for mixed hardening. Plasticity models will be used for strain localization analysis. Therefore, a more detailed description will be presented later in the Chapter 3.

Onset of strain localization

Strain localization is a ubiquitous feature of elastic-plastic materials that signifies an inception of narrow zones, also known as deformation bands, within which large strains develop while little or no strain occurring outside of these zones. Thus, strain localization can be characterized by a jump in strain rate across the boundary of a deformation or localization band. It is because the strain localization is followed by a softening response, typically leading to a catastrophic collapse of materials and structures that it is an important failure precursor. Consequently, a complete evaluation of the efficiency of a fiber reinforcement in cementitious composites requires that a diagnostic strain localization analysis be performed. Specifically, the analysis affords an improved characterization of the effect of fibers on a failure initiation by providing stress and strain levels at the inception of strain localization as well as orientations of accompanying discontinuities and corresponding strain localization modes. Ultimately, a diagnostic strain localization analysis supplies a quantitative measure of a fiber contribution towards an increased resilience and toughness of these important civil infrastructure materials.

Several researches have investigated the OSL in a plain non-reinforced concrete. Pietruszczak and Xu [82] performed a diagnostic strain localization analysis for plain concrete

subjected to plane strain uniaxial and biaxial compressions. They used a non-associative plasticity model and found that the increase in a confining pressure delayed the OSL. Salari et al. [83] developed a triaxial coupled elastic-plastic damage model for geo-materials. A Drucker-Prager yield function was used to illustrate the coupling of plasticity and elastic damage, and a non-associated flow rule was employed to control the inelastic dilatancy. Isotropic damage, represented by a scalar damage variable that evolved due to a volumetric expansion, was used. Salari et al. [83] conducted a diagnostic strain localization analysis for associated and non-associated coupled damage-plasticity models.

Beizaee [84] performed diagnostic strain localization analysis in a plain concrete. Drucker-Prager yield criterion was used in combination with scalar damage to model the constitutive behavior of the concrete. The main objective of this study was to compare the results of diagnostic strain localization analyses based on damage, plasticity, and coupled damage-plasticity models. Beizaee [84] used constitutive models that employed associated and non-associated flow rules.

To the best knowledge of authors, no previous significant attempts have been made towards conducting a diagnostic strain localization analysis in fiber-reinforced cementitious composites.

2.3. Test methods to characterize FRCC

As explained in the paragraph 2.1, HPFRCCs and UHPFRCCs usually have higher compressive strengths than plain non-reinforced concretes, more ductile post-cracking behavior under tension and higher energy absorption prior to macro-crack localization [33].

Currently, there is a hesitancy amongst engineers to use UHPFRCC in construction industry because there is no simple method to characterize the tensile properties for quality control purposes [85]. For a successful incorporation of FRCC into a design, standardized procedures for design must be established. This requires test methods that can correctly, and accurately, describe a constitutive behavior of the composite.

Post cracking tensile response of the FRCC structural member is one of the most important properties when considering design. Before cracking of the matrix, the characteristic behavior of FRCC in tension is typically represented by its stress-strain response. After cracking, the behavior is most commonly described by stress-crack opening displacement relationship.

A stress-crack opening relationship of FRCC can be obtained through: 1) a variety of direct tension tests or 2) indirect tension tests, such as prism bending test, round panel test, cylinder splitting test combined with an inverse analysis. Many more different test methods have been proposed by research bodies to characterize the post cracking behavior of FRCC. However, due to the scope of this review only two key tests in particular will be focused on: a direct tension test and prism bending tests.

Direct tension test is most direct way of collecting the information needed for determination of post cracking properties experimentally ([86], [87], [88], [89], [90], [32]). However, direct tension test, while simple in concept, requires attention to many details. More precisely, it is quite complicated and time consuming test, because the complexity of preparing the samples and test set-up is high. Moreover, it requires sophisticated testing equipment, which makes the test very cost effective.

A quicker and simpler alternative to the direct tension test is a prism bending test. Its advantages over the direct tension test are that it is fair easy to conduct, it has already been

standardized, which makes it a cheap and highly applicable test in practice. It must be noted that a prism bending test does not give direct post-cracking properties of the FRCC under a tensile loading. Therefore, an inverse analysis is needed in order to process test results and convert a load versus beam mid-span deflection to the corresponding stress-crack opening displacement. While the inverse analysis has been successfully used for well-researched materials such as plain concrete, the use of traditional inverse analysis technique might be problematic for the FRCC where a large number of parameters contribute to the post cracking strength of FRCC.

In what follows, background about direct testing and prism bending testing methods is presented.

2.3.1. Direct tension test

In this study both tests, a direct tension and prism bending test were performed on UHPFRCC. As mentioned previously, it is the use of prism bending tests only that requires an inverse analysis.

In general, when designing a reliable tensile test setup for determining the post cracking characteristics of SFRC, three fundamental technical elements should be considered. These technical elements include the geometry and alignment of the specimen, and the boundary conditions. There is a great debate within the scientific community as to which one is the most appropriate for this type of material and a wide range of experimental tensile tests and specimens have already been successfully used in the past and the results have been published, but no comprehensive agreed upon tensile standard has been published to the date. For the brief overview of different direct tension test setups reader is referred to Wille et al. [33].

The geometry of the sample is the first technical element which includes the shape, dimension and whether the specimen is notched or un-notched. The most common specimen shapes used in the direct tension test are prisms, cylinders, and so-called dog-bones, both notched and un-notched. A common drawback for un-notched prisms and cylinders is an occurrence of the stress concentration in the specimen near bond of the concrete specimen and the steel loading platens. These stress concentrations are due to a discrepancy in Young's modulus and Poisson's ratio of the concrete and steel and they often lead to a layer in the concrete close to the glue fails, i.e. to "bond failure" [91]. It is common practice to use notched specimens to avoid these bond failure occurrences. However, in the notched specimens, stress concentration will occur in the vicinity of the notch due to a sudden change in the cross section, which will further cause micro-cracks to form in that area and nowhere else in the specimen. Because capturing the multi-cracking behavior is one of the main goals of this research study, it will be proceeded with the un-notched specimens.

Bond failure and stress concentrations near the steel loading platens can be avoided by reducing the dimensions of the middle section of the specimen. That is the reason why so-called dog-bone shape of the specimen is the most frequently used specimen shape for the direct tensile testing.

Another highly important technical elements which need to be taken into account while designing uniaxial tensile test setup include the alignment of the specimen, and the boundary conditions. The type of the alignment of the specimen, and boundary conditions that should be applied to a uniaxial tension test continues to be an ongoing matter of discussion in the scientific community. In the term of transferring load from the machine to the specimen, specimens can be glued, anchored or clamped to the machine. For dog-bone shaped specimens, all of the methods

have been found applicable ([92], [33]). While designing tensile setup in this study, several different gripping arrangements and boundary conditions of a dog-bone specimen have been analyzed, such as glued, anchored, embedded rods, and combination of former three. After the complementation of the numerical simulations, rods embedded 125 mm into the specimen was chosen as an optimal gripping arrangement. Numerical simulations will be discussed later in the text.

Furthermore, the alignment of the specimen needs to be taken into account. There is significant discussion within the literature on whether the ends of uniaxial tension test specimens should be either fixed, pinned or a combination of both ([93], [87]). Fixed ends at each end of the specimen would prevent the rotation of the test specimen, while rotating ends would allow the specimen end to freely rotate about the center point. All of the variations of the ends have been used in direct tension test. In the ideal case scenario, the specimen should be fixed at each end. However, when fixed loading platens are used, the platens are forced to remain parallel during the crack propagation and it induces bending moment into the sample. The initial crack will occur in the specimen's weakest location, but due to this induced bending moment, the crack will be prevented from propagating further until the other side of the specimen begins to fracture. This will ultimately lead to a higher fracture toughness than can be achieved with free rotating boundary conditions ([89], [67]). To avoid this, Draft Australian Bridge Code DR AS5100.5: Concrete [94] adopted one fixed end and the other end fitted with a universal joint to eliminate any residual tension that may develop during the gripping process. The same testing arrangement, with one rotating and one fixed end for FRCC in uniaxial tension, was followed in this research study.

2.3.2. Prism bending test

As discussed, both direct uniaxial tension test and indirect prism bending test can be used to investigate the flexural strength, ductility, toughness and fracture behavior of the FRCC. Although, most direct way of gathering post cracking properties of UHPFRCC experimentally is a direct uniaxial tension test, there are, however, drawbacks of running direct tension tests on UHPFRCC. Therefore, prism bending test, whose conduction is quicker, cheaper, and easier, represents an interesting alternative and will be carried out in the research study ([89], [2], [85], [95]).

There exist two commonly used prism bending tests, namely, the three-point and four-point bending tests, both notched and un-notched at the beam mid-span (sometimes referred as flexural test) (Figure 2.8). Figure 2.8 contains the parameters *P* and *L,* which stand for the externally applied force and span length, respectively.

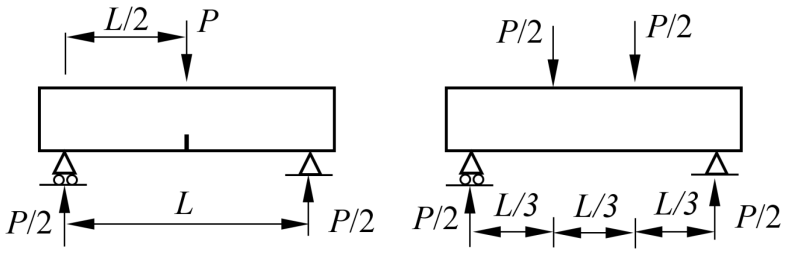

Figure 2.8 a) Three point notched prism bending test; b) four-point un-notched prism bending test

Similar as to direct tension test, there are different effects of notched and un-notched specimens, which were investigated by Wille et al. [33]. The advantage of a notch is that the specimen length can be reduced, since the specimen will fail in the notched region. Moreover,

the crack mouth opening displacement (CMOD) can be easily measured, and thus the direct relationship can be obtained between the applied moment and crack width. However, disadvantages arise due to the sudden change in cross section where stress localization occurs, leading to a crack predetermination and earlier crack initiation. Furthermore, because the failure plane in notched specimens is not necessarily the weakest cross section of the member per unit cross-sectional area, a large scatter of results can be obtained, which has been reported in di Prisco et al. [96]. Furthermore, fibers often cumulate in the bottom of the specimen and a notch could subtract a significant bending resource to the specimen [30]. Finally, the small height of the notch adds to the list of disadvantages because it does not allow the development of multiple cracks or the investigation of crack spacing or positioning which is very unlikely located at the exact position of the notch [89].

For the un-notched specimens tested in a four-point prism bending test, the first crack will appear at the weakest cross-section of the prism between the two loading points, and the likelihood of development of more than one crack in this region is high. As the prediction of the location of the crack initiation cannot be possible, it is difficult to measure the CMOD, thus results are commonly presented in terms of load versus mid-span deflection.

In summary, it was suggested that notched specimens have been designed to investigate the softening behavior of plain concrete and FRCC, while un-notched specimens are more suitable for the characterization of the strain hardening tensile behavior of FRCC. As capturing the multi-cracking behavior of strain hardening UHPFRCC is one of the main goals of this research study, it was proceeded with the un-notched specimens.

Nevertheless, in the prism bending, test stress distributions though the sample are more complex. Applied flexural loading on the beam creates a combination of tensile and compressive

stresses in prism specimens, i.e. there is no uniform tensile stress across the entire cross section anymore and the pure tensile capacity of concrete remains therefore unknown [97]. However, the test produces a load versus mid-span deflection curve, which needs to be complemented by inverse analysis in order to obtain the pure tensile properties of tested materials. Overview of current inverse analysis methodologies for determination of the stress-crack opening displacement relationship of FRCC from prism bending tests will be discussed in the following section.

Current inverse analysis methodologies

Although direct tensile test seems to provide the most direct tensile behavior, in some cases, such as an on-site quality control, when a large number of sampling in the field conditions precludes complicated testing, prism bending test seems to be a more suitable test. In order to determine a uniaxial tension behavior from a prism bending test, it is necessary to conduct an inverse analysis. Up to date, this approach has been investigated by number of researchers ([98], [88], [30]).

A prism bending test in a conjunction with the inverse analysis has been successful for well-researched materials such as plain concrete. However, modeling of the tensile behavior of FRCC is a complex task, due to a large variety of different parameters and phenomena affecting it. Thus, use of traditional inverse analysis techniques may be problematic. Due to such intricate behavior, there is not a single constitutive model, which can capture a tensile post-cracking behavior of FRCC. Up to date, numerous different constitutive models have been proposed in the literature and standards. Most of these models can be categorized into tensile stress-crack opening displacement (σ-w) and tensile stress-strain (σ-ε) models.

There have been numerous discussions among the research community and practitioners as to which constitutive law, σ-w or σ-ε, is more appropriate to model the post-cracking behavior of FRCCs. Because both approaches possess advantages and disadvantages, they are both accepted in the most recent recommendations for design of fiber reinforced concrete ([30], [12]).

The σ-w model is based on fracture mechanics concept of cohesive σ-w relationships, also known as a Fictitious Crack Model (FCM), which was originally developed by Hillerborg et al. [99]. Hillerborg et al. [99] suggested that a stress deformation relation can be divided into the σ-ε relationship up to the linear elastic part, which is followed by the σ-w relationship once a major macro-crack localization starts. This is applicable in the case of the tension softening FRCC [32] (Figure 2.9). As discussed earlier, in the case of the strain hardening FRCC, linear elastic part is followed by the multiple cracking stage, which occurs prior to a major macro-crack localization. According to the FCM model, linear elastic and strain hardening phases can be characterized by σ-ε relationship assuming smeared cracking approach for the multiple cracking stage. Once the macro crack localizes the σ-w relationship is used ([7], [33]).

The foremost advantage of using σ-w relationship is in that it can be directly compared to the experimental results at the material level, such as the one obtained from a direct tension test, thus providing an actual physical understanding of the mechanisms occurring in the FRCC [100].

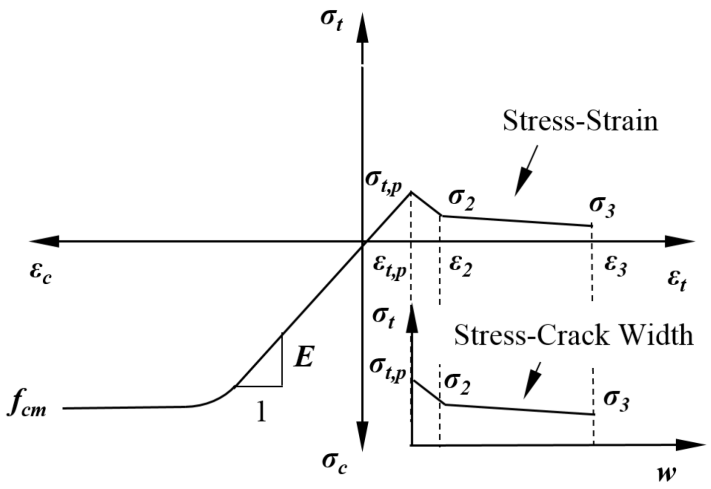

Figure 2.9 Illustration of the constitutive model for FRCC in terms of *σ-w* and tensile stress-strain, and *σ-ε* models for tensile strain softening FRCC (adapted from [100])

Furthermore, the foremost benefit of using *σ-ε* relationship to model the tensile behavior of FRCC is that a unique relation which represents the whole material in compression and tension can be used. The usage of *σ-ε* relationship is very useful in the structural design applications because it is compatible with other types of materials, such as in the case of traditional reinforced concrete.

There have been numerous studies in the literature focused on development of a specific relationship between tensile strain and crack opening displacement in order to connect continuous mechanics (*σ-ε* relationship) and fracture mechanics (*σ-w* relationship). This is most commonly resolved by introducing the characteristic length l_{cs}, which was initially proposed by Hillerborg et al. [99]. A characteristic length is a quantity which allows the strain to be defined as:

$$\varepsilon = w / l_{cs} \qquad \textbf{2.1}$$

In the case of concrete beams, a characteristic length is equal to average space between cracks when multiple cracking takes place, or in the case without multiple cracking it can be defined as a beam depth (for a rectangular cross-section) ([12], [30]).

In the case of σ-w constitutive models, the subsequent step of an inverse analysis procedure is to define the shape of a softening curve, which would reasonably and realistically represent the measured behavior. The most commonly used shapes of σ-w relationships are drop-constant, bi-linear, multi-linear, and free form relationships (Figure 2.10) [9].

Even though these shapes could be more complex, thus making the above representations seem to appear over-simplified, from a practical, structural design point of view the suggested representations are the limit [101].

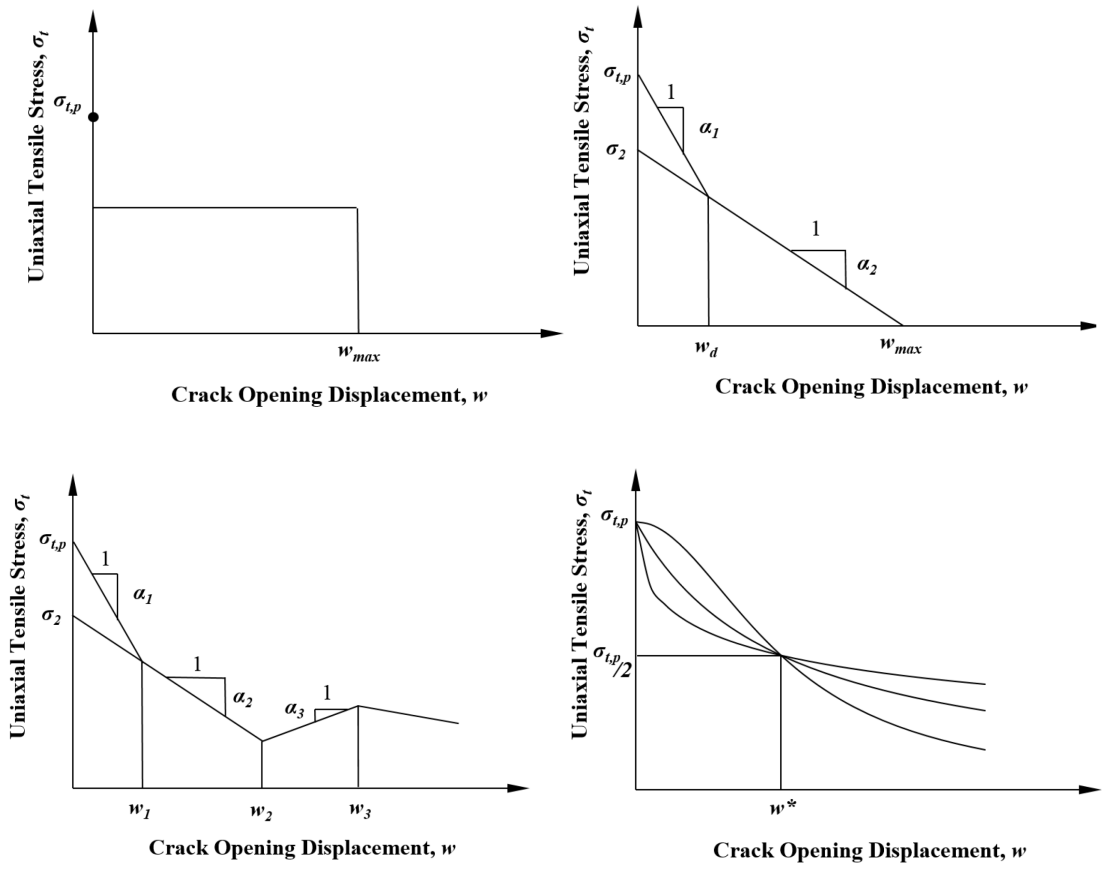

Figure 2.10 *σ-w* constitutive models for the characterization of tensile behavior of FRCC (adapted from [9])

After determination of a shape of the *σ-w* relationship, models parameters need to be identified from the experimentally obtained load versus displacement data. This is done by the iterative process (trial and error, or some other optimization technique) by varying constitutive parameters, until the analytical curve does not fit the experimental one. In the case that *σ-w* relationship is too simple, and it does not require many parameters, the procedure provides ambiguous results. On the other hand, if the *σ-w* relationship is too complex, more accurate results could be obtained but the iteration process can be too tedious.

The identification of the most appropriate constitutive law in uniaxial tension represents the critical step in the design of FRCC structures [30]. Although the research and development of

FRCC in both academia and industry dates to almost half century ago, there are only few national standards that deal with the design of FRCC structures in a comprehensive manner [32].

Over the past ten years several technical publications of design codes and recommendations can be found: the German code [102], the RILEM Scientific Committee 162 recommendations [9], the Italian guideline (2006), New Zealand Standard NZS 3101 [103], the Japanese JSCE Guidelines for Concrete No. 9 [11], the American Standard ACI-544 [10], the Spanish code (2008) and the *fib* Model Code 2010 (*fib* MC2010) [30], French Association for Civil Engineering recommendations on Ultra-High Performance Fibre-Reinforced Concrete [12], and most recently, the Draft Australian Bridge Code DR AS5100.5: Concrete [94].

Given the variety of the existing constitutive models and recommendation, the Chapter 5 will set more detailed focus on several models, namely: Amin's full model (Amin-FM) [32], Amin's simplified model (Amin-SM) [32], and Lopez's model [7]. Amin's model [32] is an alternative model for the *fib* MC2010 [96]. The latter is the most recent design guideline and the document of reference for Eurocode 2 (European code for design of concrete structures) and other national guidelines. It was found in Amin [32] that *fib* MC2010 overestimates the residual tensile strength. Moreover, a simplified version of the model can be found in the Draft Australian Bridge Code: Concrete [94]. Finally, the inverse analysis based on Lopez's model [7] is also selected because it is the most recent model developed specifically for the UHPFRCC from un-notched four-point prism bending tests, which correspond to the experimental study performed in this research.

Chapter 3 - Strain localization analysis for HPFRCC

3.1. Introduction

This Chapter presents a computational modelling of a stress-strain response and diagnostic strain localization analysis for HPFRCC. It is because the onset of strain localization is a failure precursor that the analysis can evaluate effectiveness of short discrete steel fibers on favorably modifying the inception of strain localization. This includes effects of a presence of fibers on the critical stress level, localization direction and mode.

HPFRCC is modelled by embedding multidirectional elastic fibers into an elastic-plastic matrix. The resulting HPFRCC is described by three different two-invariant Drucker-Prager hardening plasticity models, including a linear Drucker-Prager (LDP), a hyperbolic Drucker-Prager (HDP), and an exponential Drucker-Prager (EDP) plasticity models with isotropic hardening. In addition, in order to investigate the effect of hardening type on the inception of strain localization, two types of isotropic hardening laws were used: linear and nonlinear hardening. Furthermore, a simple volume-based homogenization procedure was used to derive the corresponding macroscopic elastic tangent stiffness moduli tensor of the fiber-reinforced composite. Actual uniaxial tension (UT) and uniaxial compression (UC) tests on non-reinforced mortar and on a HPRFCC were modeled.

3.2. Fiber contribution

In the theory of composite materials, a representative volume element (RVE) is the smallest volume over which a measurement yields a value representative of a whole. The RVE is herein assumed to have a cubical shape. The side length of the RVE corresponds to two times the

length of a fiber l_f (Figure 3.1). Furthermore, fibers are isotropically distributed throughout the RVE, and they have a cylindrical shape with a diameter d_f, length l_f, and an aspect ratio (length to diameter) η_f. A macroscopic tangent stiffness moduli tensor of the composite was developed by consistently homogenizing the contribution of fibers in the RVE ([104], [105]). It contains the essential information about fibers, including their aspect ratio and direction, and number of fibers in the RVE. Because composite properties are controlled by the relative volume of fiber and matrix used, the volumetric fiber content χ_f is expressed as a ratio between the volume of fibers and the volume of the cubical RVE as follows:

$$\chi_f = \frac{V_f}{V} = \frac{n_f \pi}{32\eta_f^2} \qquad \textbf{3.1}$$

where V_f is the volume of fibers contained in RVE, V is the volume of the RVE, and n_f is the total number of fibers in the RVE.

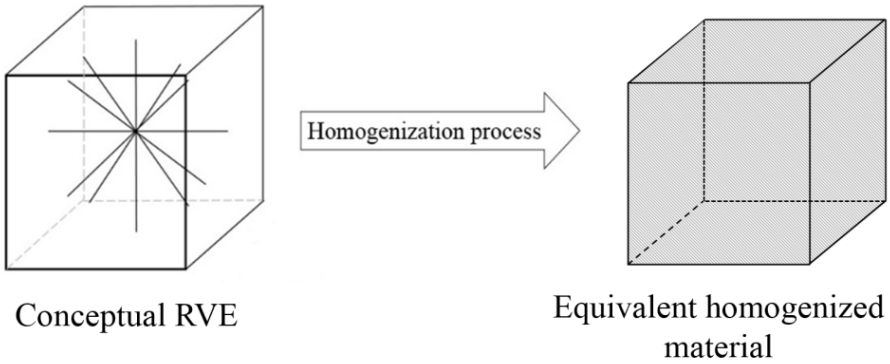

Figure 3.1 Homogenization process

Isotropic distribution of fibers in the cubical RVE was obtained by arranging fibers in such a way that each fiber connects the center and a vertex of a geodesic sphere, as shown in the cubical RVE (Figure 3.2). The center of the geodesic sphere corresponds to the origin of the Cartesian coordinate system depicted in Figure 3.2. The direction of a fiber is defined by its unit

vector N_m. Therefore, for any fiber m, Cartesian components of its direction vector N_m are given by:

$$N_{1(m)} = \sin\bar{\theta}_m \sin\varphi_m, \qquad N_{2(m)} = \cos\bar{\theta}_m, \qquad N_{3(m)} = \sin\bar{\theta}_m \cos\varphi_m \tag{3.2}$$

where angles $\bar{\theta}_m$ and φ_m are shown in Figure 3.2.

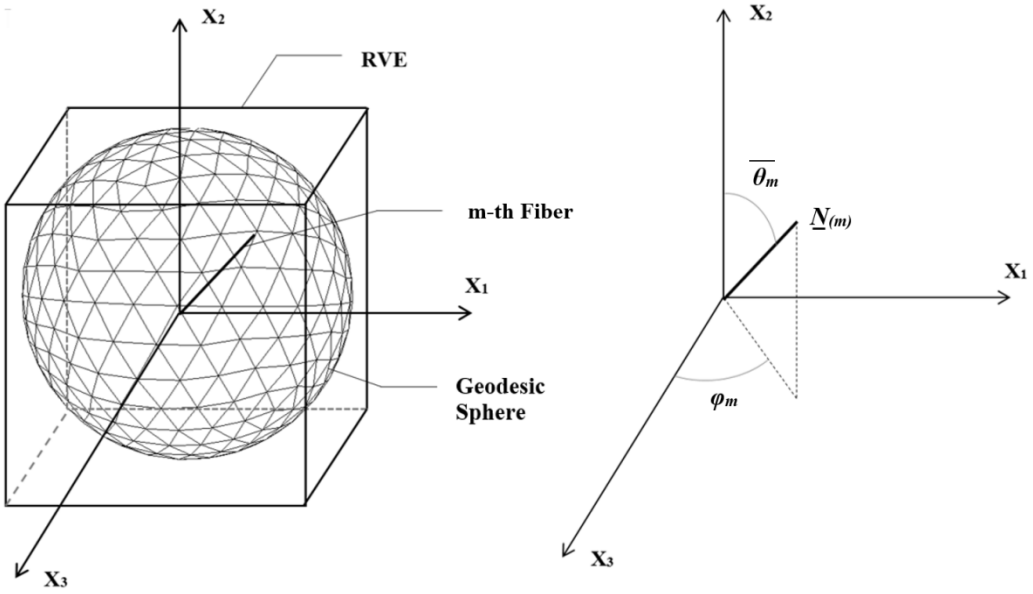

Figure 3.2 Distribution of fibers in the cubical RVE

A three-dimensional elastic stiffness moduli tensor $D^e_{ijkl,f}$, which describes elastic contribution of fibers is given by:

$$D^e_{ijkl,f} = \frac{E_f}{n_f}\sum_{m=1}^{n_f} N_{i(m)}N_{j(m)}N_{k(m)}N_{l(m)} \tag{3.3}$$

where E_f is simply an elastic modulus of a fiber and m is the summation index. Fibers embedded in a matrix can carry compressive and tensile loads.

3.3. Stress-strain relationship

The cementitious composite was assumed to be an elastic-plastic material experiencing an infinitesimal strain and obeying a general non-associative flow rule. Normal components of stress and strain tensors are positive in tension. The macroscopic stress-strain relationship for a plastic loading is given by:

$$\dot{\sigma}_{ij} = D^e_{ijkl}(\dot{\varepsilon}_{kl} - \dot{\varepsilon}^p_{kl}) \quad \textbf{3.4}$$

where $\dot{\sigma}_{ij}$, $\dot{\varepsilon}_{ij}$, and $\dot{\varepsilon}^p_{ij}$ are rates of the Cauchy stress tensor, infinitesimal strain tensor, and plastic strain tensor, respectively. D^e_{ijkl} is the corresponding elastic stiffness moduli tensor of the homogenized equivalent isotropic material depicted in Figure 3.1. Thus, an elastic stiffness moduli tensor of the composite is defined as a weighted sum of the elastic stiffness moduli tensors of the matrix and of fibers. It is given by:

$$D^e_{ijkl} = (1-\chi_f)D^e_{ijkl,m} + \chi_f D^e_{ijkl,f} = \mu(\delta_{ik}\delta_{jl} + \delta_{jk}\delta_{il}) + \lambda\delta_{ij}\delta_{kl} \quad \textbf{3.5}$$

where $D^e_{ijkl,f}$ was given in Eq. 3.3, while an elastic stiffness moduli tensor of the matrix is given by:

$$D^e_{ijkl,m} = \mu_m(\delta_{ik}\delta_{jl} + \delta_{jk}\delta_{il}) + \lambda_m\delta_{ij}\delta_{kl} \quad \textbf{3.6}$$

and δ_{ij} is Kronecker delta, μ_m and λ_m are Lamé's constants of the matrix, and μ and λ are Lamé's constants of the composite.

The two-invariant yield function was used to describe a plastic behavior of a pressure-sensitive matrix. It is defined as:

$$\bar{F} = \bar{F}(\sigma_{ij}, \kappa) \quad \textbf{3.7}$$

where κ is a plastic hardening variable.

The plastic flow rule and hardening law are respectively given by:

$$\dot{\varepsilon}_{ij}^{p} = \dot{\lambda}\frac{\partial G}{\partial \sigma_{ij}} \tag{3.8}$$

and

$$\dot{\kappa} = h\left(\dot{\varepsilon}^{p}\right) = \dot{\lambda}h\left(\frac{\partial G}{\partial \sigma_{ij}}\right) \tag{3.9}$$

where $\dot{\lambda} \geq 0$ is a plastic multiplier, $h(\dot{\varepsilon}_{ij}^{p})$ is the first order homogeneous but generally nonlinear function, while *G* is a plastic potential function. In order to realistically model the behavior of pressure sensitive materials such as cementitious composites, the non-associative flow rule should be used, especially when modeled in compression [73].

A plastic multiplier $\dot{\lambda}$ is obtained from the consistency condition in plastic loading. It is given by:

$$\dot{\lambda} = \frac{f_{ij}D^{e}_{ijkl}\dot{\varepsilon}_{kl}}{H + f_{ij}D^{e}_{ijkl}g_{kl}} \tag{3.10}$$

where gradients of a yield function and plastic potential are denoted by f_{ij} and g_{ij}, respectively. An actual hardening modulus *H* is given by:

$$H = -\frac{\partial F}{\partial \kappa}h(g_{ij}) \tag{3.11}$$

It is positive, negative, or zero for hardening, softening, or perfect plasticity, respectively.

By combining Eqs. 3.4, 3.8, and 3.10, a tangent elastic-plastic stiffness moduli tensor D^{ep}_{ijkl} is obtained as:

$$D^{ep}_{ijkl} = D^{e}_{ijkl} - \frac{D^{e}_{ijmn}g_{mn}f_{pr}D^{e}_{prkl}}{H + f_{mn}D^{e}_{mnpr}g_{pr}} \tag{3.12}$$

The yield function and rate of plastic multiplier satisfy Kuhn-Tucker conditions as follows:

$$\dot{\lambda} \geq 0\,,\ F(\sigma,\kappa) \leq 0 \qquad \textbf{3.13}$$

Onset of strain localization as given by Rudnicki and Rice [106] corresponds to the singularity of a so called acoustic tensor for plastic/plastic localization whereby the material on both sides of discontinuity responds plastically. The condition is given by:

$$Q_{ik} z_k = n_i D^{ep}_{ijkl} n_l z_k = 0 \qquad \textbf{3.14}$$

where Q_{ik} is an acoustic tensor, where n_i is unit vector perpendicular to a singular surface, and z_k is an eigenvector, which is unknown at this stage. Runesson et al. [107] showed that plastic/plastic localization precedes elastic/plastic localization in three invariant elastic-plastic materials.

To obtain critical hardening modulus, which corresponds to Eq. 3.14 and localization direction, the eigenvalue problem is formulated and solved. It was given by Runneson et al. [107]:

$$Q_{ik} z^{(i)}_k = \Lambda^{(i)} Q^e_{ik} z^{(i)}_k \qquad \textbf{3.15}$$

where Λ is an eigenvalue, and Q^e_{ij} is an elastic stiffness tensor. The analysis here is performed for plane stress state, thus resulting in a two dimensional eigenvalue problem. Consequently, it has two eigenvalues out of which one is elastic and the other one elastic. The critical amount of hardening and the corresponding hardening modulus is obtained by setting the plastic eigenvalue equal to zero [107], which gives:

$$H_{cr} = -f_{ij} D^e_{ijkl} g_{kl} + a_i P^e_{ij} b_j \qquad \textbf{3.16}$$

where P^e_{ij} is the inverse of the elastic stiffness tensor Q^e_{ij}

The vectors a_i, and b_i are defined as:

$$a_i = f_{mn} D^e_{mnij} b_j \qquad \textbf{3.17}$$

$$b_i = n_j D^e_{ijst} g_{st} \tag{3.18}$$

The corresponding eigenvector was given by Runesson et al. [107] as:

$$z_i^{(1)} = k P^e_{ij} b_j \tag{3.19}$$

where k is an arbitrary scalar.

After rearranging Eq. 3.19, the eigenvector for plane stress can be expressed as:

$$\frac{z_i}{k} = -(1+\nu)(n_j g_{jk} n_k) n_i + 2 n_k g_{ki} + \nu g_{mm} n_i \tag{3.20}$$

Furthermore, Eq. 3.14 results from imposing equilibrium and kinematic conditions across a strong discontinuity [107]. A kinematic condition assumes that there is a zero jump in a displacement rate across a singular surface, which results in the following jump in the strain rate:

$$\left[\dot{\varepsilon}_{ij}\right] = \frac{1}{2}\left(z_i n_j + z_j n_i\right) \tag{3.21}$$

Thus, a jump in the volumetric strain rate, $\dot{\varepsilon}_v$ is given by:

$$\left[\dot{\varepsilon}_v\right] = z_i n_i = \left|z_i\right| \cos\gamma \tag{3.22}$$

Thus, a magnitude of the jump in volumetric strain rate depends on the angle γ between the vectors n_i and z_i. This angle determines a mode of strain localization as follows:

$$\gamma = \begin{cases} 0^0, \text{ dilation band} \\ 0^\circ \le \gamma \le 90^\circ, \text{ dilatant shear band} \\ 90^\circ, \text{ pure shear band} \\ 90^\circ \le \gamma \le 180^\circ, \text{ contractant shear band} \\ 180^\circ, \text{ compaction band} \end{cases} \tag{3.23}$$

3.4. Application to Drucker-Prager models

As mentioned previously, three types of two-invariant Drucker-Prager models were used in this study: LDP, HDP, and EDP models [108]. Solutions for the OSL for these models are presented in the following sections.

3.4.1. Linear Drucker-Prager model

LDP yield and plastic potential functions respectively are given by:

$$\bar{F}(\sigma,\kappa) = q - p\tan\beta - d \tag{3.24}$$

$$G(\sigma) = q - p\tan\psi \tag{3.25}$$

where p and q are stress tensor invariants defined by:

$$p = -\frac{1}{3}\sigma_{kk}, \qquad q = \left(\frac{3}{2}s_{ij}s_{ij}\right)^{\frac{1}{2}} \tag{3.26}$$

and s_{ij} is the stress deviator tensor. Angles β and ψ represent an internal friction and dilatancy, while parameter d represents cohesion.

Gradients of LDP yield and plastic potential functions are given by:

$$f_{ij} = \frac{3}{2}\frac{s_{ij}}{q} + \frac{\tan\beta}{3}\delta_{ij} \tag{3.27}$$

$$g_{ij} = \frac{3}{2}\frac{s_{ij}}{q} + \frac{\tan\psi}{3}\delta_{ij} \tag{3.28}$$

While solving for critical hardening modulus Runesson et al. [107] introduced functions c_1 and c_2, which in the case of LDP, are given by:

$$c_1 = \frac{(s_1 - s_2)(9s_1 + q(\tan\beta + \tan\psi)}{2q} \quad \text{and} \quad c_2 = \frac{(s_1 - s_2)(9s_2 + q(\tan\beta + \tan\psi)}{2q} \tag{3.29}$$

It is noted that c_1 and c_2 are scalar functions, and not the above eigenvectors. Depending on the values of c_1 and c_2, the following three cases for critical hardening moduli H_{cr} and strain localization directions θ can be distinguished:

Case (i): $c_1 \geq 0$ and $c_2 \leq 0$

$$H_{cr} = \frac{\mu(3\lambda + 2\mu)}{36(\mu + \lambda)}(\tan\beta - \tan\psi)^2 \geq 0 \text{ and } \tan^2\theta = -\frac{9s_1 + q(\tan\beta + \tan\psi)}{9s_2 + q(\tan\beta + \tan\psi)} \quad \textbf{3.30}$$

Case (ii): $c_1 \leq 0$ and $c_2 \leq 0$

$$H_{cr} = -\frac{\mu(3\lambda + 2\mu)}{36(\mu + \lambda)}\frac{(9s_1 + 2q\tan\beta)(9s_1 + 2q\tan\psi)}{q^2} \quad \text{and} \quad \theta = 0^\circ \quad \textbf{3.31}$$

Case (iii): $c_1 \geq 0$ and $c_2 \geq 0$

$$H_{cr} = -\frac{\mu(3\lambda + 2\mu)}{36(\mu + \lambda)}\frac{(9s_2 + 2q\tan\beta)(9s_2 + 2q\tan\psi)}{q^2} \quad \text{and} \quad \theta = 90^\circ \quad \textbf{3.32}$$

where θ denotes the angle in the x_1, x_2-plane from the unit normal n_i to the x_2 axis defining the strain localization direction. Furthermore, x_1 is oriented in the direction of the major in plane principal stress.

3.4.2. Hyperbolic Drucker-Prager model

The HDP model is a continuous combination of the LDP model at high confining stress and Rankine's maximum tensile stress criterion. The corresponding yield function is given by:

$$\overline{F}(\sigma, \kappa) = \sqrt{(d'_0 - p_{t0}\tan\beta)^2 + q^2} - p\tan\beta - d' \quad \textbf{3.33}$$

where p_{t0} is an initial hydrostatic tensile yield stress of a material, d' is a hardening parameter, d_0' is an initial value of d', and β corresponds to a friction angle measured at a high confining pressure. Therefore, a gradient of the yield surface in Eq. 3.33 is given by:

$$f_{ij} = \frac{3}{2}\frac{s_{ij}}{\sqrt{(d'_0 - p_{t0}\tan\beta)^2 + q^2}} + \frac{\tan\beta}{3}\delta_{ij}. \quad \textbf{3.34}$$

The plastic potential function for HDP model is given by:

$$G(\sigma) = \sqrt{(\grave{o}\sigma_0 \tan\psi)^2 + q^2} - p\tan\psi \quad \textbf{3.35}$$

where ϵ is a parameter referred to as eccentricity. It defines the rate at which the function G approaches its asymptote, and σ_0 is an initial hydrostatic yield stress. Consequently, a gradient of the plastic potential function is given by:

$$g_{ij} = \frac{3}{2\sqrt{(\grave{o}\sigma_0 \tan\psi)^2 + q^2}} s_{ij} + \frac{1}{3}\tan\psi\delta_{ij} \quad \textbf{3.36}$$

For HDP, functions c_1 and c_2 are given by:

$$c_1 = \frac{(s_1 - s_2)\left(9s_1 + \tan\beta\sqrt{(d'_0 - p_{t0}\tan\beta)^2 + q^2} + \tan\psi\sqrt{(\grave{o}\sigma_0\tan\psi)^2 + q^2}\right)}{2\sqrt{(d'_0 - p_{t0}\tan\beta)^2 + q^2}\sqrt{(\grave{o}\sigma_0\tan\psi)^2 + q^2}} \quad \textbf{3.37}$$

and

$$c_2 = \frac{(s_1 - s_2)\left(9s_2 + \tan\beta\sqrt{(d'_0 - p_{t0}\tan\beta)^2 + q^2} + \tan\psi\sqrt{(\grave{o}\sigma_0\tan\psi)^2 + q^2}\right)}{2\sqrt{(d'_0 - p_{t0}\tan\beta)^2 + q^2}\sqrt{(\grave{o}\sigma_0\tan\psi)^2 + q^2}} \quad \textbf{3.38}$$

The critical hardening moduli and strain localization directions are given by:

Case (i): $c_1 \geq 0$ and $c_2 \leq 0$

$$H_{cr} = \frac{\mu(3\lambda + 2\mu)}{36(\mu + \lambda)}\frac{(\tan\beta\sqrt{(d'_0 - p_{t0}\tan\beta)^2 + q^2} - \tan\psi\sqrt{(\grave{o}\sigma_0\tan\psi)^2 + q^2})^2}{\sqrt{(d'_0 - p_{t0}\tan\beta)^2 + q^2}\sqrt{(\grave{o}\sigma_0\tan\psi)^2 + q^2}} \geq 0 \quad \textbf{3.39}$$

and

$$\tan^2\theta = -\frac{9s_1 + \tan\beta\sqrt{(d'_0 - p_{t0}\tan\beta)^2 + q^2} + \tan\psi\sqrt{(\grave{o}\sigma_0\tan\psi)^2 + q^2}}{9s_2 + \tan\beta\sqrt{(d'_0 - p_{t0}\tan\beta)^2 + q^2} + \tan\psi\sqrt{(\grave{o}\sigma_0\tan\psi)^2 + q^2}} \quad \textbf{3.40}$$

Case (ii): $c_1 \le 0$ and $c_2 \le 0$

$$H_{cr} = -\frac{\mu(3\lambda + 2\mu)}{36(\mu + \lambda)}\frac{(9s_1 + 2\tan\beta\sqrt{(d'_0 - p_{t0}\tan\beta)^2 + q^2})(9s_1 + 2\tan\psi\sqrt{(\grave{o}\sigma_0\tan\psi)^2 + q^2})}{\sqrt{(d'_0 - p_{t0}\tan\beta)^2 + q^2}\sqrt{(\grave{o}\sigma_0\tan\psi)^2 + q^2}} \quad \textbf{3.41}$$

and

$$\theta = 0^\circ \quad \textbf{3.42}$$

Case (iii): $c_1 \ge 0$ and $c_2 \ge 0$

$$H_{cr} = -\frac{\mu(3\lambda + 2\mu)}{36(\mu + \lambda)}\frac{(9s_1 + 2\tan\beta\sqrt{(d'_0 - p_{t0}\tan\beta)^2 + q^2})(9s_1 + 2\tan\psi\sqrt{(\grave{o}\sigma_0\tan\psi)^2 + q^2})}{\sqrt{(d'_0 - p_{t0}\tan\beta)^2 + q^2}\sqrt{(\grave{o}\sigma_0\tan\psi)^2 + q^2}} \quad \textbf{3.43}$$

and

$$\theta = 90^\circ \quad \textbf{3.44}$$

3.4.3. Exponential Drucker-Prager model

An initial yield function of the EDP model is given by:

$$\bar{F} = aq^b - p - p_{t0} \quad \textbf{3.45}$$

where a and b are material parameters, which are independent of plastic deformation.

For EDP, a gradient of the yield function is:

$$f_{ij} = ab\frac{3}{2}q^{b-2}s_{ij} + \frac{1}{3}\delta_{ij}\,. \quad \textbf{3.46}$$

The plastic potential function G and its gradient are given by Eqs. 3.35 and 3.36, respectively.

Expressions for c_1 and c_2 are given by:

$$c_1 = \frac{3}{2}\frac{(s_1 - s_2)}{\sqrt{(\dot{\sigma}_0 \tan\psi)^2 + q^2}}\left(3abq^{b-2}s_1 + \frac{1}{3}\left(1 + \tan\psi abq^{b-2}\sqrt{(\dot{\sigma}_0 \tan\psi)^2 + q^2}\right)\right) \quad \textbf{3.47}$$

and

$$c_2 = \frac{3}{2}\frac{(s_1 - s_2)}{\sqrt{(\dot{\sigma}_0 \tan\psi)^2 + q^2}}\left(3abq^{b-2}s_2 + \frac{1}{3}\left(1 + \tan\psi abq^{b-2}\sqrt{(\dot{\sigma}_0 \tan\psi)^2 + q^2}\right)\right) \quad \textbf{3.48}$$

Finally, the solutions for the critical hardening moduli and corresponding strain localization directions are given by:

Case (i): $c_1 \geq 0$ and $c_2 \leq 0$

$$H_{cr} = \frac{\mu(3\lambda + 2\mu)}{36(\mu + \lambda)}\frac{q^{-(b+2)}(q^2 - abq^b \tan\psi\sqrt{(\dot{\sigma}_0 \tan\psi)^2 + q^2})^2}{ab\sqrt{(\dot{\sigma}_0 \tan\psi)^2 + q^2}} \geq 0 \quad \textbf{3.49}$$

and

$$\tan^2\theta = -\frac{q^2 + abq^b(9s_1 + \tan\psi\sqrt{(\dot{\sigma}_0 \tan\psi)^2 + q^2})}{q^2 + abq^b(9s_1 + \tan\psi\sqrt{(\dot{\sigma}_0 \tan\psi)^2 + q^2})} \quad \textbf{3.50}$$

Case (ii): $c_1 \leq 0$ and $c_2 \leq 0$

$$H_{cr} = -\frac{\mu(3\lambda + 2\mu)}{(\mu + \lambda)}\left(\frac{1}{3} + \frac{3}{2}abq^{b-2}s_1\right)\left(\frac{3s_1}{2\sqrt{(\dot{\sigma}_0 \tan\psi)^2 + q^2}} + \frac{\tan\psi}{3}\right) \quad \textbf{3.51}$$

and

$$\theta = 0^\circ \quad \textbf{3.52}$$

Case (iii): $c_1 \geq 0$ and $c_2 \geq 0$

$$H_{cr} = -\frac{\mu(3\lambda + 2\mu)}{(\mu + \lambda)}\left(\frac{1}{3} + \frac{3}{2}abq^{b-2}s_2\right)\left(\frac{3s_2}{2\sqrt{(\dot{\sigma}_0 \tan\psi)^2 + q^2}} + \frac{\tan\psi}{3}\right) \quad \textbf{3.53}$$

and

$$\theta = 90^{\circ} \tag{3.54}$$

Once the solution for a critical hardening modulus is obtained, detection of the OSL can be performed by comparing values of the actual and critical hardening moduli. Actual hardening modulus H_{act} is obtained by numerical differentiation of the actual stress-plastic strain response obtained from ABAQUS [108]. Inception of strain localization occurs when the actual hardening modulus is equal to the critical hardening modulus.

3.5. Calibration of constitutive models

Drucker-Prager models were calibrated based on UT, UC, and conventional triaxial compression (CTC) experiments, which were carried out at confining pressures of 41 and 52 MPa. The experiments were performed on plain mortar and on HPFRCC [61]. According to Sirijaroonchai [61] experimental data for each test represented the average of eight experiments.

As shown in Table 3.1, eight material parameters were determined during the calibration procedure of the Drucker-Prager models. Although experimental data are available for four volumetric fiber contents (0%, 1%, 1.5%, and 2%), the data for only three fiber contents (0%, 1%, and 2%) were used during the calibration procedure.

The modulus of elasticity, $E_{m,}$ and Poisson's ratio, $v_{m,}$ of the matrix were determined based on experiments performed on plain mortar. Modulus of fiber, $E_{f,}$ was provided by Sirijaroonchai [61] and Poisson's ratio of fiber, $v_{f,}$ was determined in accordance with Eq. 3.5. The data presented in Table 3.1 show that the value of the modulus of elasticity, $E,$ of the HPFRCC slightly increased with the increasing volumetric fiber content. The most often-found

values of Poisson's ratio, v, of the HPFRCC in the literature range from 0.2 to 0.25 ([109], [10], [110], [111]). In addition, these authors also found that the average Poisson's ratio v remained unchanged regardless of the fiber content and type. ACI Committee 544 [10] suggested that, in the case of fiber-reinforced cementitious composites with volumetric fiber content smaller than 2%, Poisson's ratio v, should be equal to that of a similar non-reinforced concrete. This is in a good agreement with analytically obtained values of Poisson's ratio v in this research.

Plastic properties differed for each elastic-plastic model. Parameters β and d of the LDP model, which are related to the mobilized internal friction and cohesion, were determined based on the stress states at the onset of yielding in UC and CTC tests. They are provided in Table 3.1. The angle β for the HDP model was equal to the one used by the LDP model. The initial hydrostatic yield stress p_{to}, was obtained by the best fit of HDP yield surface to stress states at the onset of yielding plotted in q-p plane for UT, UC, and CTC tests.

Furthermore, plastic input parameters required by the EDP model were a, b, and p_{t0} (Eq. 3.45). They were determined on the basis of the best fit with corresponding experimental data at the onset of yielding in the UT, UC, and two CTC tests at different confining pressures. In order to achieve the best fit values for the input parameters, the least-squares fit that minimized the relative error with respect to experimental data was used.

For a non-associated flow all plasticity models require the value of a dilation angle, ψ. Chi et al. [112] found that an increase in volumetric fiber content increased the non-associativity of the composite. In other words, the presence of fibers effectively restrained plastic dilation. Values of dilation angles summarized in Table 3.1 were determined using the data presented by Chi et al. [112] because Sirijaroonchai [61] did not provide volumetric response in UT, UC, and CTC experiments.

Table 3.1 Elastic and plastic input parameters for Drucker-Prager models

Property	Mortar	HPFRCC-1	HPFRCC-1.5	HPFRCC-2
χ_f *(%)*	0	1	1.5	2
E (GPa)	26.58	26.66	26.69	26.72
v	0.2	0.2007	0.2011	0.2014
β (°)	28	31	31	30
d (MPa)	37.3	34.3	34.4	35.7
a $(x10^{-4})$	4	7.3	7.4	6.5
b	2.8	2.65	2.64	2.67
p_t (MPa)	0.27	0.38	0.4	0.41
ψ (°)	22	15	13	11

Isotropic hardening was used in all models. A hardening function was prescribed in a tabular form based on the experimental data from uniaxial tests. For non-reinforced cementitious composites, the assumption was made that deviatoric stress at the onset of yielding coincided with the peak deviatoric stress in UT, thus resulting in no hardening. For non-reinforced cementitious composites in UC and HPFRCCs, two types of hardening laws were investigated, linear and nonlinear.

3.6. Predictions

HDP and EDP plasticity models were used for simulations of the plane stress UT test. The LDP plasticity model was disregarded because it significantly overestimated yield and peak stress states in the tensile region. Comparisons between the experimentally observed and numerically predicted axial responses in UT for the HDP and EDP models are shown in Figure 3.3 and Figure 3.4, respectively.

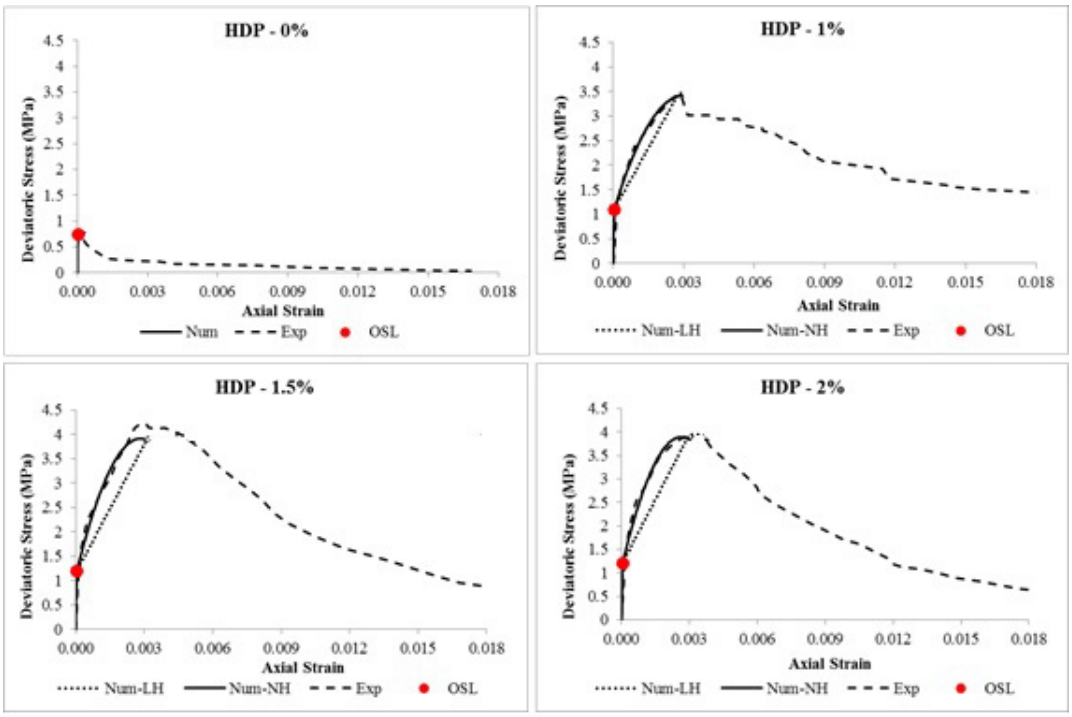

Figure 3.3 Experimentally observed and numerically predicted responses in UT for HDP model with linear and nonlinear hardening (HPFRCC with χ_f of 0%, 1%, 1.5% and 2%)

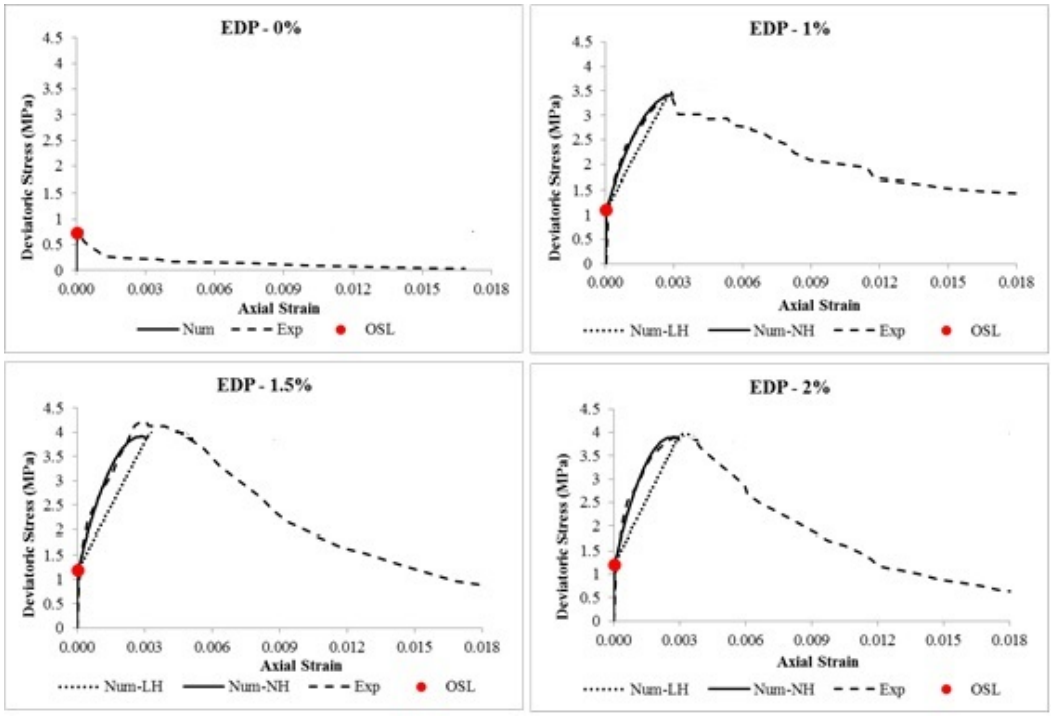

Figure 3.4 Experimentally observed and numerically predicted responses in UT for EDP model with linear and nonlinear hardening (HPFRCC with χ_f of 0%, 1%, 1.5% and 2%)

Based on Figure 3.3 and Figure 3.4, especially for χ_f = 1.5%, which was not used for calibration, a very good agreement was observed in the pre-peak stress-strain response between numerical and experimental data for the UT test, whereby the model with nonlinear hardening gave more accurate predictions. The predicted axial strain level at the OSL in the plain mortar coincided with the axial strain level at which a severe post peak drop in deviatoric stress began, thus signifying a major crack localization. It is noted that all ABAQUS predictions in this Chapter are essentially at the constitutive level, which is valid only prior to the crack localization. A post-cracking response is addressed in Chapter 5.

While Figure 3.3 and Figure 3.4 show that addition of fibers slightly increased the axial stresses at yielding and OSL it significantly increased the peak axial stress and improved the tensile strain capacity. For example, the axial yield stress was approximately 0.77 MPa for unreinforced mortar. By increasing the volumetric fiber content to 1% the axial yield stress increased to approximately 1.2 MPa. However, the peak axial stresses of HPRFCCs were at least five times higher than the peak axial stress of the plain cementitious composite. The predicted OSL coincided very closely with the onset of yielding in all cementitious composites in all UT tests. Thus, it appears that the principal mechanism of the delayed OSL in the UT tests was a fiber-induced slight increase in the yield stress. Furthermore, experimental data and numerical predictions indicated that OSL in plain mortar coincided with the formation of a major crack while in HPFRCC the OSL indicated the inception of distributed cracking. Thus, the major crack localization was delayed through the fiber induced distributed cracking. LDP and EDP models were chosen to simulate the plane stress UC test. The HDP model was not used in the simulations because it significantly over estimates the corresponding stress-strain response. Figure 3.5 and Figure 3.6 depict numerically predicted responses according for LDP and EDP

models respectively. Since experimental data are available only for axisymmetric UC tests [61], experimentally observed responses were not included in Figure 3.5 and Figure 3.6.

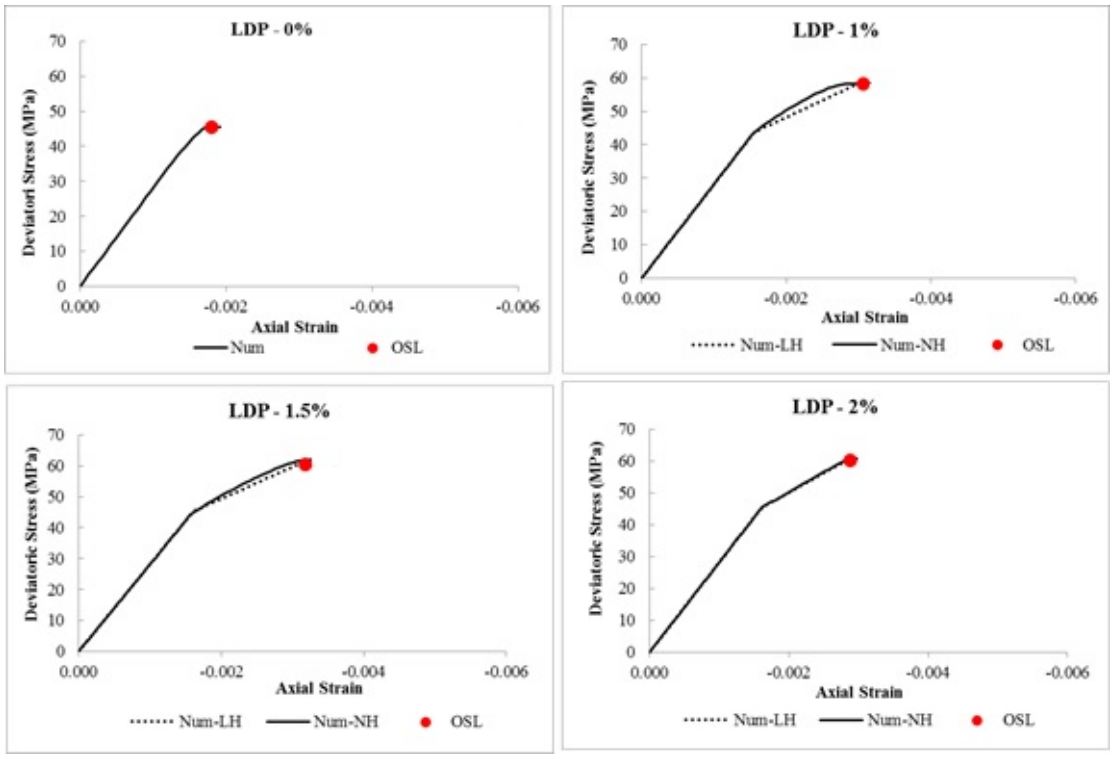

Figure 3.5 Numerically predicted responses in UC for LDP model with linear and nonlinear hardening (HPFRCC with volumetric fiber contents of 0%, 1%, 1.5% and 2%)

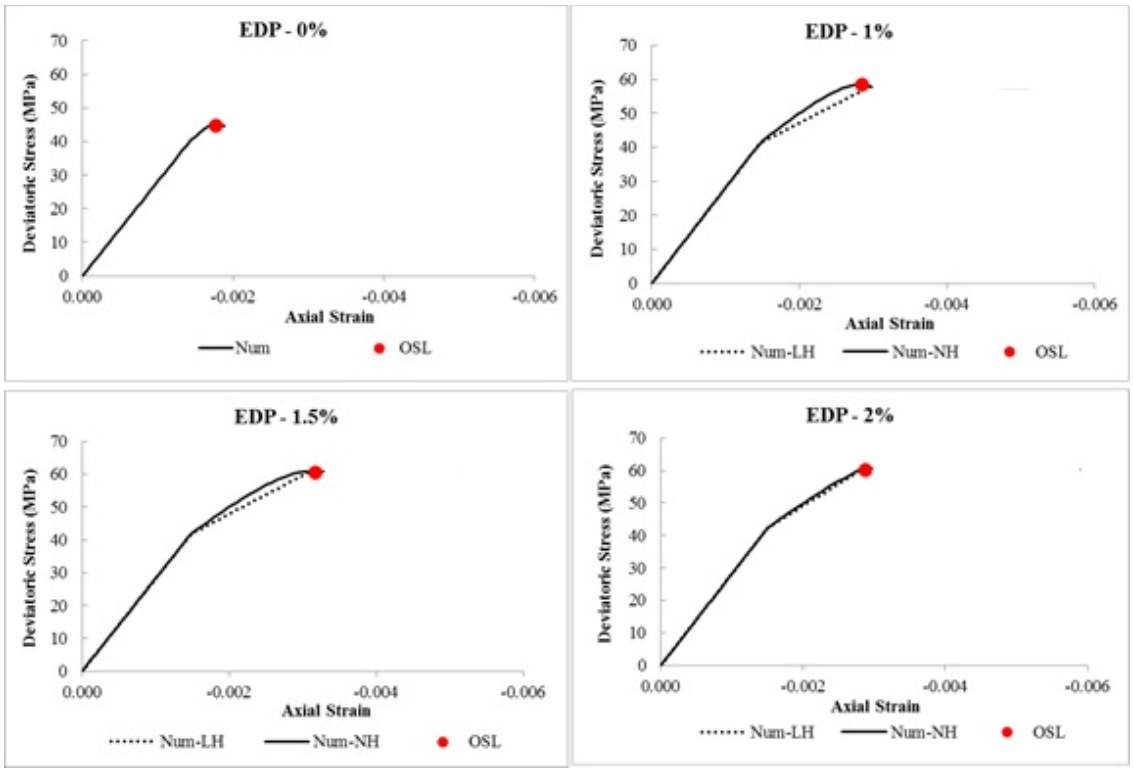

Figure 3.6 Numerically predicted responses for EDP model in UC with linear and nonlinear hardening (HPFRCC with volumetric fiber contents of 0%, 1%, 1.5% and 2%)

The predicted OSL in the plain mortar coincided closely with the peak stress. For HPFRCC, stress-strain response exhibited more pronounced strain hardening prior to the predicted OSL, which closely coincided with the peak stress. Unlike in UT tests the predicted OSL in UC tests coincided with the onset of major crack localization. In addition, results showed a 25% increase in the peak stress in HPFRCC compared to the plain mortar.

3.7. Strain localization predictions

Next, the influence of fibers on the OSL, and direction and mode of deformation bands is investigated.

Figure 3.7 summarizes axial strain values at the OSL for various volumetric fiber contents. The left figure depicts the results from the UC test modeled with LDP and EDP with

nonlinear hardening. The figure on the right shows the data from the UT test modeled with HDP and EDP with nonlinear hardening. Figure 3.7 shows that the presence of fibers delayed the inception of strain localization in all uniaxial tests. For example, in UC tests, the addition of 1.5% of fibers to a matrix doubled the axial strain at OSL. Results from the UC test showed that HPFRCC containing 1.5% of fiber most effectively postponed the inception of strain localization, followed by 1% and 2%, whereby the later are very close to each other. In the UT tests the OSL occurred at nearly equal strain levels for all non-zero volumetric fiber contents, and the presence of fibers in the matrix doubled the axial strain at the OSL with respect to the non-reinforced specimens. These findings were validated by two types of plasticity models for both, UC and UT tests.

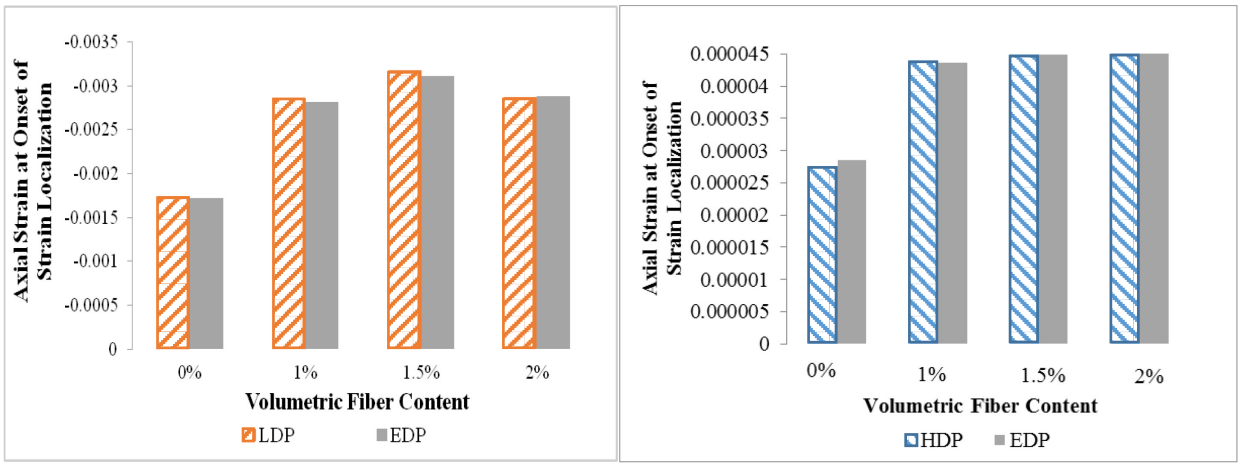

Figure 3.7 Axial strain at the OSL for different volumetric fiber contents for plane stress UC tests (left) and UT tests (right)

The additional goal of this research was to investigate the effect of hardening type on the inception of strain localization. Therefore, two types of hardening were considered: linear and nonlinear hardening rules. Figure 3.8 shows the value of axial strain at the OSL versus volumetric fiber content for these two types of hardening. It is noted that the results for the

unreinforced cementitious composite in UT are not shown in Figure 3.8 because the composite was assumed not to experience any hardening during the UT test. As shown in the figure, the hardening type did not significantly affect the OSL in UC and UT tests.

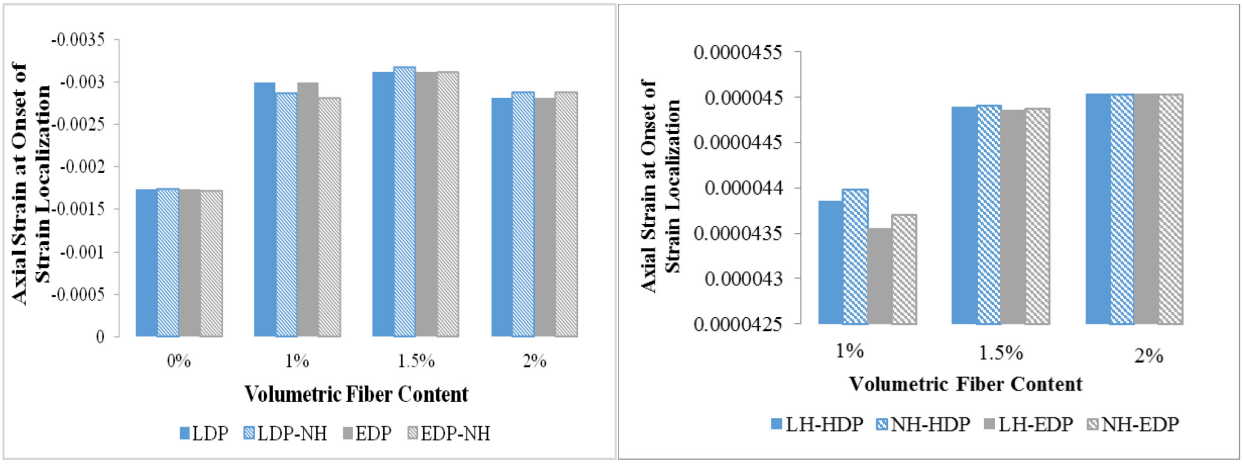

Figure 3.8 Axial strain at the OSL for various volumetric fiber contents and different types of hardening for UC tests (left) and UT tests (right)

Figure 3.9 depicts values of the axial stresses at the OSL versus volumetric fiber content. It can be observed that in both tests, UC and UT, addition of fibers to the plain composite increased the level of axial stress at the OSL. The type of hardening had less influence on the values of axial stress at the OSL in the UC test, than in the UT test.

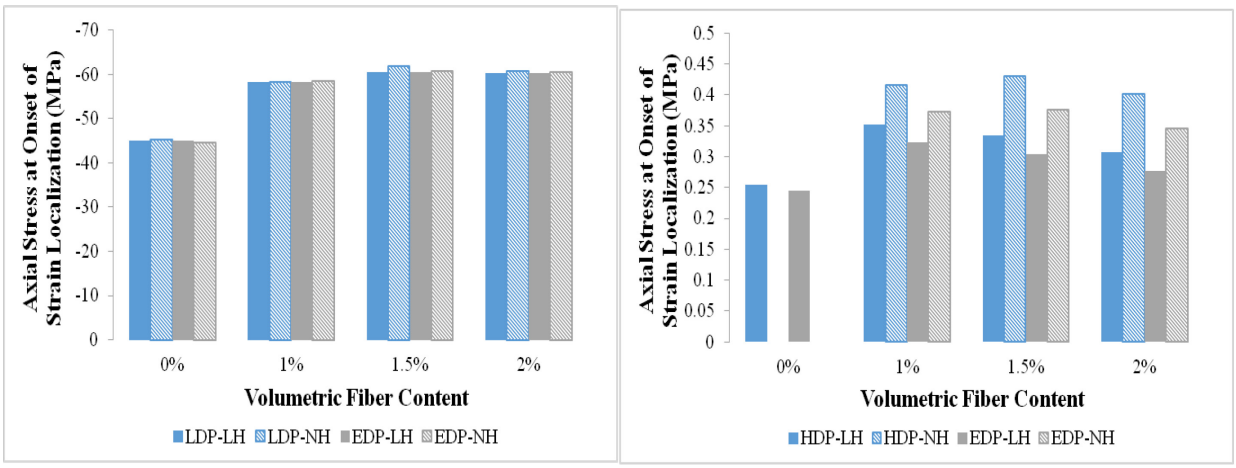

Figure 3.9 Axial stress at the OSL for various volumetric fiber contents and different types of hardening for UC tests (left) and UT tests (right)

Figure 3.10 and Figure 3.11 illustrate how orientation of deformation bands and their modes changed with volumetric fiber content for the UC and UT tests respectively. It is evident from Figure 3.10 (left) that the localization angle decreased with an increase in volumetric fiber content for both plasticity models in the UC tests. Thus, deformation bands in UC tests became flatter with the addition of fibers. The right side of the Figure 3.10 shows increase in the mode angle with increase in fibers, thus implying that deformation bands become more contractant with addition of fiber.

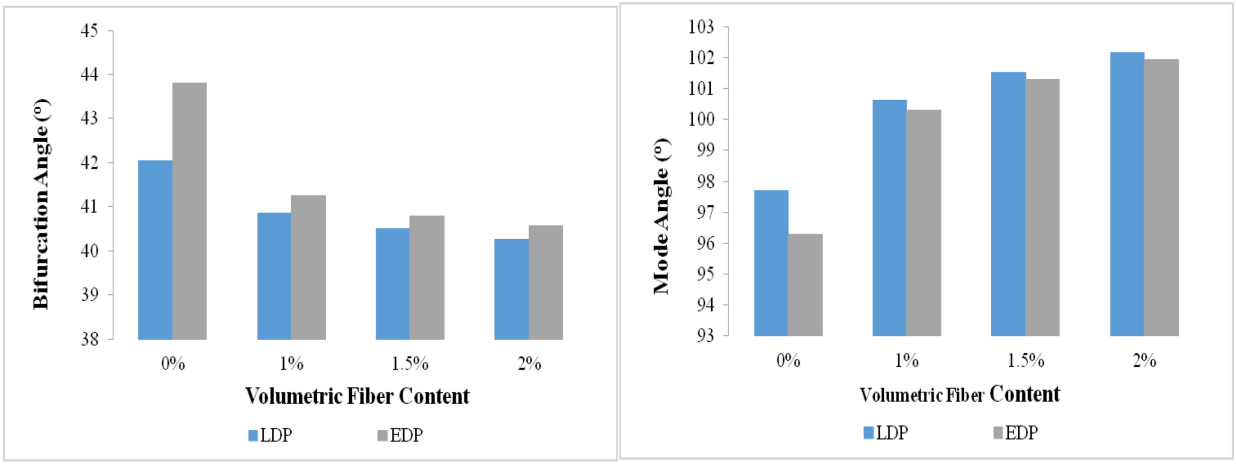

Figure 3.10 Critical bifurcation angle (left) and mode angle (right) versus volumetric fiber content for UC tests

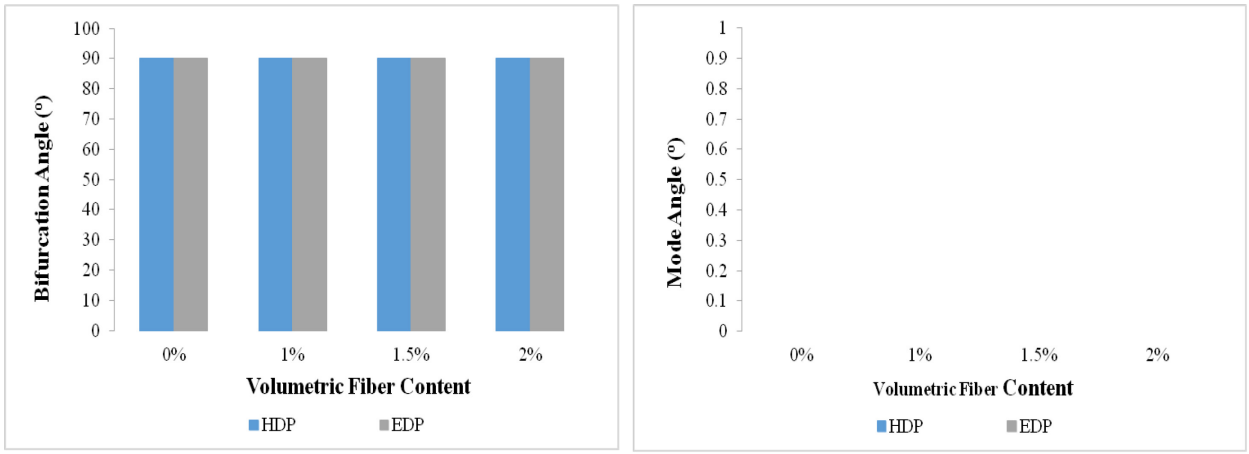

Figure 3.11 Critical bifurcation angle (left) and mode angle (right) versus volumetric fiber content for UT test

Figure 3.11 (left) shows that presence of fibers did not affect the orientation of deformation bands in the UT tests at all. For each case, the orientation was 90^0 implying that deformation bands were perpendicular to the direction of a major principal stress. Furthermore, fibers did not have any effect on the mode angle as well (Figure 3.11-right). Mode angles for all volumetric fiber content remained equal to zero, thus signifying pure dilatation bands.

Chapter 4 - Material characterization of the UHPFRCC

4.1. Materials, mix proportions and fiber properties

As mentioned previously, all experiments conducted during this study were performed on the UHPFRCC at the University of New South Wales, in Sydney, Australia. In the casting process of the UHPFRCC, Type I General Purpose Cement, produced by Cement Australia, was used. The specific gravity of the cement was 3.15. Furthermore, un-densified silica fume supplied by SIMCOA, Western Australia, was used. Sydney sand with a specific gravity of 2.6, a maximum particle size of 600 μm, and a fineness modulus between 1.3–1.6 was used as the fine aggregate. Sand was oven dried at 105ºC for at least 24 hours before being used. The superplasticizer used was Glenium 107 Suretec manufactured by Baden Aniline and Soda Factory (BASF).

Three different types of steel fibers were used in this study. The first type (S) was a straight wire with a length, l_f of 13 mm, and a diameter, d_f of 0.2 mm. The second type of fibers was double end hooked (DEH) cold drawn wire fibers, with the length and diameter of 60 mm and 0.9 mm, respectively. The third type of fibers was a single end hooked (EH) cold drawn wire fibers with a length and diameter of 25 mm and 0.3 mm respectively. All three types of the fibers were manufactured from a very high strength steel wire with minimum tensile strength of 1,800 MPa. In addition, fibers S and DEH were manufactured by Dramix, Belgium, while Dura Technology, Malaysia fabricated EH fibers. Three volumetric fiber contents, χ_f were adopted in this experimental program corresponding to 1 %, 2 %, and 3 %. Dimensions and properties of all types of fibers are given in Table 4.2 and Figure 4.1.

The test variables were water to binder (w/b) ratio, the type of fibers and volumetric fiber content. The total of five different material mix designs were cast and tested in this study. Mixes

were identified using the following abbreviations: the first part represents a number of the mix (M1 for the mix cast first), the second part indicates a percentage of the volumetric fiber content added to the cementitious matrix, and the last part specifies the type of fiber used. It is noted that one of the mixes had a higher water to binder ratio in the comparison with other mixes, thus it has an additional term "2" at the end of the abbreviation. For example, the abbreviation M2-3S denotes the second mix with the three percent of the straight fibers, while M4-2EH/S2 denotes the fourth mix cast with the two percent of end hooked and straight fibers incorporated in the matrix, and has a higher water to binder ratio. Table 4.1 summarizes all of the concrete mix designs.

Table 4.1 Concrete Mix Design (proportion by weight relative to weight of cement)

Component	Mix Design Number				
	M1-2S	**M2-3S**	**M3-1DEH**	**M4-2EH/S2**	**M5-2EH/S**
Cement	1	1	1	1	1
Silica Fume	0.25	0.25	0.25	0.25	0.25
Sydney Sand	1.1	1.1	1.1	1.1	1.1
Superplasticizer	0.026	0.028	0.027	0.017	0.026
Water	0.20	0.19	0.20	0.24	0.20
Steel Fibers (S)	0.17	0.25	-	0.085	0.085
Steel Fibers (DEH)	-	-	0.085	-	-
Steel Fibers (EH)	-	-	-	0.085	0.085
Water/Cement	0.20	0.19	0.20	0.24	0.2
Water/Binder	0.16	0.15	0.16	0.19	0.16
χ_f (%)	2.0	3.0	1.0	2.0	2.0

Table 4.2 Properties of steel fibers

Type	Length, l_f (mm)	Diameter, d_f (mm)	Aspect Ratio, η_f	Tensile Strength (MPa)	Fiber Shape
S	13	0.2	65	1800	
DEH	60	0.9	67	2300	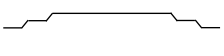
EH	25	0.3	83	>2300	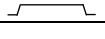

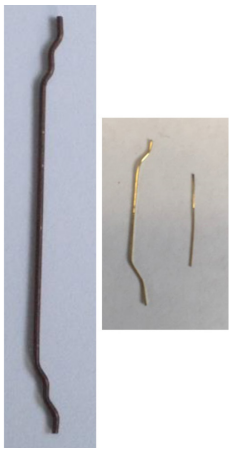

Figure 4.1 Photo of the three fiber types used in study: DEH, EH, and S respectively from the left to the right

A total of three direct tension, three un-notched prism specimens, and nine cylinders were cast for each mix design. All mixing quantities were batched using an electronic balance and mixed in a horizontal pan type mixer. In the mixing process, all dry components (cement, sand, and silica fume) were first mixed together for a few minutes and then the water and superplasticizer were added. Once the dry components were fully mixed with the liquid part fibers were slowly added in a small amount at a time. They were sprinkled manually into the mix through the Sieve No. 4 and the mixing was continued for another few minutes.

Once the right plastic consistency of the mix was achieved, the specimens were cast in lubricated stainless steel molds in two layers. They were subsequently vibrated using a shaking table in order to achieve a good compaction. The internal vibration should be avoided in the case of the FRCC in order to ensure the uniform distribution of the fibers within the sample. After casting, the specimens were kept in their molds and covered with a wet hessian to prevent moisture loss for about 24 hours. The specimens were then demolded and placed in a hot water tank at the temperature of 80ºC for seven days. In addition, in order to ensure an even loading during the uniaxial compression test, both ends of the cylinders were ground flat and smooth.

4.2. Compression strength and Young's modulus tests

A compressive strength is an important property in the design of any concrete structure. The uniaxial or unconfined compression test also known as a cylinder compression test is the appropriate test for determination of a compressive strength of a cementitious composite regardless of the amount of fibers that it may contain. Therefore, cylinder specimens having a 100 mm diameter and a 200 mm height were tested, thus enabling determination of the compressive strength for all five concrete mix designs. For determination of a compressive strength, the load control rate was 20 MPa per minute, as per Australian Standard AS1012.9 [113]. The compressive strength, f_{cm} of the specimen was computed by dividing the maximum load attained during the test by the average cross-sectional area of the specimen.

Furthermore, in order to obtain a Young's modulus, *E,* of a sample from an unconfined uniaxial compressive test, the applied load, and a longitudinal deformation were recorded. A longitudinal deformation was measured using a linear variable differential transformer (LVDT), which was attached to the side of a specimen. It is noted that it is necessary to obtain the compressive strength on companion specimens prior to testing for Young's modulus because the maximum load applied during the latter test was equal to 40% of the uniaxial compressive strength. Young's modulus was extracted from the slope of the straight line passing through the origin and the 40% compressive stress point and corresponding strain, which is in agreement with Australian Standard AS1012.17 [114].

In order to ensure the consistency of the results, at least three specimens within the same series were tested and their mean value was used. The final results are shown in Table 4.3. Raw data are included in the Appendix A1.

Table 4.3 Compressive strength and elastic modulus of UHPFRCC mixes

Mix No.	w/b	χ_f (%)	f_{cm} (MPa)	E (GPa)
M1-2S	0.16	2	169	43.6
M2-3S	0.15	3	177	45.6
M3-1DEH	0.16	1	143	43.9
M4-2EH/S2	0.19	2	155	42.1
M5-2EH/S	0.16	2	169	42.7

It can be seen from Table 4.3 that compressive strength varied between 143 and 177 MPa. Moreover, the material mix design with the lowest w/b (M2-3S) had the highest unconfined compressive strength. It is because a lower w/b reduces voids between particles and thus contributes to an increase in the packing density, which has a positive effect on reduced porosity in cement matrix and subsequently on its compressive strength [115].

Furthermore, although there is a common understanding that the addition of fibers to a cementitious matrix causes a significant increase in the tensile strength of FRCC there is a slight dissent within the research community as to whether fibers also increase the compressive strength. Experimental data showed that compressive strength is practically not increased due to addition of fibers [116], while the other data including ([117], [118], [119]) indicate that both, the type and volumetric content of fibers affect a compressive strength of UHPFRCC. Results obtained in this study (Table 4.3) indicate that the volumetric fiber content affects uniaxial compressive strength of UHPFRCC. Specifically, the increase in χ_f increases the uniaxial compressive strength. For example, UHPFRCC with the lowest amount of fibers (χ_f =1%) had the lowest compressive strength (f_{cm}=143 MPa), while the mix with the highest amount of fibers (χ_f =3%) had a compressive strength of 177 MPa (f_{cm}=177 MPa).

In addition, it can be seen from Table 4.3 that the value of Young's modulus of UHPFRCC was not significantly affected by the volumetric fiber content. Specifically, it varied

between 42 and 46 GPa. A number of equations, which define correlations between the Young's modulus and unconfined compressive strength can be found in the literature. For example ACI 363R-92 [120], Kakizaki et al. [121], and Sritharan et al. [122] developed Eqs 4.1 through 4.3 for HPFRCC. On the other hand, Graybeal [123] and Ma et al. [124] developed Eqs.4.4 and 4.5 for UHPFRCC:

$$E(MPa) = 3,300\sqrt{f_{cm}(MPa)} + 6.9 \quad \textbf{4.1}$$

$$E(MPa) = 3,650\sqrt{f_{cm}(MPa)} \quad \textbf{4.2}$$

$$E(MPa) = 4,150\sqrt{f_{cm}(MPa)} \quad \textbf{4.3}$$

$$E(MPa) = 3,840\sqrt{f_{cm}(MPa)} \quad \textbf{4.4}$$

$$E(MPa) = 16,364\ln(f_{cm}(MPa)) - 34,828 \quad \textbf{4.5}$$

Most of these equations have a very similar form. Figure 4.2 depicts the experimentally obtained data presented in Table 4.3 along with Eqs. 4.1 through 4.5. It appears from Figure 4.2, that Eq. 4.1 provides the best fit to the experimental data generated in this study. It is noted that Eq. 4.1 was originally developed for the HPFRCC. Among the Eqs.4.4 and 4.5 which were developed specifically for the UHPFRCC, both of them give similar results.

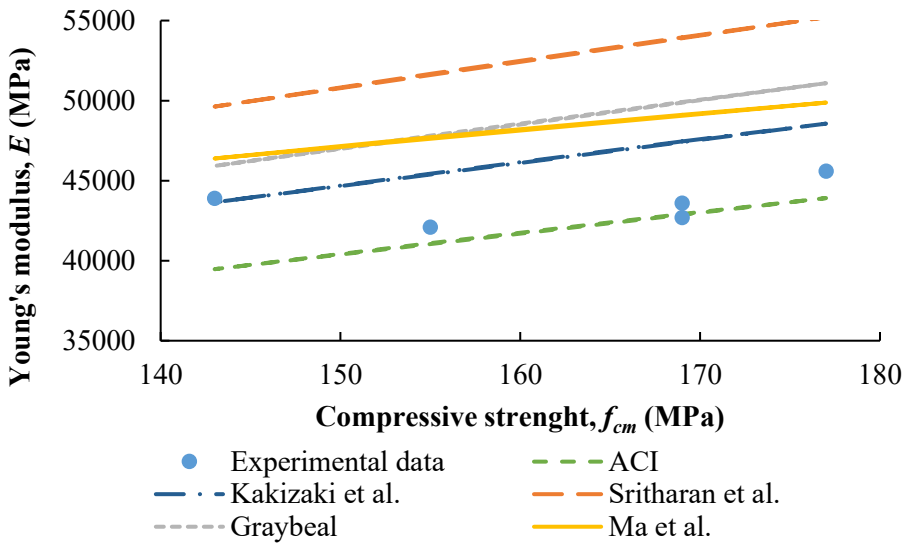

Figure 4.2 Comparison of experimental data and equations proposed for Young's modulus of UHPFRCC

Due to a high compressive strength of the ultra-high performance cementitious composites an unconfined compression results in an extremely brittle failure [125]. On the other hand, in the case of UHPFRCC a compressive failure tends to be similar to the compressive failure of any fiber-reinforced concrete, which exhibits a more ductile behavior due to a restraining and confining effect of fibers. Figure 4.3 shows a comparison of compressive failures of the ultra-high performance concrete with and without fiber reinforcement. Furthermore, Figure 4.3 a) shows that the compressive failure of UHPC started by spalling at the top and bottom edges of the cylinder at its contact with the steel plates. It continued until the UHPC specimen crushed and disintegrated into many fragments [125].

Nevertheless, the compressive failure of the UHPFRCC tested in this study (mix M1-2S) depicted in Figure 4.3 b) is strikingly different from the failure of UHPC shown in Figure 4.3 a). Specifically, the presence of fibers nearly completely stops disintegration of the specimen. Moreover, a compressive load is accommodated by lateral expansion, which is partially

restrained by the steel fiber reinforcement, thus ultimately resulting in a more ductile failure mechanism.

a) b)

Figure 4.3 Comparison between the compressive failure of a) a UHPC specimen without fiber reinforcement (adapted from [125]), and b) a UHPFRCC specimen (this study)

4.3. Tension testing

The following section will focus on the experimental determination and evaluation of the tensile properties of the UHPFRCC. In the case of a conventional plain concrete, a splitting test method is commonly used test for determination of a splitting tensile strength of cylindrical concrete specimens [8]. However, in the case of more ductile material, such as UHPFRCC, use of such indirect testing method can be more challenging when determining the post response. Therefore, in order to examine the tensile properties of UHPFRCC two different types of tension tests were conducted: 1) direct tension test, and 2) four-point prism bending test. They are described next.

4.3.1. Direct tension test

Specimen development and testing procedure

One of the tests, which was conducted herein in order to determine tensile properties of the UHPFRCC was a direct tension test. It is one of the most challenging experimental methods for several reasons. A direct tension test requires a sophisticated testing machine, which should be capable of loading a sample under external displacement control. Moreover, a great care must be taken in ensuring that a high-strength gripping holds a tensile specimen. Lastly, a shape and geometry of a specimen must be specially designed so that it can provide a uniaxial tensile stress state throughout the specimen. A direct tension test will be capable of providing the most complete set of results only if all of these requirements are met. Furthermore, it provides one of the most direct ways of obtaining a complete response including a tensile stress-strain and stress-crack opening behavior.

Many researchers have investigated direct tensile test. They attempted to develop reliable and repeatable means of testing the tensile properties of FRCC. Although, Japan Society of Civil Engineers [11] and French Association of Civil Engineering [12] both provide recommendations on how to conduct direct tensile tests on HPFRCC and UHPFRCC materials, there are currently no testing standards available that define the test conditions, specimen geometry, and analytical procedures necessary to fully characterize tensile properties of strain-hardening cementitious materials.

When designing a reliable tensile test setup for determining the tensile characteristics of FRCC, three fundamental technical issues should be considered. They include the geometry and alignment of a specimen, and corresponding boundary conditions. One of the main aims of this

research was to develop the specimen geometry and loading arrangement that would ensure a uniform tensile stress field over a large area that is unaffected by the loading arrangements.

The geometry of a sample includes a shape, dimensions of the specimen as well as a decision whether to test a notched or un-notched sample. The most common specimen shapes used in direct tension test are prism, cylinder, and a so-called dog-bone, both notched and un-notched. A common drawback for un-notched prisms and cylinders is occurrence of a stress concentration in the specimen near boundaries where a cementitious composite specimen is attached to steel loading platens. Stress concentrations occur at this location due to a discrepancy in the values of Young's moduli and Poisson's ratios of a cementitious composite and steel. The stress concentrations often lead to a glue failure, also known as a "bond failure" [91]. It is common practice to use notched specimens to avoid these bond failure occurrences. However, in the case of notched specimens, stress concentrations occur in the vicinity of the notch due to a sudden change in the area of a cross section, which causes subsequent micro-cracks to form exclusively in this area. It is because capturing of a multi-cracking behavior is one of important goals of this study, the decision was made to proceed with testing un-notched specimens.

As pointed out previously, stress concentrations and bond failure near the steel loading platens can be avoided by reducing dimensions of the middle portion of the specimen. This is the reason why a so-called dog-bone shape of a specimen is one of the most frequently used specimen shapes for direct tensile testing. This shape of the specimen geometry was originally introduced by van Vliet [91], who studied tensile properties of a conventional concrete and rock. Moreover, a wide range of different dog-bone shaped specimens have already been successfully used in the past for FRCC [33].

In general, an un-notched dog-bone specimen has three main sections: middle section with the reduced cross sectional area, grip sections and smooth transition sections in between the former two sections. The un-notched middle section has constant or nearly constant cross-sectional area in order to enable and capture a multiple cracking behavior. While choosing the shape and dimensions of the middle section, recommendations made by Naaman and Reinhardt [36] were followed. They suggested using prisms of square or circular cross-section, with a side or diameter equal to at least to 50 mm, and minimum three times the fiber length, and/or six times the size of the maximum aggregate. In the research presented here, the largest fiber length of 25 mm was used, thus giving a square cross-section with the side length of 75 mm. It was decided at the later stage of testing to use fibers longer than 25 mm, only in one instance (M3-1DEH). Naaman and Reinhardt [36] also suggested that the gauge length for measuring the axial strain should be at least two to three times the minimum size (side or diameter) of a tensile prism. It is important to note, that it may not be possible to control the test if the gauge length is too small and a crack occurs outside of the gauge length. On the other hand, if the gauge length is too large, the snap back behavior can occur if the stored elastic energy is released from the material outside of the fracture process zone. Therefore, the selected lengths of the middle section and gauge length were 300 and 480 mm, respectively.

The transition section is smooth, thus providing a continuous transition from the grip sections to the middle one, which reduces and minimizes the effects of stress concentrations and ensures a uniform stress field in the middle section. The length of the transition zone is crucial in order to guarantee the constant stress region. Therefore, in the design process of a transition zone, Neuber's solution [126] for the length and shape of transition section was implemented. Neuber's solution ensures no stress concentration along the continuous transition curve. For

more detailed calculations reader is referred to Neuber [126]. A similar approach for the design of the transition section was proposed by Benson and Karihaloo [127] and used to measure a uniaxial tensile response of CARDIFRC mixes, a class of high performance short steel FRCC.

The grip section of the specimen has a larger cross sectional area in order to reduce boundary stresses, avoid support failure and to ensure that a uniform tensile stress field over a middle section remains unaffected by the loading arrangement. Two different widths of grip section widths were considered, 130 mm and 150 mm. Upon completion of the related computational modeling the grip section with of 150 mm was selected for dog bone specimens. The computational modeling is discussed in the test below.

Other highly important considerations, which need to be taken into account while designing a uniaxial tensile test setup, include the alignment of the specimen, and boundary conditions. Both of these continue to be a subject of an ongoing discussion in the scientific community. A load can be transferred to the specimen by gluing, anchoring or clamping it to the machine. All of these methods have been found applicable ([33], [92]) for dog-bone shaped specimens. While designing tensile setup in this study, several different gripping arrangements and boundary conditions of a dog-bone specimen have been analyzed, such as glued, anchored, and embedded rods, as well as a combination of former three. After the completion of the numerical simulations it was decided to embed the rods 100 mm into the specimen.

Furthermore, there is significant discussion in the literature on whether the ends of uniaxial tension specimens should be either fixed, pinned or a combination of both ([93], [87]). Fixed ends at each end of a specimen would prevent the rotation of the test specimen while rotating ends would allow the specimen end to freely rotate about the center point. All of the above variations have been used in a direct tension test. In the ideal case the specimen should be

fixed at each end. The initial crack occurs at the weakest location within the specimen. However, when fixed loading platens are used, the platens are forced to remain parallel during the crack propagation, thus inducing a bending moment into the sample. Thus, the crack will be prevented from propagating further until the other side of the specimen begins to fracture. This ultimately leads to a higher fracture toughness than can be achieved with free rotating boundary conditions ([89], [67]). To avoid this, Draft Australian Bridge Code: Concrete [94] adopted one fixed end and the other end fitted with a universal joint to eliminate any residual tension that may develop during the gripping process. The same testing arrangement, with one rotating and one fixed end in uniaxial tension, was adopted in this study.

In order to finalize the test setup, and to find most optimal specimen shape, a linear elastic analysis was performed using the commercial finite element (FE) analysis software ABAQUS [108]. The results provided distributions of stress tensor components within the specimen. To this end, several different geometries and boundary conditions of a dog-bone specimen have been analyzed. The general shape of a specimen was always the same while different values of a total height of the specimen $(\bar{H})$, a width of the gripping section (W) and a radius (R) of the transition spline were considered. Furthermore, several different boundary conditions (BC), such as glued, anchored, embedded rods, and the combination of former three, were simulated as well in order to evaluate the influence of BCs on the stress and strain distributions. A schematic diagram of the computational modeling process can be found in Figure 4.4.

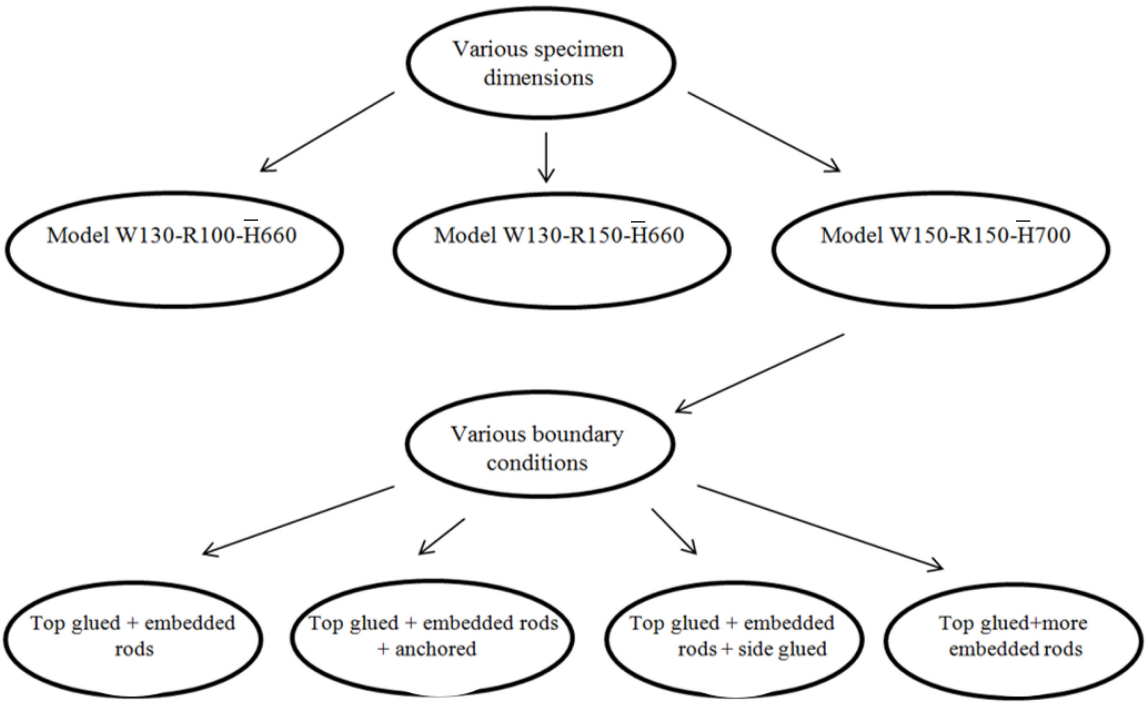

Figure 4.4 Schematic diagram of the computational modeling process

An eight node isoparametic linear brick element (C3D8R:3D) with reduced integration was used to represent steel fiber reinforced cementitious composites, while a two node linear three dimensional truss element (T3D2) was used to model steel gripping rods. The Young's moduli of 30 and 210 GPa were used for steel FRCC and steel, respectively. Poisson's ratios of the steel FRCC and steel rods were equal to 0.2 and 0.3, respectively. Rods were embedded into a solid block.

Figure 4.5 depicts a contour plot of the linear elastic vertical stress distribution under the external uniaxial tensile load. It can be seen from the figure that a uniform tensile stress field was ensured in the middle section of the specimen and that it was not affected by the loading arrangement. Moreover, results show that the stress is the greatest in the middle section of the specimen, causing that cracking occurs in that area. It should be noted, that in this FE

simulations specimens are made out of the perfectly homogenized material, which is not true it the real case scenario.

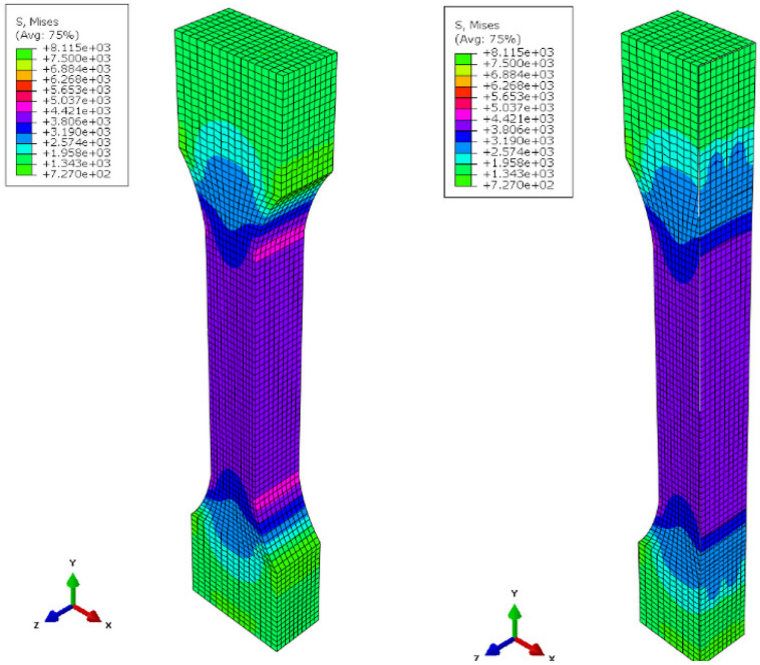

Figure 4.5 Vertical stress distributions for the whole specimen (left) and with the view cut through the rods (right) (Units Pa)

After taking into account all relevant recommendations from the literature, prerequisites, and results of the FE analyses an elongated dog-bone specimen was selected for testing. Its overall length was equal to 700 mm, out of which a transition spline was 450 mm long, and a prismatic mid-section was 75 mm wide. The width of the prismatic mid-section increased gradually to 150 mm at the end of the transition spline (Figure 4.6).

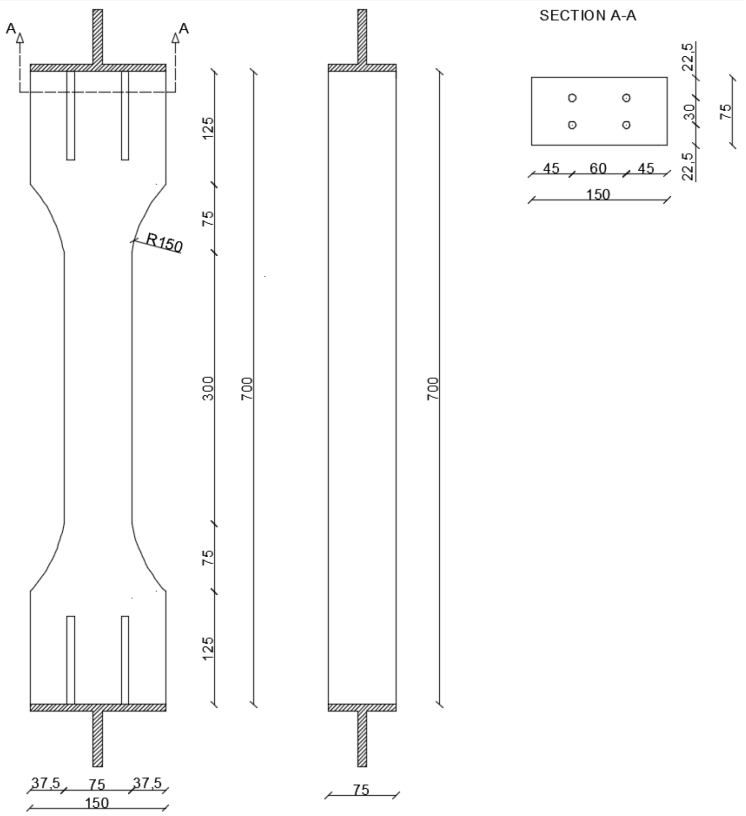

Figure 4.6 Model W150-R150-H700 specimen geometry (dimensions in mm)

Prior to casting, four 16 mm 8.8 grade threaded rods were placed 100 mm within each end of the formwork (Figure 4.7). A level and alignment of the threaded rods were checked from the inside of the form and then locked in place using a nut on either side of the wall of the formwork.

The specimens were cast horizontally in lubricated stainless steel molds using the procedure outlined in the earlier section. Also, the center portion of the mold was filled to approximately 90% of the height of the specimen, which was then followed by pouring of the ends. The material in dog-bone molds was externally vibrated using a shaking table.

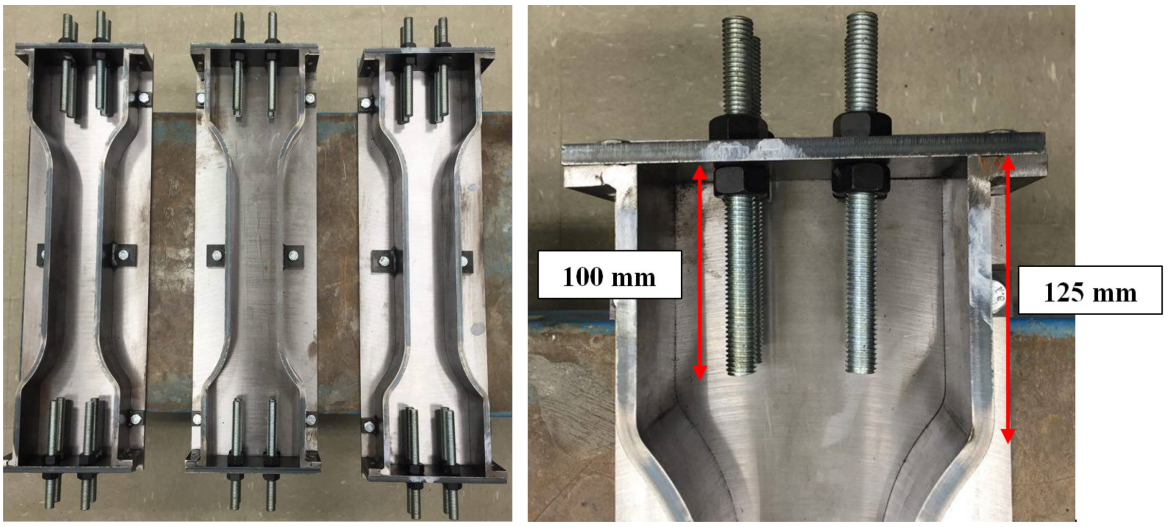

Figure 4.7 Photos of the dog-bone molds and a detail of the gripping arrangement

Furthermore, direct tension tests on these specially developed dog-bone specimens were performed in a 1MN Instron servo-hydraulic universal testing machine. As mentioned earlier, the dog-bone specimen was connected to the testing machine with four bolted threaded rods protruding from each end of the specimen. One end of the specimen was fixed while the other was fitted with a universal joint. In order to measure displacement, four displacement transducers (LVDTs or LSCTs) were attached along the North, South, East and West sides of the specimen in the loading direction. The gauges were mounted and centered on the specimen sides and had gauge lengths of 480 mm. A complete test setup is shown in Figure 4.8.

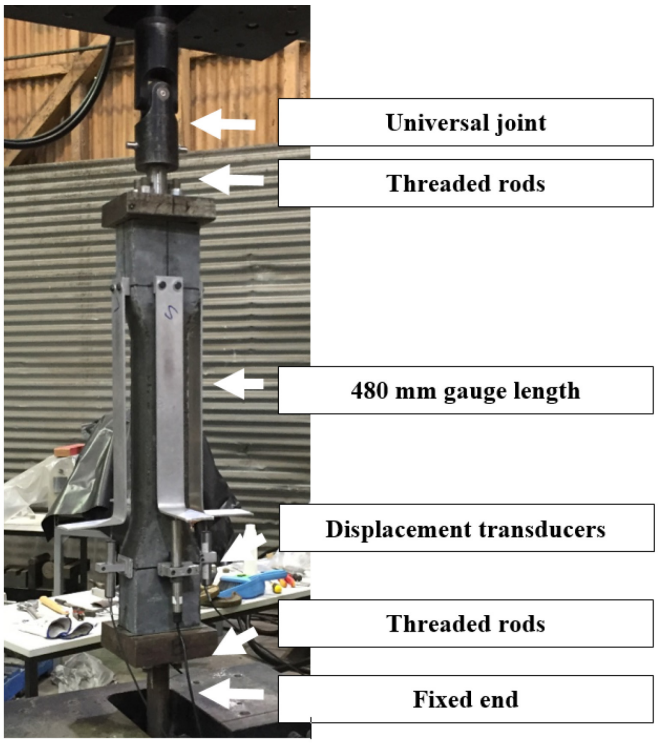

Figure 4.8 Direct tension test setup

Prior to testing, the dog-bone specimens were lightly sprayed with water for the easier crack detection. The uniaxial tensile load was applied using a displacement control with the initial rate of 0.12 mm/min up to the inception of the first crack. After cracking, the displacement rate was gradually increased to 0.2, 0.5, 0.75, 1, 1.5, 2, 3, and 5 mm/min until the crack opened up to 1.5, 2, 2.5, 3, 4, 6, 9 mm, and until the end of the test, respectively. A data acquisition system was used to record the applied load. A deformation of a specimen was obtained by averaging the readings of the four transducers placed on each side of the specimen as indicated in the Figure 4.8. Three tests were repeated for each material mix.

Test results

The test setup and procedures discussed earlier were implemented in order to completely capture the tensile behavior of UHPFRCC. Test results and observations from uniaxial direct tension tests are presented in this section.

In general, a tensile behavior of a FRCC subjected to a direct uniaxial load can be presented in the form of a tensile axial stress-strain response prior to matrix cracking. Upon a major crack localization, a softening behavior initiates and a tensile response can be expressed in terms of a stress versus crack opening displacement. The experimental stress-strain responses obtained from direct tension tests are depicted in Figure 4.9 through Figure 4.13 a), while the post-crack tensile behavior is presented in Figure 4.9 through Figure 4.13 b). An axial stress was calculated by dividing the applied load by the cross sectional area of the narrowest cross-section of a specimen. A deformation of a specimen was obtained by averaging the readings of the four transducers. Moreover, abbreviations DB1, DB2, and DB3 in the figure legends denote the number of dog-bone specimen tested.

Overall, it can be seen from Figure 4.9 through Figure 4.13 a) that the UHPFRCC dog-bone specimens initially exhibited a linear behavior up to onset of a tensile cracking. Thus, the assumption was made that a deformation was distributed uniformly over the entire gauge length. Furthermore, the Hooke's law was used to calculate a tensile modulus of elasticity, E_t. The values of the E_t are summarized in Table 4.4 through Table 4.9. They range between 37.6 and 55.1 GPa depending on the volumetric fiber content and fiber type except for the mix M2-3S. These E_t values are somewhat higher or lower, depending on the mix, than the values obtained from the uniaxial compression tests on cylinders. For mixes M1-2S and M4-2EH/S2, the values of the Young's moduli obtained from uniaxial tension tests correspond relatively well to the

values obtained from the uniaxial compression tests. Moreover, the initial linear elastic behavior is delimited with the first cracking stress (yield stress), $\sigma_{t,f}$. Table 4.4 though Table 4.9 provide all yield stress values along with the corresponding yield strain, $\varepsilon_{t,f}$ and the first cracking load values, F_f. Although only a limited number of experiments were performed the results indicate that the tensile stress at onset of cracking ranges from 4.68-8.52 MPa. This observation excludes the M2-3S data. It was observed during the testing that mixes M4-2EH/S2 (DB1 and DB2), and M5-2EH/S (DB2) exhibited a multiple cracking after yielding. This multiple cracking phase was followed by a major macro-crack localization.

Figure 4.9 through Figure 4.13 b) present the UHPFRCC behavior after a peak stress is reached. Graphs depict a tensile axial stress versus crack opening displacement for each individual mix. Figure 4.14 summarizes responses of all mixes for easier comparisons. The square symbols plotted on the vertical axis denote a maximum tensile stress $\sigma_{t,p}$, with the averages for each mix given in Table 4.9. Moreover, a peak load, F_p, corresponding elongation, d_p and strain, $\varepsilon_{t,p,}$ for each dog-bone specimen are listed in Table 4.4 through Table 4.8. In the majority of the cases, the first cracking stress in dog-bone samples corresponded to the peak stress (M1-2S, M2-3S DB1, M3-1DEH, M5-2EH/S DB1). In all of the direct tension tests, where the first cracking stress in dog-bone samples corresponded to the peak stress, the UHPFRCC dog-bone specimens exhibited a strong acoustic indication of the abrupt formation of the first major crack. This sudden formation of a major crack corresponds to a discontinuity in the axial stress-crack opening displacement response (Figure 4.14 a), c) and e)). A further uninhibited crack propagation was subsequently impeded by engagement of the bridging fibers. Moreover, the in-plane and out-of-plane rotations of the uniaxial specimens at an average crack opening displacement equal to 1.5 mm in Table A.11. (Appendix A.2.)

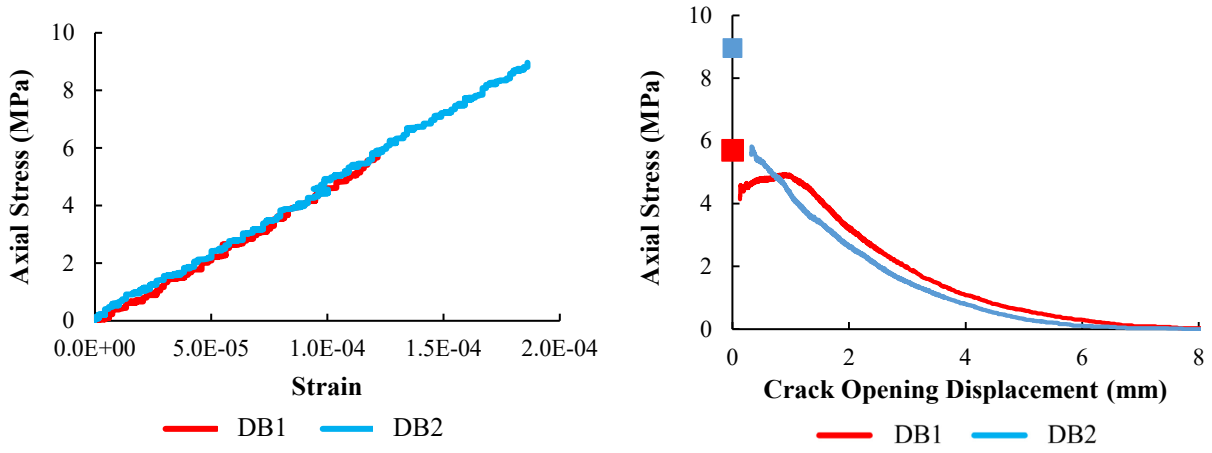

a) b)

Figure 4.9 Direct uniaxial tension test results for M1-2S

Table 4.4 Direct uniaxial tension test results for M1-2S

Specimen	$\sigma_{t,f}$ (MPa)	F_f (kN)	$\varepsilon_{t,f}$ (x10^{-4})	E_t (GPa)
DB1	5.7	33.5	1.23	44.9
DB2	9.0	54.4	1.86	47.7
Mean	7.3	43.9	1.55	46.3

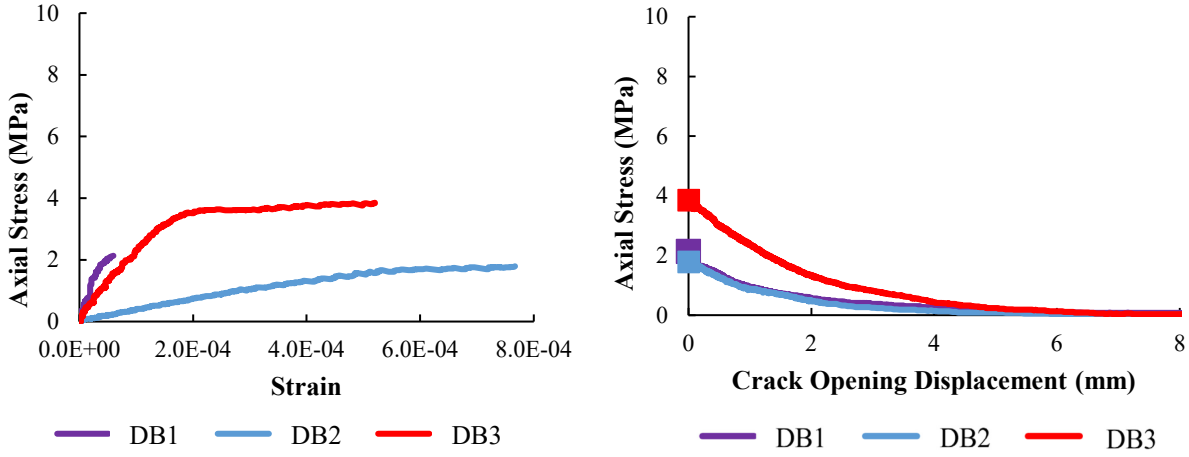

a) b)

Figure 4.10 Direct uniaxial tension test results for M2-3S

Table 4.5 Direct uniaxial tension test results for M2-3S

Specimen	$\sigma_{t,f}$ (MPa)	F_f (kN)	$\varepsilon_{t,f}$ (x10^{-4})	$\sigma_{t,p}$ (MPa)	F_p (kN)	d_p (mm)	$\varepsilon_{t,p}$ (x10^{-4})	E_t (GPa)
DB1	2.13	12.0	0.68	2.13	12.0	0.03	0.68	46.9
DB2	1.67	9.4	5.80	1.79	10.1	0.37	7.74	3.0
DB3	3.40	17.7	1.78	3.85	21.7	0.25	5.22	12.0
Mean	**2.40**	**13.0**	**2.75**	**2.59**	**14.6**	**0.22**	**4.55**	**20.6**

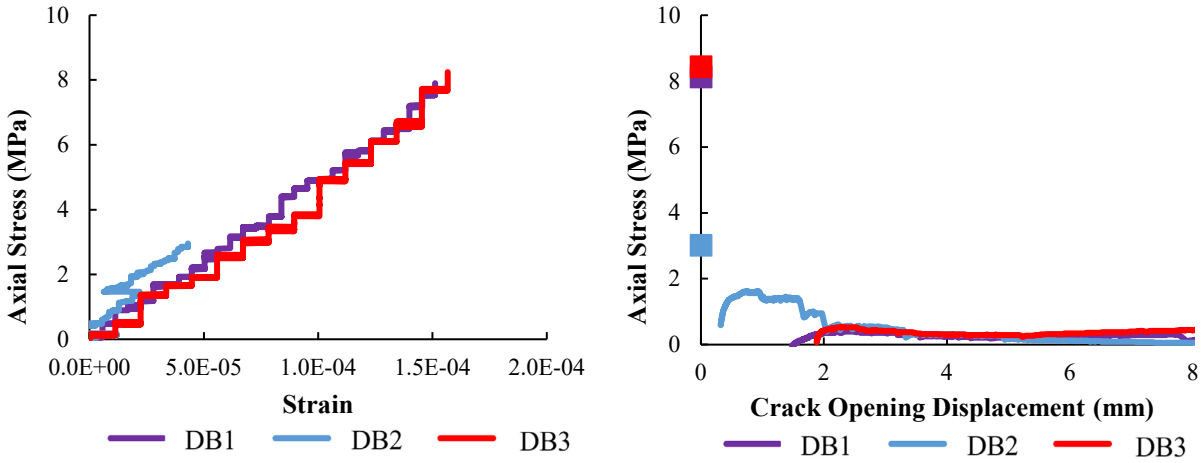

Figure 4.11 Direct uniaxial tension test results for M3-1DEH

Table 4.6 Direct uniaxial tension test results for M3-1DEH

Specimen	$\sigma_{t,f}$ (MPa)	F_f (kN)	$\varepsilon_{t,f}$ (x10^{-4})	E_t (GPa)
DB1	8.14	45.8	0.00	49.2
DB2	3.03	17.0	0.45	69.7
DB3	8.44	47.5	1.68	46.4
Mean	**6.53**	**36.8**	**1.23**	**55.1**

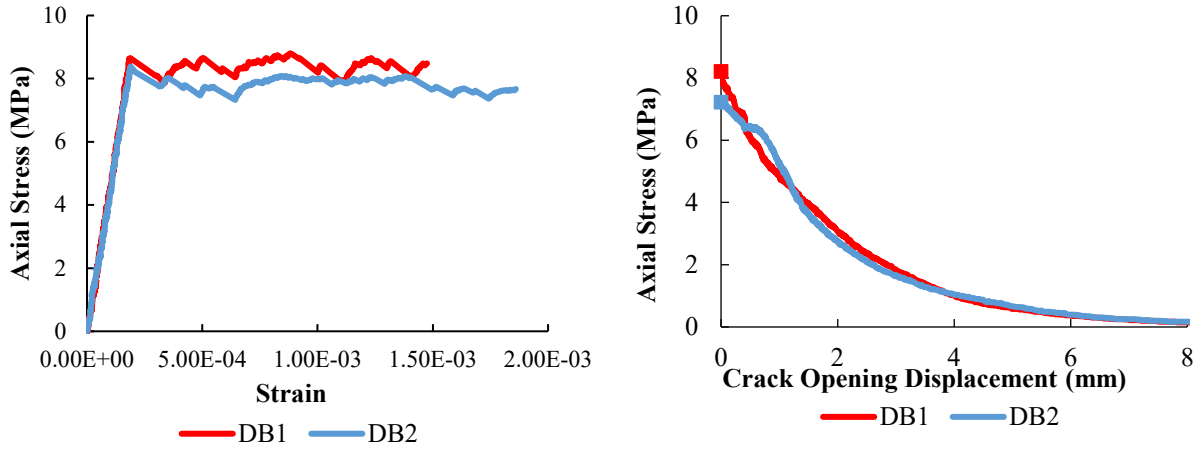

Figure 4.12 Direct uniaxial tension test results for M4-2EH/S2

Table 4.7 Direct uniaxial tension test results for M4-2EH/S2

Specimen	$\sigma_{t,f}$ (MPa)	F_f (kN)	$\varepsilon_{t,f}$ (x10^{-4})	$\sigma_{t,p}$ (MPa)	F_p (kN)	d_p (mm)	$\varepsilon_{t,p}$ (x10^{-4})	E_t (GPa)
DB1	8.66	48.7	1.88	8.80	49.5	0.42	14.7	45.7
DB2	8.39	47.2	1.89	7.67**	43.14	0.54	18.9	44.3
Mean	**8.52**	**47.9**	**1.89**	**8.59**	**48.3**	**0.26**	**18.9**	**45.0**

** Stress corresponding to the end of multiple cracking stage (Lower than the first cracking stress)

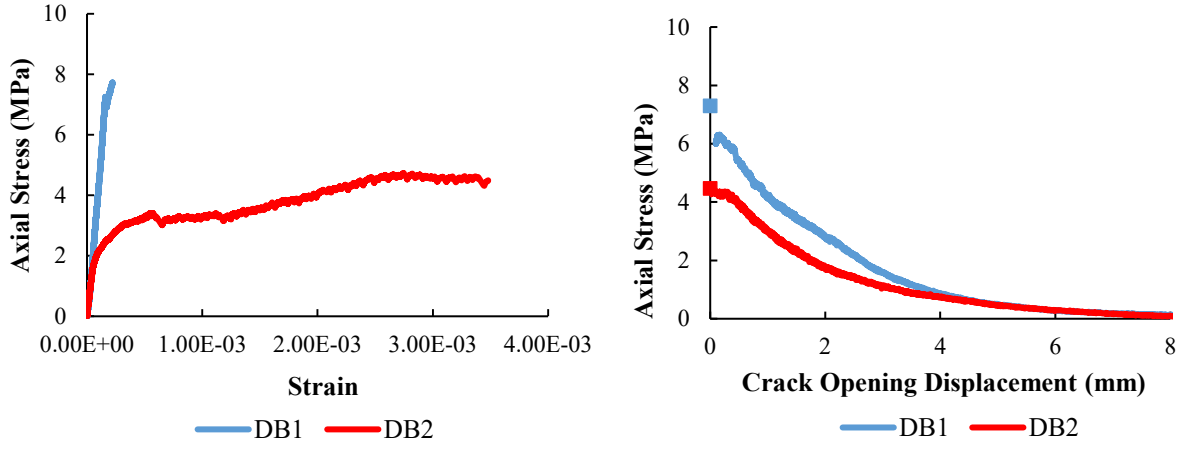

Figure 4.13 Direct uniaxial tension test results for M5-2EH/S

Table 4.8 Direct uniaxial tension test results for M5-2EH/S

Specimen	$\sigma_{t,f}$ (MPa)	F_f (kN)	$\varepsilon_{t,f}$ (x10^{-4})	$\sigma_{t,p}$ (MPa)	F_p (kN)	d_p (mm)	$\varepsilon_{t,p}$ (x10^{-4})	E_t (GPa)
DB1	7.69	43.56	2.22	7.69	43.6	0.11	2.2	42.2
DB2	1.66	9.4	0.38	4.71	26.6	1.32	N/A	33.0
Mean	**4.68**	**26.5**	**1.30**	**6.20**	**35.1**	**0.71**	**2.2**	**37.6**

Table 4.9 Summary of direct tension test results

Mix	χ_f (%)	E_t (GPa)	$\sigma_{t,f}$ (MPa)	$\varepsilon_{t,f}$ (x10^{-4})	$\sigma_{t,p}$ (MPa)	d_p (mm)
M1-2S	2.0	46.3	7.3	1.55	7.3	0.074
M2-3S	3.0	20.6	2.59	4.55	2.59	0.22
M3-1DEH	1.0	55.1	6.53	1.23	6.53	0.06
M4-2EH/S2	2.0	45.0	8.52	1.90	8.59	0.26
M5-2EH/S	2.0	37.6	4.68	1.30	6.2	0.71

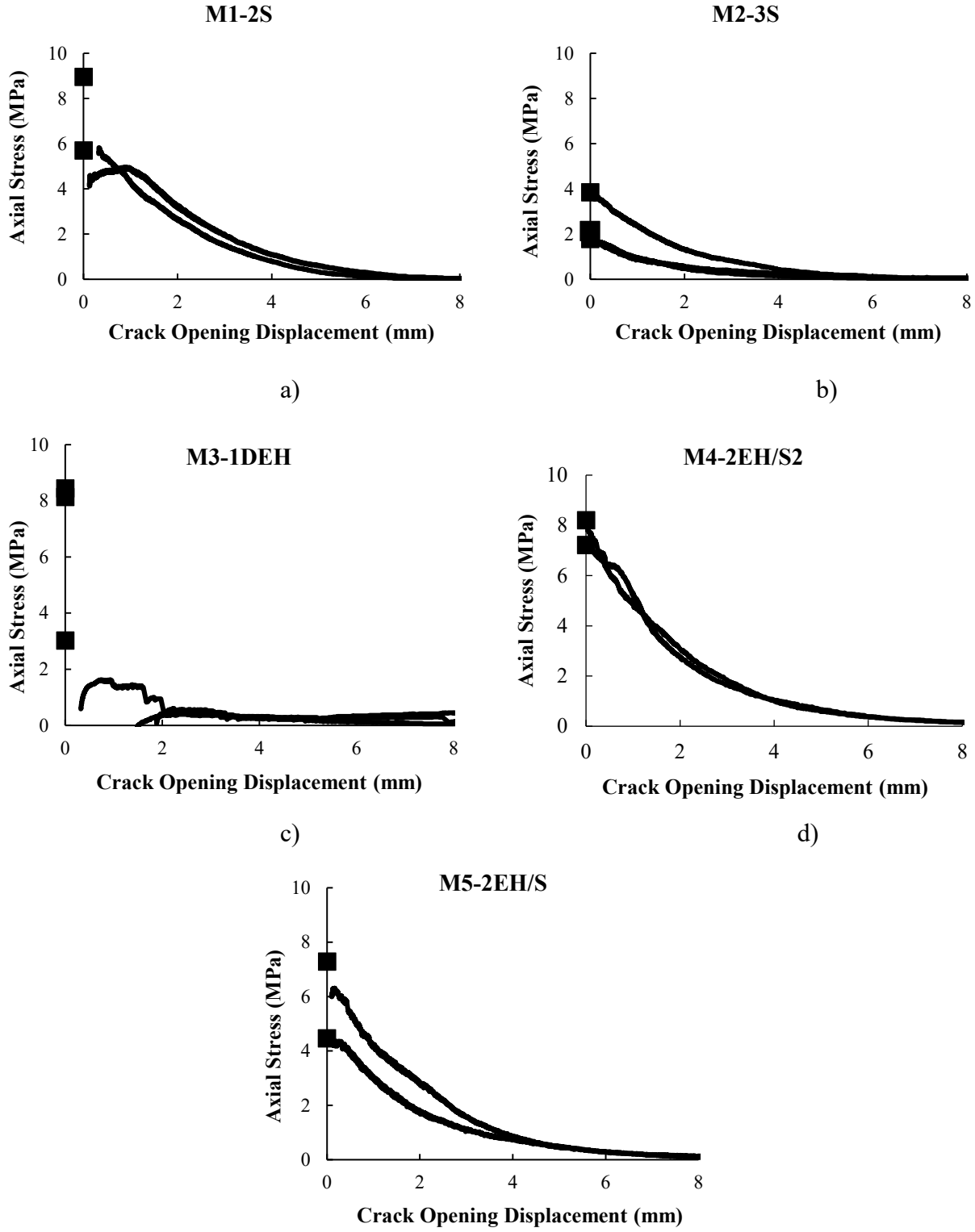

Figure 4.14 Axial stress versus crack opening displacement response for a) M1-2S, b) M2-3S, c) M3-1DEH, d) M4-2EH/S2, and e) M5-2EH/S

Two different types of the tensile behavior can be observed from the plots shown in Figure 4.9 through Figure 4.14. The first type of behavior is characterized by a gradual decrease of the axial stress with an increase in the crack opening displacement that occurs upon the major crack localization (M1-2S, M2-3S DB1, M3-1DEH, M5-2EH/S DB1). In this case, only one major crack was detected, which gradually propagated along the weakest cross-section along the surface.

The second type of the post-peak behavior was detected only in the specimens containing hybrid fibers (M4-2EH/S2, M5-2EH/S DB2). After the yield stress was reached and the first crack was initiated, the engagement of fibers induced several cracks (Figure 4.15). This multiple cracking behavior, which occurred along the gauge length, can be noticed by the saw-tooth shaped tensile response between the yield stress and the peak stress. At the peak stress this multiple micro-cracks coalesce and localize into one dominant macro-crack, which cause material softening behavior.

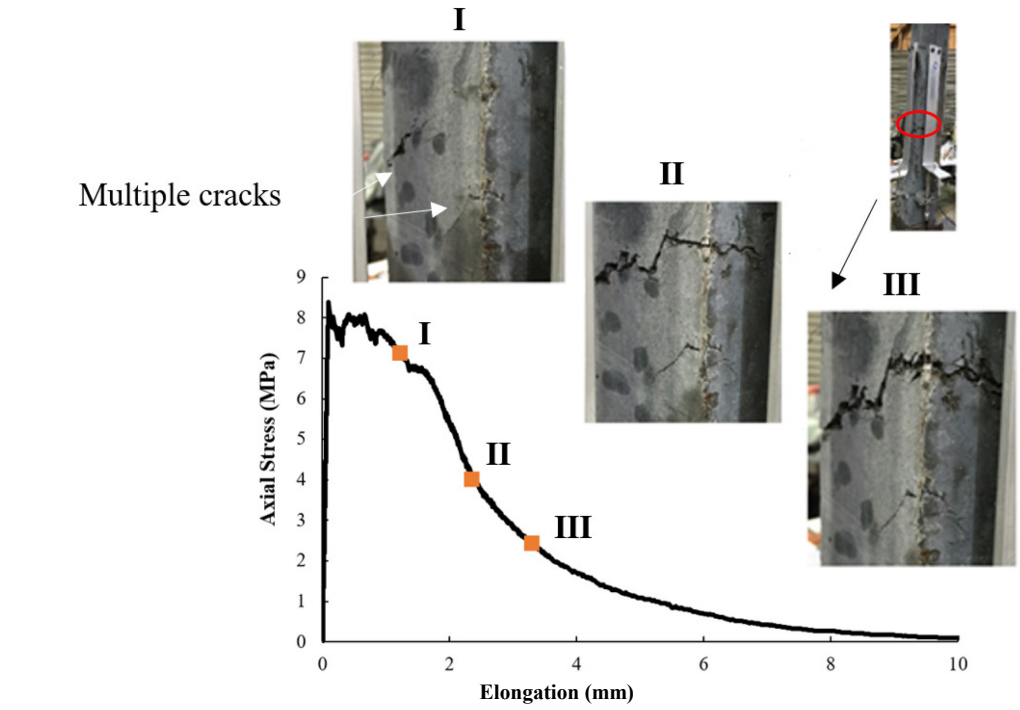

a)

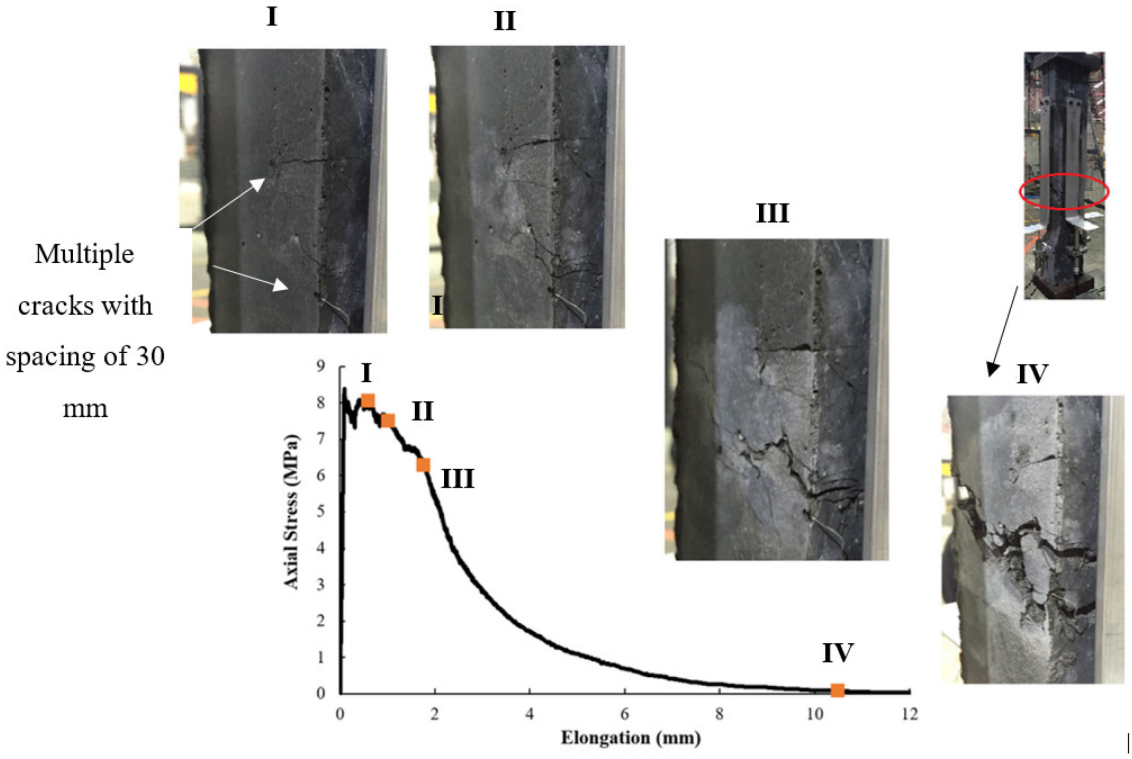

b)

Figure 4.15 Development of multiple cracks in the specimen DB1, mix M4-2EH/S2. Pictures were taken from two opposite sides of the specimen

As the crack opening displacement increased the load was gradually transferred to the fibers ultimately resulting in no contribution from the cementitious matrix. The mechanism responsible for residual load carrying capacity was bonding between the fibers and surrounding matrix. The final tensile failure of UHPFRCC occurred by the time at which the fibers started to debond from and to pull out of the cementitious matrix.

Unfortunately, two mix designs, M2-3S and M3-1DEH, have not behaved the way it was expected. In the case of the M3-1DEH, a response after the initial tensile cracking could not be reliably observed and examined because the universal testing machine controller temporarily lost control of the dog-bone specimen during the brittle initiation of the first tensile crack. When control was recouped, the specimen had undergone some tensile fiber pullout across the crack, and the critical portion of the UHPFRCC tensile behavior just after tensile cracking had been bypassed (Figure 4.11 b). This uncontrolled behavior was probably due to a lack of sensitivity of the universal testing machine control system due to its larger-than-necessary load capacity. Furthermore, in the case of M2-3S, low axial yield and peak stresses are probably due to a high volumetric fiber content, due to which a distribution and orientation of fibers within the dog bone specimens were not sufficiently random. Poor fiber distribution and orientation were indicated by observing the failure surface (Figure 4.16).

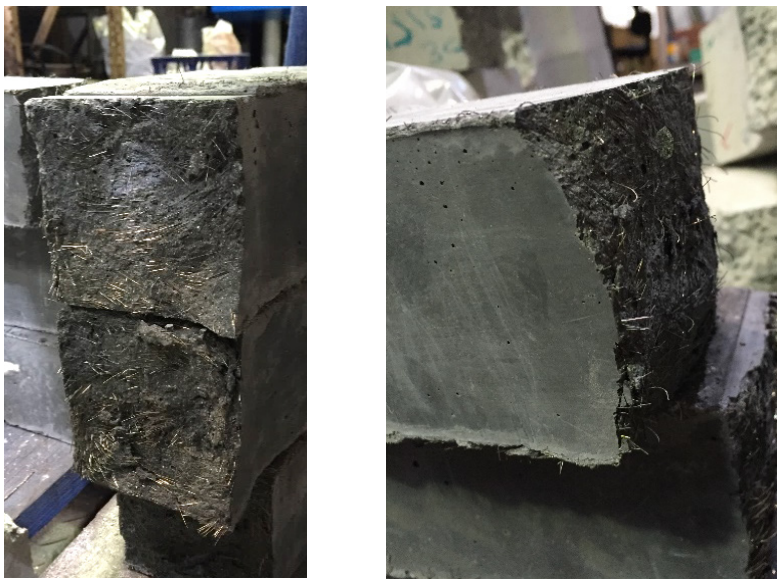

Figure 4.16 Photographs of the M2-3S failure surface with the poor fiber distribution and orientation

It can be seen from the uniaxial tension test results presented herein that the UHPFRCC dog-bone specimens exhibited high tensile yield, and peak stresses, along with ductile behavior, and increased fracture toughness. Other UHPFRCC enhancements were evident as well, such as strain hardening behavior accompanied with a multiple cracking.

4.3.2. Prism bending test

In order to evaluate a flexural behavior of UHPFRCC, four-point prism bending tests were performed on un-notched specimens. The ASTM C1609 Standard Test Method for Flexural Performance of Fiber-Reinforced Concrete (Using Beam with Third-Point Loading) [128] was followed. This method enables determination of the first crack, peak, and residual loads, and corresponding stresses. Moreover, determination of a specimen toughness based on the area under the load-mid-span deflection curve can also be performed based on this method.

For each mix design, the test was performed on up to the three un-notched beams having a 100 mm x 100 mm square cross section, a length of 550 mm and a span length of 456 mm. Prismatic specimens were tested using a closed loop, servo-controlled testing system. During a test, the applied load and the mid-span deflection of the prism were monitored and recorded. The mid-span deflection of a specimen was measured by the LVDTs, which were attached to the yoke on each side of the specimen at mid-span. A loading arrangement of four-point prism bending test is shown in Figure 4.17.

Figure 4.17 Deflection measurement setup for four-point prism bending test

The experimental data collected in the prism bending tests are presented in Figure 4.18 and summarized in Table 4.10. Abbreviations B1, B2, and B3 in the legend of Figure 4.18 denote the individual specimens. It can be seen from Figure 4.18 that the flexural response of the UHPFRCC consists of the three different phases. The first part is a linear elastic phase, which extends up to first cracking of the matrix. After the first crack occurs, a non-linear flexural hardening response takes place up to the peak load. This is followed by the second phase, during which a slight decrease in load-carrying capacity can be noticed. A saw tooth pattern visible in the second phase is an indication of cracks propagating and forming throughout the highly

stressed tension face of the prism. After a peak load is reached, load decreases further while the mid-span deflection increases. The third phase is characterized by the tensile fiber pullout. Moreover, for some concrete mixes (M1-2S, M5-2EH/S) four-point bending test showed a scatter in the test results, which is due to variations in fiber distributions and orientations, and it is expected to occur in this type of test ([129], [130], [131]).

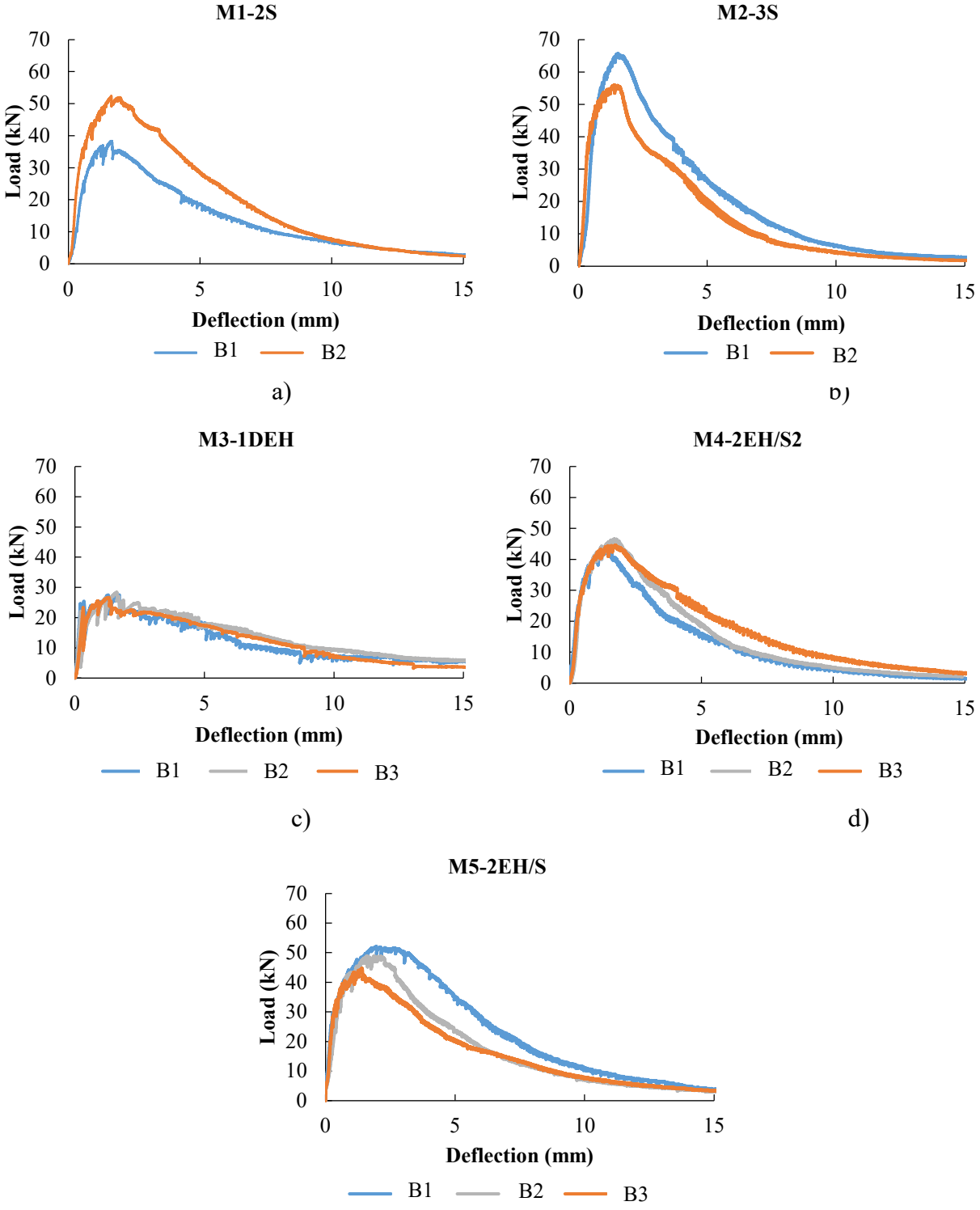

Figure 4.18 Load versus mid-span deflection results from the four-point prism bending tests: a) M1-2S, b) M2-3S, c) M3-1DEH, d) M4-2EH/S2, and e) M5-2EH/S

Table 4.10 provides the averaged results for the prisms in each set. One of the most important results from these tests is a first crack load of the UHPFRCC matrix because it is an indication of the tensile cracking strength of UHPFRCC. The mean load, stress, and deflection at first cracking denoted by P_f, $\sigma_{fl,f}$, and $d_{fl,f}$, respectively are given in Table 4.10 for each material. While the P_f and $d_{fl,f}$ are obtained directly from the graph, and $\sigma_{fl,f}$ is obtained using the following equation, which is based on linear elastic material subjected to a pure bending:

$$\sigma_{fl,f} = \frac{P_f L}{bd^2} \quad \textbf{4.6}$$

where L is a span length (mm), b is an average width of the prism, and d is an average depth.

Furthermore, results related to a peak load, P_p corresponding deflection, $d_{fl,p}$ and a corresponding flexural stress, $\sigma_{fl,p}$ are also listed in Table 4.10. The first cracking stress (yield stress) tended to be approximately 45 to 85 percent of the peak stress, depending on the volumetric fiber content, and water to binder ratio (Figure 4.19). The lower the volumetric fiber content, the closer to each other the values of the first crack stress and peak stress are. In the other words, a deflection-hardening part of the flexural response becomes less pronounced with a decreasing volumetric fiber content, thus indicating a more brittle flexural behavior. It should be noted that the first crack to peak stress ratio calculation is only for comparative purposes as this equivalent flexural peak stress has no physical meaning. It is because the UHPFRCC prism exhibits an extensive cracking at the peak load that the assumption of a pure bending in a linear, elastic cross section is not justified.

In characterization of cementitious materials, a specimen toughness, T is a term that provides a measure of energy absorption capacity of a tested specimen. Toughness is typically quantified in terms of the area under a load-deflection response curve up to the specific deflection levels. According to the ASTM C1609 [128], a toughness of the prismatic specimen

should be calculated at the mid-span deflection of $L/150$. The values of the toughness, residual load, P_r and stress, σ_r at the same deflection level ($L/150$) for all of the concrete mixes were obtained. They are presented in Table 4.10.

Table 4.10 ASTM C1609 strength results

Mix	χ_f (%)	First Crack			Peak			Residual		$T^{\#}$ (kJ)
		P_f (kN)	$d_{fl,f}$ (mm)	$\sigma_{fl,f}$ (MPa)	P_p (kN)	$d_{fl,p}$ (mm)	$\sigma_{fl,p}$ (MPa)	P_r* (kN)	σ_r** (MPa)	
M1-2S	2	31	0.57	14	45	1.63	20	36	16	115.5
M2-3S	3	37	0.44	16	61	1.47	27	39	17	144.6
M3-1DEH	1	23	0.25	10	28	1.54	12	22	9	72.6
M4-2EH/S2	2	21	0.27	9	45	1.62	20	33	15	116.4
M5-2EH/S	2	27	0.31	12	49	1.66	22	41	19	139.2

* The load value corresponding to a deflection of $L/150$ (3.04 mm)

** The stress value corresponding to a deflection of $L/150$ (3.04 mm)

\# Toughness of beam specimen at a net deflection of $L/150$ (3.04 mm)

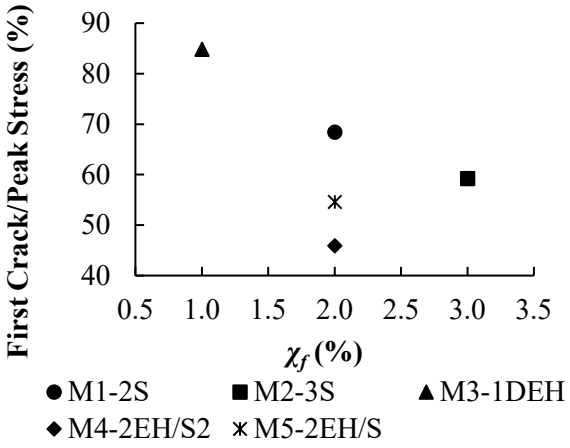

Figure 4.19 First crack stress to peak stress ratio versus volumetric fiber content for prism bending tests

Figure 4.20 depicts the variation of experimentally obtained ASTM C1609 strength results with the volumetric fiber content. The larger the volumetric fiber content, the higher the values of the material toughness, first crack, peak, and residual loads are. Moreover, the mix M4-

2EH/S2, which is denoted by the rhomboid symbol in Figure 4.20, has the highest water to binder ratio (w/b=0.19). This caused ASTM strength results to be lower than for the other mixes having equal volumetric fiber contents but less water added to the mix.

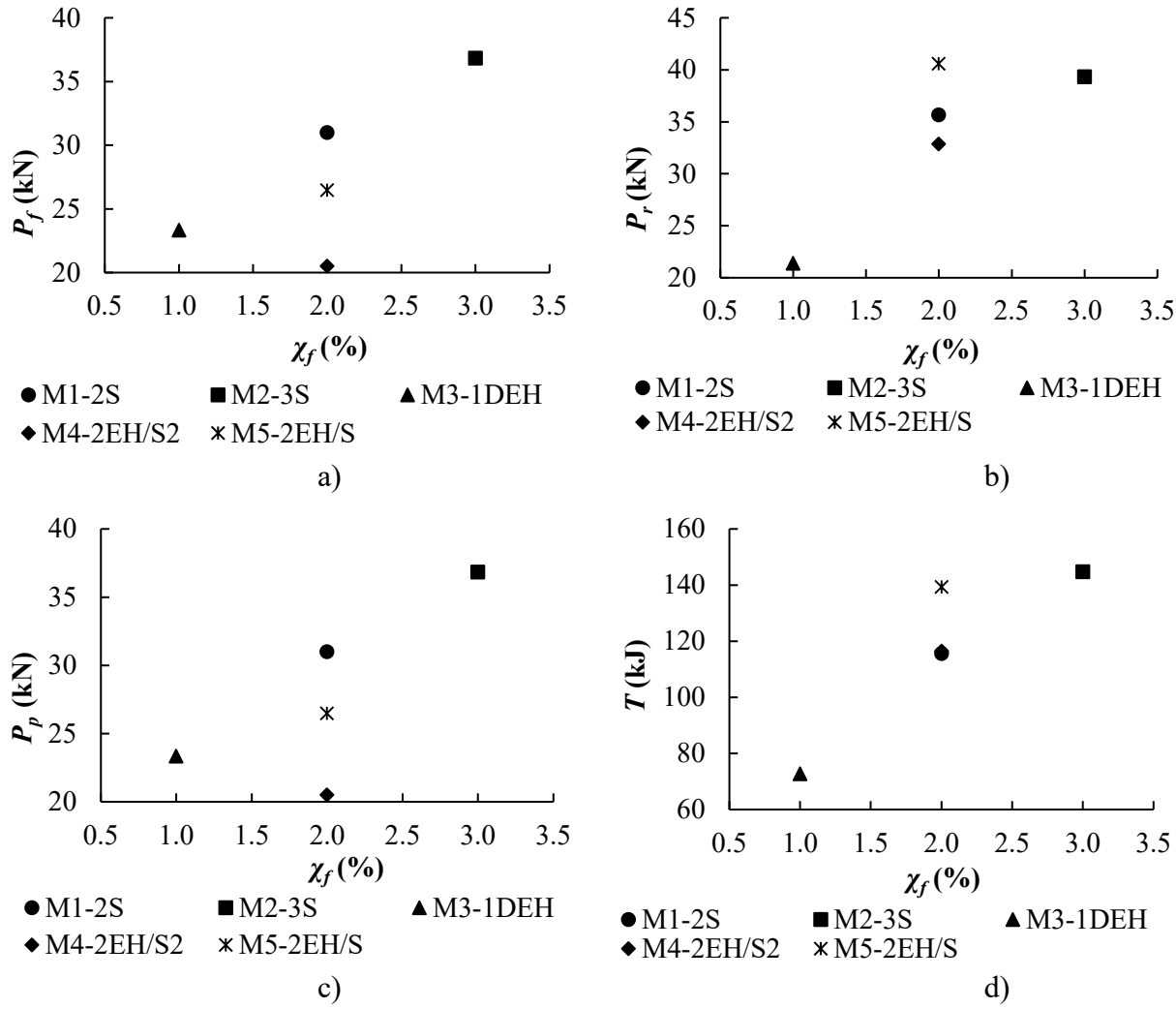

Figure 4.20 ASTM C1609 strength results: a) first crack load, b) peak load, c) residual load, and d) toughness versus volumetric fiber content

Two different failure modes are known to occur in the flexural performance tests. The first type is characterized by a single crack, which initiates at the weakest cross section of the specimen, and propagates directly toward the loading point with no other cracks branching out

from the initial one. This failure mode was observed during all of the four-point prism tests (Figure 4.21). The second type is characterized by multiple cracks and/or by a significant bifurcating from the initial crack. The second failure mode was not observed in this study.

Figure 4.21 Single dominant crack observed in prism bending test

Chapter 5 - Modeling of post-cracking behavior of UHPFRCC

5.1. Introduction

UHPFRCC is a specially tailored cement based composite with a compressive strength of 150 MPa and higher ([123], [124], [23], [5]). Moreover, this composite has a substantial post-cracking tensile capacity due to presence of steel fibers. Thus, it can exhibit a pseudo-strain hardening under tension and undergo multiple cracking prior to a macro-crack localization as seen from the experimental results presented in Chapter 4.

Although exhibiting such superior material properties, characterization of UHPFRCC tensile behavior is still a challenge. Furthermore, no agreement has been reached regarding a standard test setup and geometry of the specimen. Moreover, an additional reason why the UHPFRCC and FRCC in general have had a limited use in practice lies in a difficulty in establishing a post-cracking, tensile response of the FRCC, which is a fundamental property required for design of structural members manufactured from FRCC.

A characteristic tensile response of FRCC is linear elastic prior to matrix cracking. Thus, it can be represented by a σ-ε relationship. If strain hardening is accompanied by a multiple micro-cracking, which occurs after the linear elastic stage, a tensile response of FRCC can still be represented by a stress-strain relationship if smeared cracking approach is used. Once multiple micro-cracks coalesce into a macro-crack a tensile response becomes highly non-local and it should be described in terms of stress versus crack opening displacement relationship.

The σ-w relationship for UHPFRCC can be obtained directly from a direct tensile test without having to resort to inverse analysis methods, which was shown in Chapter 4.

Nevertheless, these direct tensile tests were arduous to perform, time-consuming, and they required sophisticated testing equipment.

Consequently, four-point prism bending tests were performed as a simpler and quicker alternative to direct tension tests. During the prism bending tests applied load and a mid-span deflection were measured. In order to characterize a post-cracking behavior from the corresponding direct tension test an inverse analysis was performed on prism bending tests. Specifically, a σ-w relationship was obtained from load verses mid-span deflection data. Therefore, the aim of this Chapter is to conduct inverse analyses and determine whether the prism bending tests could be used to characterize tensile responses of UHPFRCC in the direct tension tests.

To this end, the most recent types of inverse analysis methods for FRCC and UHPFRCC are used to predict the post-cracking responses observed in the direct tension tests. The predicted responses are subsequently compared to the experimentally observed responses, thus enabling an evaluation of performance of the employed models. These models that were used are: Amin's full model (Amin-FM) [32], Amin's simplified model (Amin-SM) [32], and Lopez's model [7]. Amin's full model [32] is an alternative model to the *fib* MC2010 [96], whereby the latter represents the most recent design guideline, which is contained in Eurocode 2 (European code for design of concrete structures) and other national guidelines. It was found in Amin [32] that *fib* MC2010 overestimates the residual tensile strength. Moreover, a simplified version of the Amin's model is featured in the Draft Australian Bridge Code: Concrete [94]. It is noted that both Amin's models were developed for FRCC. They are based on three-point prism bending test on notched specimens. Finally, the Lopez's model [6] for inverse analysis is chosen because

it is the most recent model developed specifically for the UHPFRCC based on un-notched four-point prism bending test, which was conducted in this study.

5.2. Amin's models

5.2.1. Amin's full model

Amin-FM [32] is a physics based model, which offers a simple, but effective inverse analysis procedure to determine a σ-w relationship from prism bending test.

The assumed post-cracking tensile σ-w relationship in a direct tension test is depicted in Figure 5.1. It can be seen that contribution of a plain cementitious matrix remains substantial immediately after a peak tensile stress $\sigma_{t,p}$ is reached. As the matrix contribution starts to decrease exponentially fibers reach their maximum contribution, which corresponds to an insignificant contribution of a matrix. The point, where the fibers reach their full capacity, is denoted by w_T in Figure 5.1.

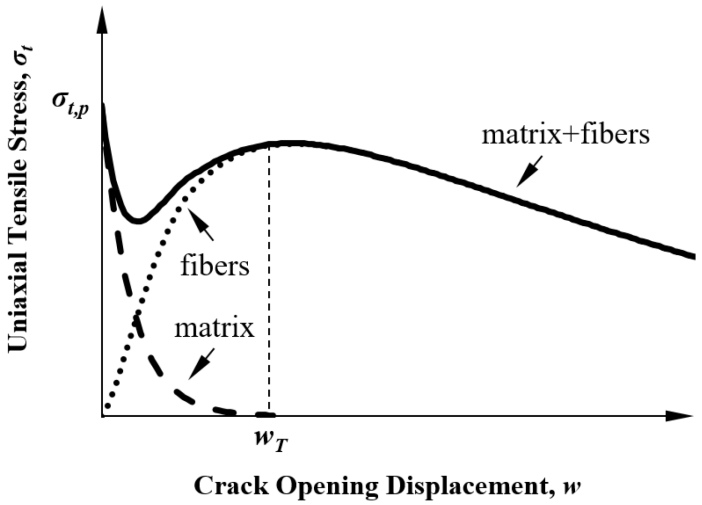

Figure 5.1 The tensile σ-w relationship for fiber reinforced concrete (adapted from [32])

Therefore, at a given crack opening, a stress in the fiber reinforced cementitious composite $\sigma_t(w)$ is additively decomposed into a stress in the un-reinforced matrix $\sigma_c(w)$ and a stress carried by fibers $\sigma_f(w)$. It is given by

$$\sigma_t(w) = \sigma_c(w) + \sigma_f(w) \tag{5.1}$$

A stress in the un-reinforced cementitious composite for a given crack opening can be expressed as follows ([132], [5], [133]):

$$\sigma_c(w) = \sigma_{t,p} e^{-cw} \tag{5.2}$$

where the coefficient c depends on the maximum aggregate size and volumetric fiber content, χ_f. For a mortar and aggregate sizes smaller than 10 mm, c is given by the following expression [134]:

$$c = 30/(1+100\chi_f) \tag{5.3}$$

Furthermore, a stress carried by fibers $\sigma_f(w)$ can be expressed as [32]:

$$\sigma_f(w) = \zeta(w) f_w \tag{5.4}$$

where f_w is a tensile stress carried by fibers in the corresponding prism bending test, and $\zeta(w)$ is an elliptical transition function given by [135]:

$$\zeta(w) = \begin{cases} \sqrt{1 - \dfrac{(w_T - w)^2}{w_T}} & \text{if } w < w_T \\ 1 & \text{if } w < w_T \end{cases} \tag{5.5}$$

The transition function is used to describe a progressive engagement of fibers after the onset of macro-cracking [135].

Moreover, it is assumed that the un-cracked matrix has no contribution towards the average tensile stress f_w carried by the beam, which is in turn assumed to undergo a rigid body

motion depicted in Figure 5.2. The parameters d_n, and d_r denoted in Figure 5.2 stand for the depths from extreme compressive, and tensile fiber to the neutral axis, respectively. The distance between the centroids of the tensile, and compressive stress blocks is so-called a lever arm and is denoted by z, while the distance between the centroids of the tensile stress blocks and the neutral axis is denoted with d_r^*. A resulting tensile stress carried by fibers f_w is then given by:

$$f_w = \frac{k_1 k_2 Pa}{D^2 b} \qquad \textbf{5.6}$$

where D and b are depth and width or the prism respectively, and a is one-third of a span length in the case of a four-point bending test. The coefficient k_1 depends on the ratio between a depth of the neutral axis and depth of the prism, while the coefficient k_2 takes into account the influence of the notch in the case of the notched prism specimens. In this study $k_1 k_2 \approx 1$ because un-notched specimens were used. The reader is referred Amin [32], Amin et al. [135] for further details.

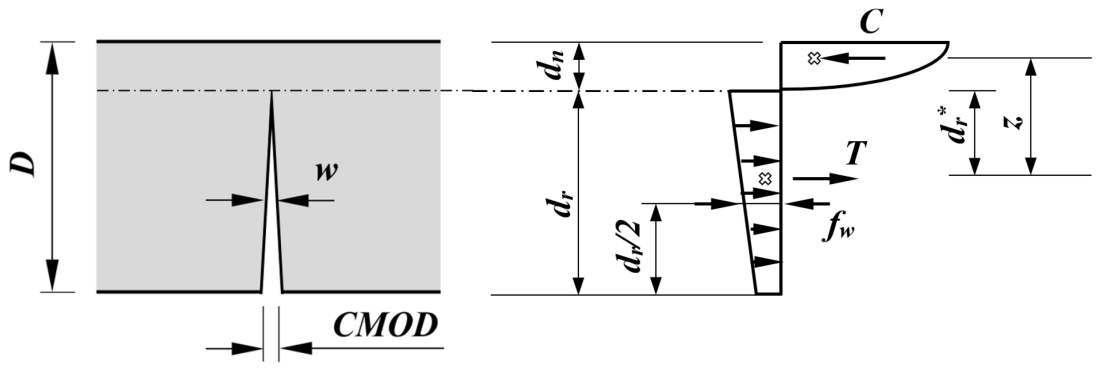

Figure 5.2 Stress distribution at the cracked section of FRCC prism in bending (adapted from [32])

Moreover, it is because four-point prism bending tests were carried out on un-notched specimens that load versus mid-span deflections were measured. In order to obtain a

corresponding CMOD values a simple conversion from a mid-span displacement to CMOD was performed. It is based on rigid body rotations of the two prism halves centered about the crack tip, and the assumption that failure occurs along a single crack [9]. The relationship between the CMOD and the mid-span deflection, δ is given by:

$$CMOD = \frac{4D\delta}{L} \quad \textbf{5.7}$$

Based on the above assumptions, a crack opening displacement from a direct tension test is assumed to be equal to one-half of the CMOD.

The experimental results of direct tensile tests and four-point prism bending tests are presented in Chapter 4. It is important to note that the tensile behavior of FRCC specimen is sensitive to the orientation of fibers within the matrix. In addition, a presence of boundaries (walls of the casting mold) restricts fibers from being freely orientated within the matrix ([134], [20], [136]). This is a so-called boundary or wall effect. Therefore, prior to comparing the direct tensile test data with the results obtained from the inverse analysis, the former need to be modified to account for the orientation effect. In the other words, the orientation factor k_t converts the actual experimental results to those equivalent to the three-dimensional fiber distribution and orientation, which are free from the wall effects. For example, if tensile specimens were obtained by coring out of a larger section, such as a slab, the boundary effect would be negligible, thus resulting in k_t being equal to one. The orientation factor for the specimen with the square cross section and tested in the direct tension is given by Lee et al. [136] as follows:

$$k_t = 0.5 \le \frac{1}{0.94 + 0.6 l_f / b} \le 1 \quad \textbf{5.8}$$

Moreover, the same correction applies to the prism bending test results except that the orientation factor k_b is now different. It is adopted from Ng et al. [134] and is given by:

$$k_b = \frac{\pi}{3.1 + 0.6 l_f / b} \leq 1 \qquad \textbf{5.9}$$

Finally, applying the inverse analysis technique (Eqs. 5.1- 5.6) to the results of the four-point prism bending tests produces σ-w results depicted in Figure 5.3. In order to evaluate the performance of the Amin-FM model, predicted σ-w results are compared with the experimentally obtained uniaxial tension data (denoted with DB1, DB2 or DB3 in Figure 5.3), whereby the latter have been modified by accounting r for the wall effect.

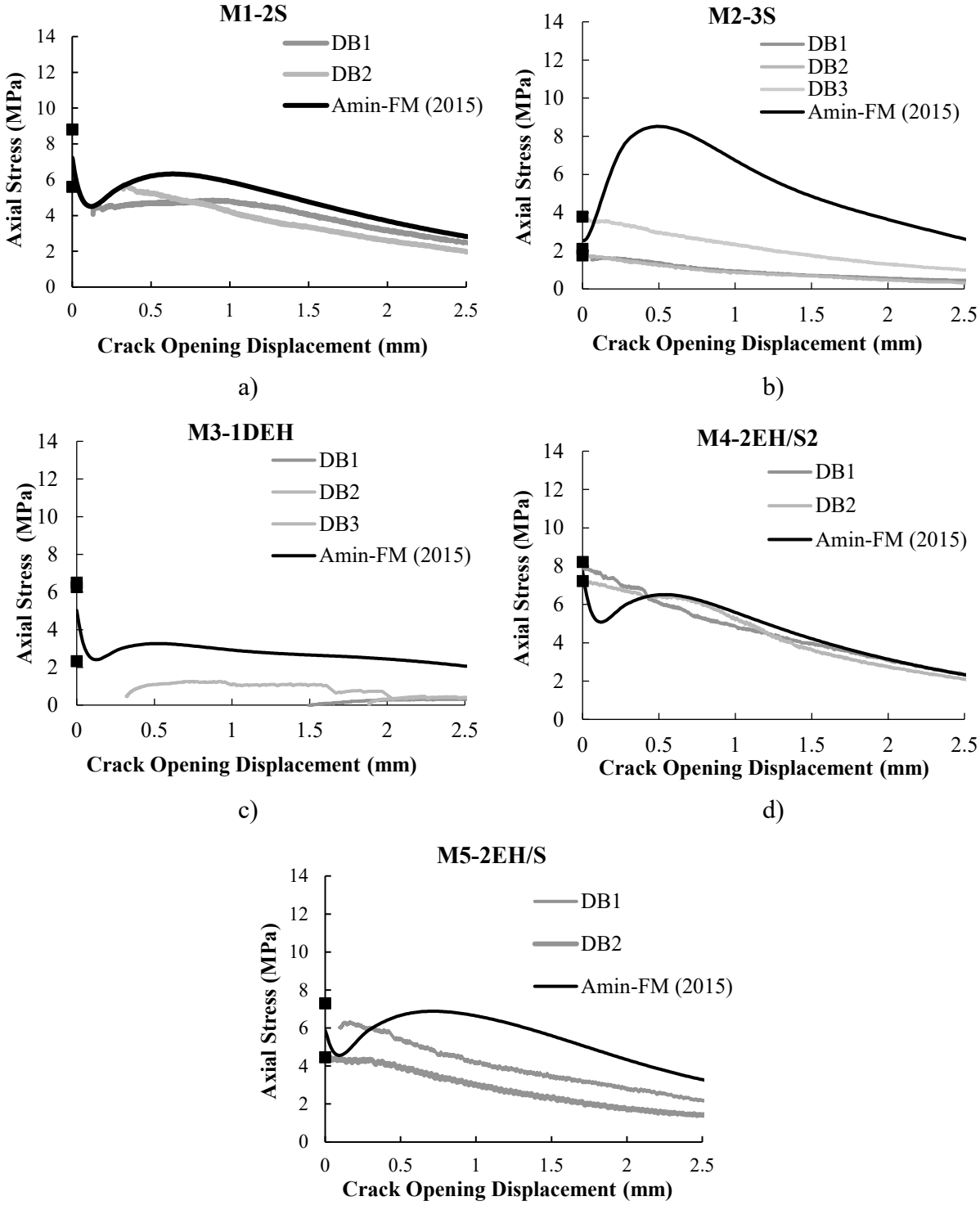

Figure 5.3 Predictions of Amin-FM compared with the experimental data from uniaxial tests: a) M1-S2, b) M2-3S, c) M3-1DEH, d) M4-2EH/S2, and e) M5-2EH/S

It can be seen that in the case of mixes M1-S2, M4-2EH/S2, and M5-2EH/S the proposed model fits the experimental data very well whereby the best prediction was obtained for M4-2EH/S2. Predictions are slightly non-conservative. In the case of the remaining two mixes, Amin-FM significantly over estimates the σ-w behavior. This is due to a significant discrepancy between the prism bending and direct tension tests, thus resulting in unsatisfactory experimentally observed responses in direct tension tests for these two mixes. Further evaluations of performance of all models are presented at the end of this Chapter, after the predictions of each individual model have been presented.

5.2.2. Amin's simplified model

Although the full Amin's model provides worthy results, it needs to be simplified for design purposes (Amin-SM). Therefore, Amin [32] developed a simplified version of the post-cracking residual tensile strength (σ-w relationship) of FRCC (Amin-SM). The model is featured in the Draft Australian Bridge Code: Concrete [94].

In the development of the simple model, the philosophy for predicting the tensile residual stress is adopted from the *fib* MC2010 [96]. The *fib* MC2010 model is defined by two reference values f_{Fts} and $f_{Ftu,}$ which are the post-cracking strengths corresponding to crack openings significant for serviceability limit state (SLS) and ultimate limit state (ULS), respectively. A limit state is a condition of a structure beyond which it no longer fulfills the relevant design criteria [137]. Moreover, SLS is characterized by CMOD of 0.5 mm, while the ULS corresponds to the CMOD of 2.5 mm. Crack mouth opening displacements corresponding to SLS and ULS are depicted in Figure 5.4, and denoted with $CMOD_1$ and $CMOD_3$ respectively.

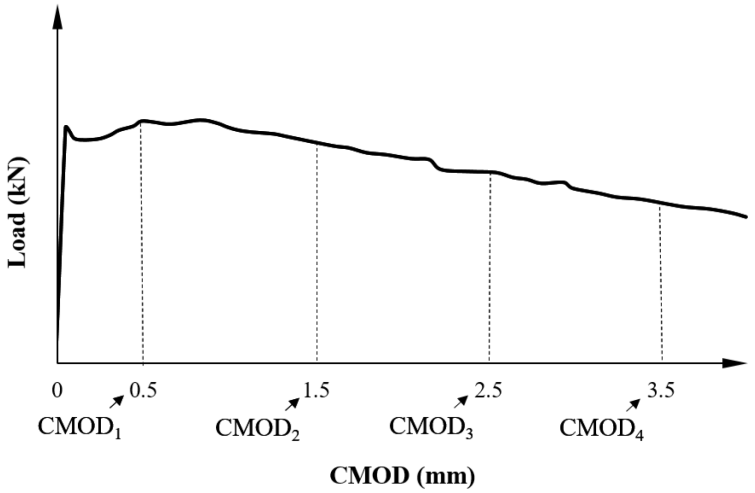

Figure 5.4 Definition of the key points on the applied load versus CMOD curve (adapted from [30])

As previously discussed, Amin-FM model assumes that the contribution of the un-cracked cementitious composite to the tensile stress in a prism is negligible, which is not the case at the $CMOD_1$ (0.5 mm). In addition, results from Amin [32] showed, that the contribution of the concrete at the $CMOD_1$ is approximately 14%. Therefore, in the derivation of the simple model, new points corresponding to CMODs of 1.5 and 3.5 mm were adopted. They are denoted as $CMOD_2$ and $CMOD_4$ in Figure 5.4. This new first sampling point $CMOD_2$ should be sufficiently far away from the initial cracking, so that the contribution of the un-cracked cementitious composite to the tensile stress remains relatively small. $CMOD_4$ is moved to 3.5 mm so that it is sufficiently distanced from $CMOD_2$ in order to provide a reasonable model for the σ-w relationship.

Finally, considering Eqs. 5.1-5.6 with a linear constitutive law interpolating between points $CMOD_2$ and $CMOD_4$, and an un-notched specimen results in the following equation for $\sigma(w)$:

$$\sigma_t(w) = \frac{f_{R2}}{3} + (f_{R4} - f_{R2})\left(\frac{w}{3} - \frac{1}{4}\right) \geq 0 \qquad \textbf{5.10}$$

$$f_{R,j} = \frac{3F_j a}{bD^2} \qquad \text{j =2,4 (no summation)} \qquad \textbf{5.11}$$

where f_{Rj} are residual flexural tensile strengths at $CMOD_j$.

The obtained residual tensile strengths at $CMOD_2$ and $CMOD_4$ from the prism bending tests for all five mixes are summarized in Table 5.1.

Table 5.1 Residual flexural tensile strengths at $CMOD_2$ and $CMOD_4$

Mix	f_{R2} (MPa)	f_{R4} (MPa)
M1-S2	18.78	12.55
M2-3S	23.61	12.52
M3-1DEH	9.42	7.69
M4-2EH/S2	18.74	10.84
M5-2EH/S	20.62	14.79

Inserting these values in the Eq. 5.10 gives the post-cracking σ-w predictions depicted in Figure 5.5. Experimental direct tensile data corrected for the wall effects are also included in Figure 5.5.A very good agreement between the experimental data and predictions of the simplified model is observed, especially for mix M4-2EH/S2. Again, the exceptions are mixes M2-3S and M3-1DEH for the same reasons mentioned before in case of Amin's full model.

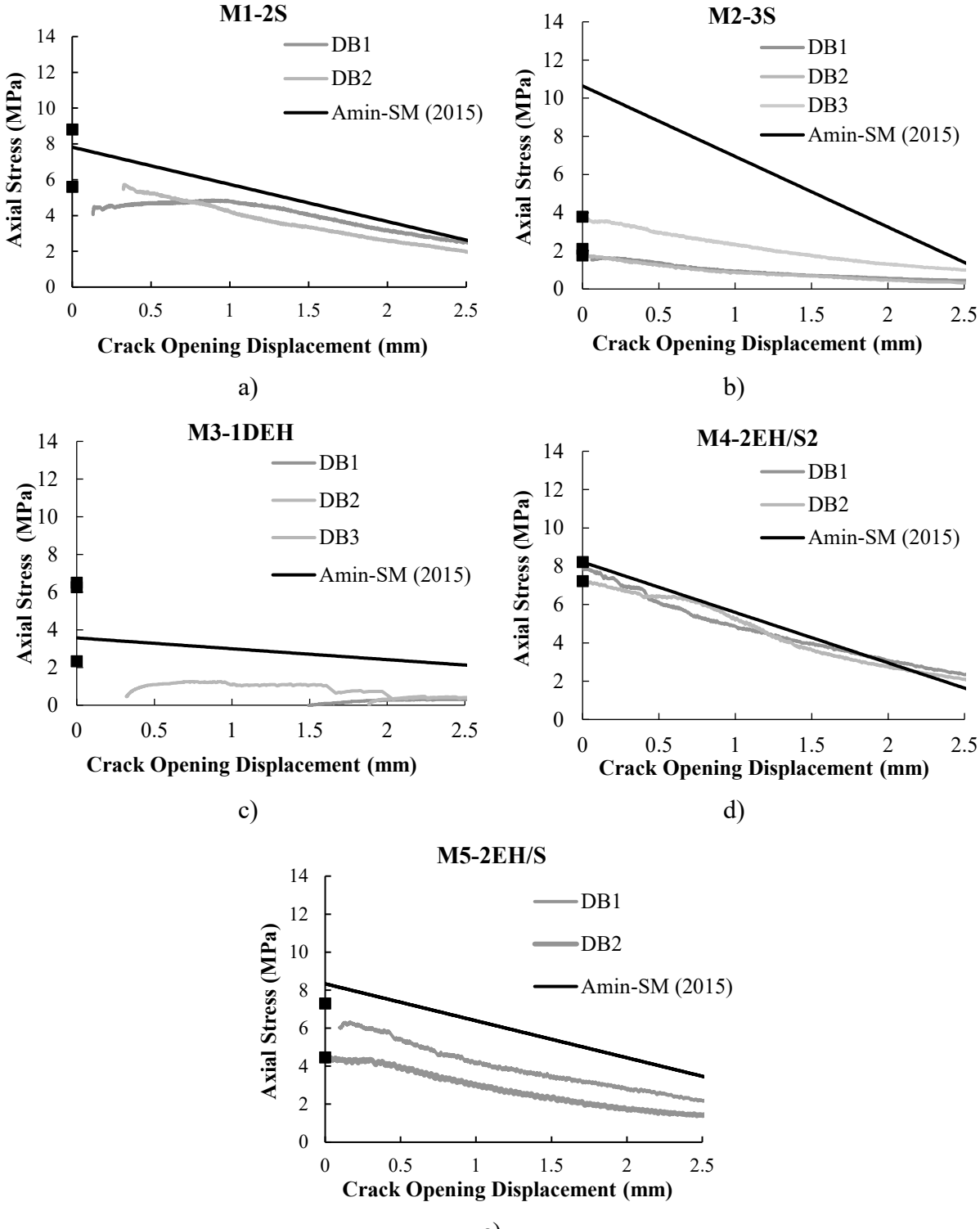

Figure 5.5 Predictions of the Amin-FM compared with the experimental data from uniaxial tests: a) M1-S2, b) M2-3S, c) M3-1DEH, d) M4-2EH/S2, and e) M5-2EH/S

In summary, although both Amin's models [32] have been developed for the post-cracking modeling of the stress–crack opening displacement responses of a steel fiber reinforced concrete, the results obtained in this study indicate that the models predict the post-cracking behavior of UHPFRCC specimens with a high accuracy as well. It should be noted that a limited number of prism bending and direct tension tests were performed. However, the available results presented herein give a good insight into the performance of Amin's models for post-cracking behavior of UHPFRCC. For more substantial conclusions more experimental data is needed.

5.3. Lopez's model

More recently, Lopez et al. [7] proposed a new and simplified inverse analysis developed specifically for the UHPFRCC based on un-notched four-point prism bending test. Moreover, the method showed a potential not only for using a four-point prism bending testing as an alternative to uniaxial testing, but also for characterizing both, a strain hardening and strain softening responses of UHPFRCC. Because of these encouraging initial results, it was decided to apply this method to experimental data obtained in this study.

The analytical model is based on a linear elastic constitutive σ-ε relationship in uniaxial compression and a quadri-linear one in tension. Both constitutive laws, for compression and tension are depicted in Figure 5.6 a), b) and c). Moreover, it can be seen from Figure 5.6 a) and b) that a total of six parameters is needed to fully define the compressive and tensile laws. They include Young's modulus E, first cracking tensile strength $\sigma_{t,f}$; ultimate tensile strength $\sigma_{t,p}$ and its corresponding strain $\varepsilon_{t,p}$; strain at the intersection of the softening lines $\varepsilon_{t,d}$ and the maximum strain $\varepsilon_{t,max}$, which corresponds to zero stress. The unloading modulus, E^* is also included.

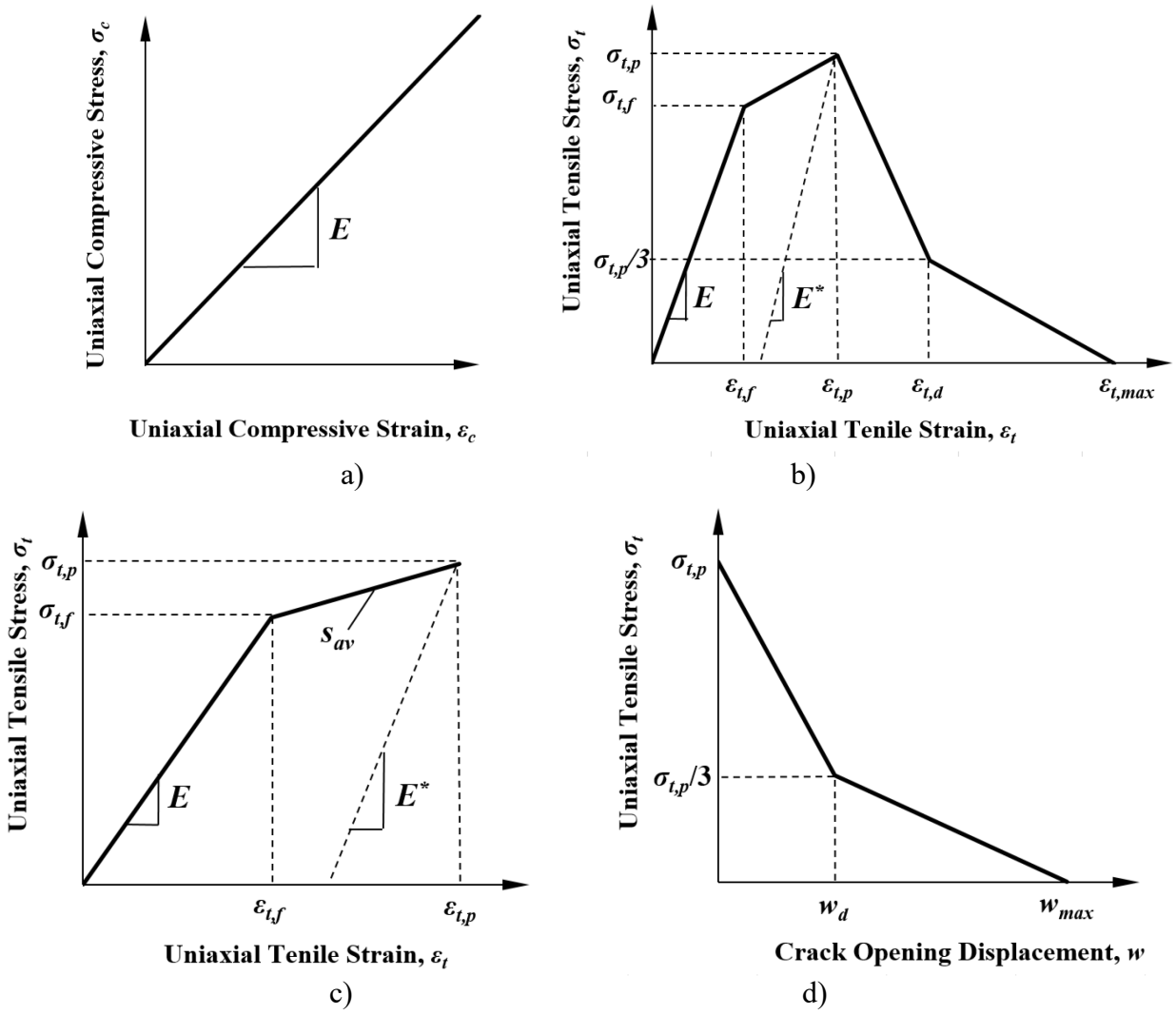

Figure 5.6 σ-ε relationship in a) uniaxial compression, b) and c) uniaxial tension, d) σ-w relationship for the post-cracking response in tension (adapted from [7])

In order to perform the inverse analysis and determine a uniaxial tensile σ-ε relationship, the five key points need to be extracted from an experimental flexural stress-mid-span deflection curve. These points are illustrated in Figure 5.7 and are determined as follows:

I. The intersection of the prism bending response curve and a straight line that passes through the origin having slope equal to 75% of initial secant stiffness (σ_{75}, δ_{75});

II. The intersection of the prism response curve and a straight line that passes s through the origin having slope equal to 40% of initial secant stiffness (σ_{40}, δ_{40});

III. A crack localization point corresponding to 97% of the maximum flexural strength on the loading branch of prism bending test results (σ_{loc}, δ_{loc});

IV. The point where flexural stress equals to 80% of the stress at crack localization point located on the post-peak softening branch of a prism bending response curve (σ_{80u}, δ_{80u}); and,

V. The point where flexural stress equals to 30% of the stress at crack localization point located on the post peak softening branch of a prism bending response curve (σ_{30u}, δ_{30u}).

For the detailed justification and validation of key point selection, the reader is referred to [7].

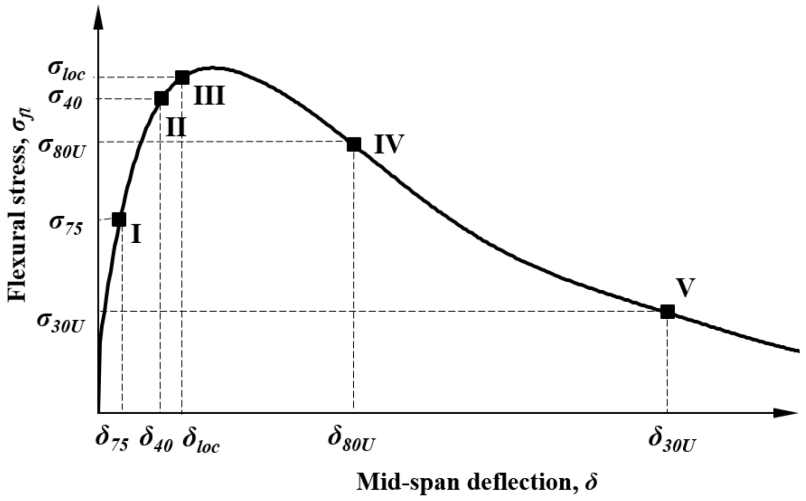

Figure 5.7 Schematic illustration of the proposed five key points from the prism bending test (adapted from [7])

Moreover, a statistical analysis of theoretical flexural stress versus mid-span deflection analytical curves was conducted. This provided a relationship between flexural and tensile behaviors. The resulting simplified inverse analysis equations for the prismatic beams with *L/D*=4.5 are given as follows:

$$\sigma_{t,f} = \frac{\sigma_{75}}{1.59}\left(\frac{\sigma_{75}}{\sigma_{40}}\right)^{0.21} \quad \textbf{5.12}$$

$$\varepsilon_{t,p} = \frac{\sigma_{t,f}}{E}\left(6.65\frac{\delta_{loc}}{\delta_{75}} - 9.40\right) \quad \textbf{5.13}$$

$$\sigma_{t,p} = \sigma_{t,f}\left(2.24\frac{\sigma_{loc}}{\sigma_{75}} - 1.55\right)\left(\frac{\varepsilon_{t,p}}{\varepsilon_{t,f}}\right)^{-0.17} \quad \textbf{5.14}$$

$$\varepsilon_{t,d} = \frac{\sigma_{t,f}}{E}\left(2.82\frac{\delta_{80u}}{\delta_{loc}} - 1.68\right)\left(\frac{\sigma_{t,p}}{\sigma_{t,f}}\right)^{-0.38}\left(\frac{\varepsilon_{t,p}}{\varepsilon_{t,f}}\right)^{0.89} \quad \textbf{5.15}$$

$$\varepsilon_{t,\max} = 2.17\frac{\sigma_{t,f}}{E}\left(\frac{\delta_{80u}}{\delta_{loc}}\right)^{1.86}\left(\frac{\varepsilon_{t,d}}{\varepsilon_{t,f}}\right)^{-0.76}\left(\frac{\sigma_{t,p}}{\sigma_{t,f}}\right)^{-0.26}\left(\frac{\varepsilon_{t,p}}{\varepsilon_{t,f}}\right)^{1.48} \quad \textbf{5.16}$$

The proposed equations define a complete quadri-linear *σ*-*ε* relationship in uniaxial tension. This relationship holds only if a multiple micro-cracking is observed in a prism bending test. However, if only a single macro-crack occurs, the ascending branch of the tensile response needs to be characterized by the *σ*-*w* relationship (Figure 5.6 c) and d)). Applying the fictitious crack modeling approach by [99] the *σ*-*w* relationship can be obtained as follows:

$$w_0 = \varepsilon_{t,u} s_{av} \quad \textbf{5.17}$$

$$w_d = w_0 + (\varepsilon_{t,u} - \varepsilon_{t,d} - \frac{2f_{t,u}}{3E^*})\frac{L}{3} \quad \textbf{5.18}$$

$$w_{\max} = w_0 + (\varepsilon_{t,\max} - \varepsilon_{t,d} - \frac{f_{t,u}}{E^*})\frac{L}{3} \quad \textbf{5.19}$$

where w_o, w_d, w_{max} are initial, intersectional, and maximum crack opening displacements (Figure 5.6 d), respectively, while s_{av}, is an average crack spacing. If no data is available for s_{av}, and E^*, values of w_o and E^* should be assumed to be zero and infinity, respectively.

Finally, based on the previously presented Lopez's model, the five key parameters are determined from the four-point prism bending test results obtained in this study. The results are summarized in Table 5.2 for all five mixes.

Table 5.2 Input parameters for the Lopez's model obtained from the four-point prism bending test results

Mix	σ_{75} (MPa)	δ_{75} (mm)	σ_{40} (MPa)	σ_{loc} (MPa)	δ_{loc} (mm)	δ_{80u} (mm)	δ_{30u} (mm)
M1-S2	16.13	0.48	21.78	22.70	1.42	3.36	7.40
M2-3S	19.65	0.48	25.37	24.90	0.90	2.40	5.91
M3-1DEH	7.66	0.37	10.64	10.46	0.90	4.20	11.10
M4-2EH/S2	13.99	0.42	19.83	19.30	0.96	2.73	6.54
M5-2EH/S	13.52	0.39	20.28	20.48	1.20	3.66	8.13

After determination of the key parameters from the prism bending tests, and after performing the inverse analysis (Eqs. 5.12-5.19) output parameters were obtained. They are summarized in Table 5.3.

Table 5.3 Predicted uniaxial tensile parameters

Mix	$\sigma_{t,f}$ (MPa)	$\sigma_{t,p}$ (MPa)	$\varepsilon_{t,p}$ (-)	w_d (mm)	w_{max} (mm)
M1-S2	8.35	9.11	0.0020	1.62	4.13
M2-3S	11.71	12.43	0.0014	0.97	3.05
M3-1DEH	4.49	4.87	0.0023	3.01	8.53
M4-2EH/S2	8.18	9.38	0.0021	1.51	4.29
M5-2EH/S	7.81	9.55	0.0038	2.66	2.66

Finally, Figure 5.8 depicts the predicted simplified strain hardening σ-ε response up to the ultimate tensile strength. The results are also compared with the corresponding uniaxial test data. It can be seen that the Lope's model predicts the first cracking stress very well, with the exception of M2-3S and M3-1DEH. Moreover, a strain hardening behavior was experimentally observed only in the case of M2-3S (DB2 and DB3), M4-2EH/S2, and M5-2EH/S (DB-2). In the case of M2-3S (DB2 and DB3) (Figure 5.8 b), and M5-2EH/S (DB-2) (Figure 5.8 e) the Lopez's model follows the general trend of strain hardening, but the stresses obtained experimentally are much lower than the predicted ones. In the case of M4-2EH/S2 (Figure 5.8 d), the Lopez's model correlates with experimental data very well.

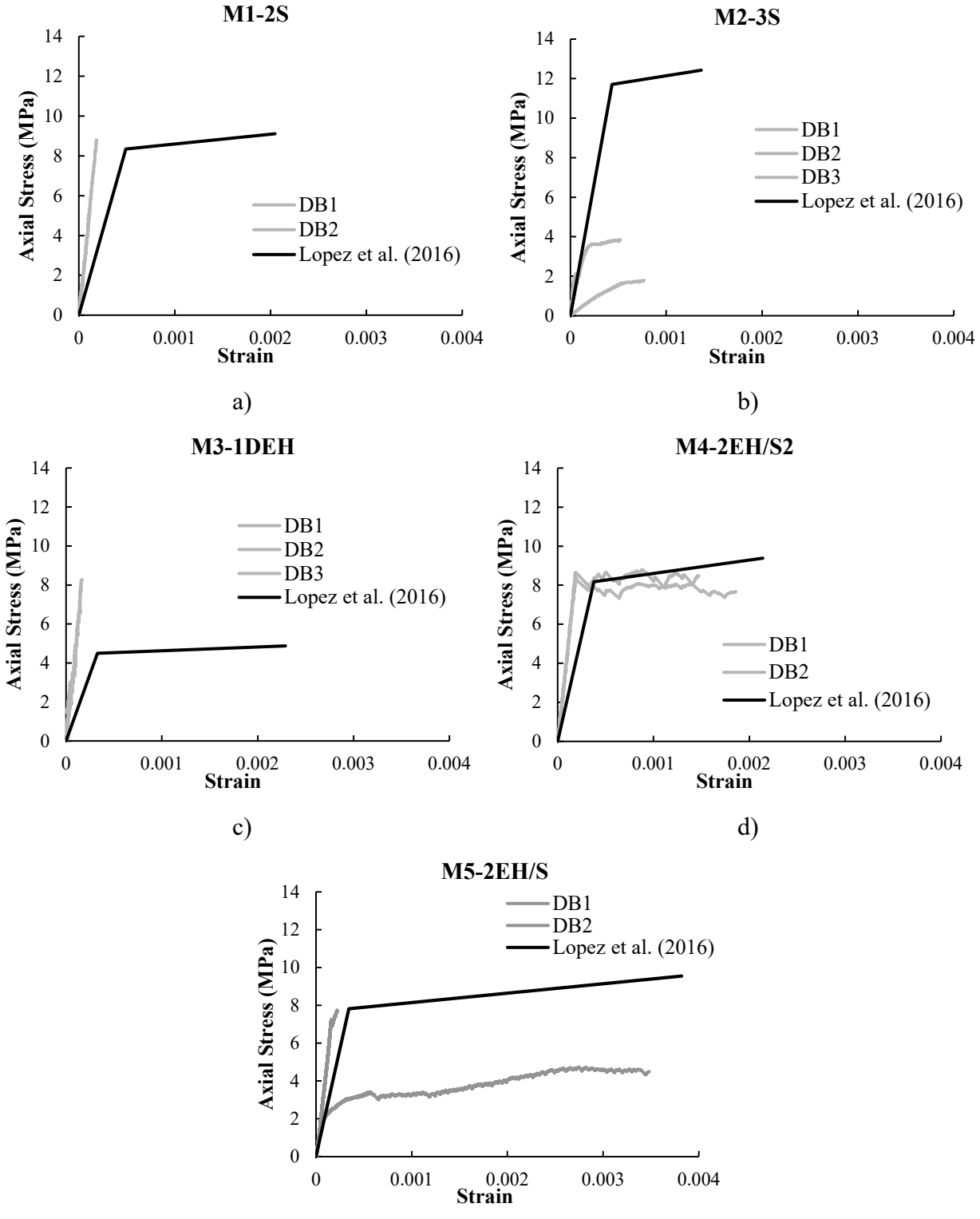

Figure 5.8 Predictions of σ-ε relationship based on Lopez's model compared with the experimental data from uniaxial tests: a) M1-S2, b) M2-3S, c) M3-1DEH, d) M4-2EH/S2, and e) M5-2EH/S

Figure 5.9 compares experimentally obtained uniaxial tensile data with the σ-w relationship predicted by the inverse analysis. Overall, Lopez's model shows a good agreement with the uniaxial test results. Magnitudes of predicted stresses are slightly higher than indicated by the experimental data in the first part of the descending branch of the σ-w curve, right after the peak tensile stress is reached. However, after the inflexion in the curve, Lopez's model becomes slightly conservative for tests M1-2S, and M4-2EH/S2.

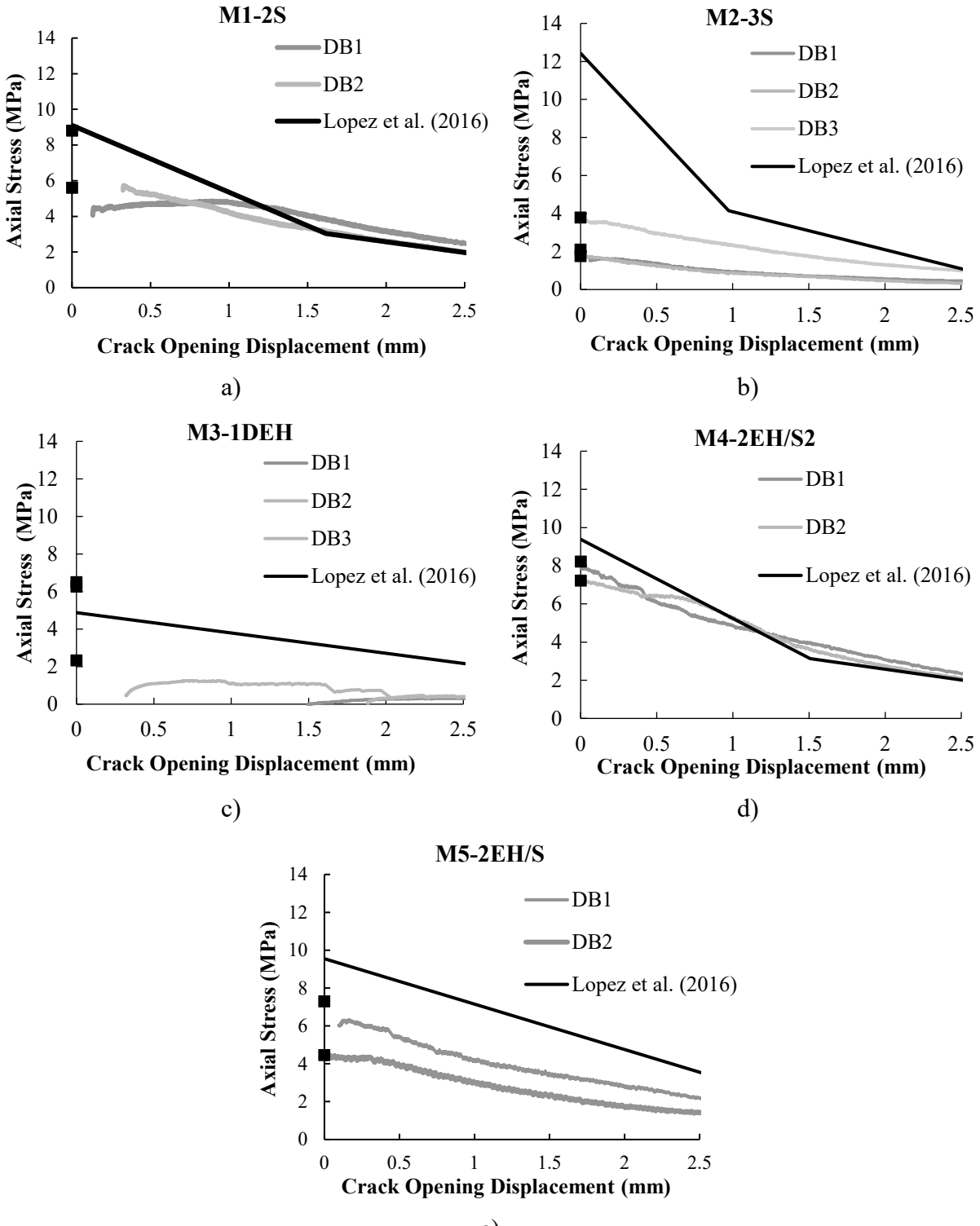

Figure 5.9 Predictions of Lopez's model compared with the experimental data: a) M1-S2, b) M2-3S, c) M3-1DEH, d) M4-2EH/S2, and e) M5-2EH/S

5.4. Comparison and conclusion

In general, all three models showed a very good agreement with the experimentally obtained uniaxial tensile data of UHPFRCC, especially for the experiments where direct tension and prism bending exhibit similar behaviors. This suggests that the four-point prism bending test combined with an inverse analysis is a viable alternative for characterization of tensile behavior to a uniaxial tension test.

Predictions of uniaxial tensile stresses at crack opening displacements of 0.5 mm, 1.5 mm and 2. 5 mm, which were obtained from the three different inverse analyses along with the experimental data, are presented in Table 5.4 through Table 5.6. It is noted that too high values of a coefficient of variation (COV) are obtained based on all five mixes. This is due to significant discrepancies between uniaxial tension and prism bending results for mixes M2-3S, and M3-1DEH.

Table 5.4 Comparisons of the Amin-SM, Amin-FM and Lopez's models with the experimental data for all five mixes at the w=0.5 mm

Mix	Exp.	Amin-SM (2015)		Amin-FM (2015)		Lopez et al. (2016)	
	σ_t (MPa) -A-	σ_t (MPa) -B-	B/A	σ_t (MPa) -C-	C/A	σ_t (MPa) -D-	D/A
M1-S2	4.98	6.81	1.37	6.18	1.24	7.23	1.45
M2-3S	1.87	8.84	4.72	8.52	4.55	8.17	4.37
M3-1DEH	1.09	3.29	3.02	3.26	2.99	4.33	3.98
M4-2EH/S2	6.29	6.94	1.10	6.50	1.03	7.31	1.16
M5-2EH/S	4.99	7.39	1.48	6.63	1.33	8.35	1.67
Mean			2.34		2.23		2.53
COV			0.65		0.68		0.60
Standard deviation			1.53		1.52		1.52

Table 5.5 Comparisons of the Amin-SM, Amin-FM and Lopez's models with the experimental data for all five mixes at the *w*=1.5 mm

Mix	Exp.	Amin-SM (2015)		Amin-FM (2015)		Lopez et al. (2016)	
	σ_t (MPa) -A-	σ_t (MPa) -B-	B/A	σ_t (MPa) -C-	C/A	σ_t (MPa) -D-	D/A
M1-S2	3.75	4.73	1.26	4.80	1.28	3.48	0.93
M2-3S	1.06	5.14	4.84	4.90	4.61	3.09	2.91
M3-1DEH	1.06	2.71	2.56	2.66	2.51	3.25	3.07
M4-2EH/S2	3.85	4.31	1.12	4.25	1.10	3.16	0.82
M5-2EH/S	3.43	5.44	1.59	5.63	1.64	5.96	1.74
Mean			2.27		2.23		1.89
COV			0.68		0.65		0.56
Standard deviation			1.54		1.44		1.06

Table 5.6 Comparisons of the Amin-SM, Amin-FM and Lopez's models with the experimental data for all five mixes at the *w*=2.5 mm

Mix	Exp.	Amin-SM (2015)		Amin-FM (2015)		Lopez et al. (2016)	
	σ_t (MPa) -A-	σ_t (MPa) -B-	B/A	σ_t (MPa) -C-	C/A	σ_t (MPa) -D-	D/A
M1-S2	2.24	2.65	1.18	2.85	1.27	1.97	0.88
M2-3S	0.59	1.45	2.44	2.65	4.47	1.10	1.85
M3-1DEH	0.37	2.14	5.81	2.08	5.67	2.17	5.91
M4-2EH/S2	3.05	1.68	0.55	2.35	0.77	2.01	0.66
M5-2EH/S	3.02	3.49	1.16	3.30	1.09	3.56	1.18
Mean			2.23		2.65		2.10
COV			0.95		0.85		1.04
Standard deviation			2.12		2.25		2.18

In general, direct tension and prism bending tests results show a good agreement in performance with each other except for mix M2-3S, and M3-1DEH. Furthermore, according to slightly modified French Association for Civil Engineering recommendations on Ultra-High Performance Fibre-Reinforced Concrete [12] mixes M2-3S, and M3-1DEH do not satisfy criteria for UHPFRCC. The only modification is related to the minimum volumetric fiber content equal or larger than 2% while modified French Association for Civil Engineering recommendations on

Ultra-High Performance Fibre-Reinforced Concrete [12] require strictly larger than 2%. Specifically mix M3-1DEH fails to meet the recommendations due to a too low volumetric fiber content and mix M2-3S fails due to a too low uniaxial tensile strength. Consequently, these two mixes are removed from further analysis. Therefore, Table 5.7, Table 5.8, and Table 5.9 compare experimentally obtained uniaxial tensile stresses with the predicted stresses at the crack opening displacement of 0.5 mm, 1.5 mm, and 2.5 mm, respectively. In this case, the values of the mean and the coefficient of the variation of the predicted to experimental values ratio show improved values.

In the case of Amin's full model, at w = 0.5 mm the mean of the predicted to experimental values ratios is 1.20 with COV of 0.13. At w = 1.5 mm the mean of the predicted to experimental values ratios is 1.34 with a COV = 0.21. Furthermore, at w=2.5 mm values of the mean of the predicted to experimental values ratios, and COVs are 1.04 and 0.24 respectively.

Furthermore, in the case of the simplified version of Amin's model, at w = 0.5 mm the mean of the predicted to experimental values ratios is 1.32 with a COV of 0.21. At w = 1.5 mm the mean of the predicted to experimental values ratios is 1.32 with a COV = 0.18. At w=2.5 mm values of the mean of the predicted to experimental ratios, and COVs are 0.96 and 0.37 respectively.

Lastly, when Lopez's model was applied, at w = 0.5 mm the mean of the predicted to experimental values ratios is 1.43 with a COV of 0.18. At w = 1.5 mm the mean of the predicted to experimental values ratios is 1.16 with a COV = 0.43. At w=2.5 mm values of the mean of the predicted to experimental values ratios, and COVs are 0.91 and 0.29 respectively.

Table 5.7 Comparisons of the Amin-SM, Amin-FM and Lopez's models with the experimental data, disregarding the mixes M2-3S, and M3-1DEH, at the *w*=0.5 mm

Mix	Exp.	Amin-SM (2015)		Amin-FM (2015)		Lopez et al. (2016)	
	σ_t (MPa) -A-	σ_t (MPa) -B-	B/A	σ_t (MPa) -C-	C/A	σ_t (MPa) -D-	D/A
M1-S2	4.98	6.81	1.37	6.18	1.24	7.23	1.45
M4-2EH/S2	6.29	6.94	1.10	6.50	1.03	7.31	1.16
M5-2EH/S	4.99	7.39	1.48	6.63	1.33	8.35	1.67
Mean			1.32		1.20		1.43
COV			0.15		0.13		0.18
Standard deviation			0.19		0.15		0.26

Table 5.8 Comparisons of the Amin-SM, Amin-FM and Lopez's models with the experimental data, disregarding the mixes M2-3S, and M3-1DEH, at the *w*=1.5 mm

Mix	Exp.	Amin-SM (2015)		Amin-FM (2015)		Lopez et al. (2016)	
	σ_t (MPa) -A-	σ_t (MPa) -B-	B/A	σ_t (MPa) -C-	C/A	σ_t (MPa) -D-	D/A
M1-S2	3.75	4.73	1.26	4.80	1.28	3.48	0.93
M4-2EH/S2	3.85	4.31	1.12	4.25	1.10	3.16	0.82
M5-2EH/S	3.43	5.44	1.59	5.63	1.64	5.96	1.74
Mean			1.32		1.34		1.16
COV			0.18		0.21		0.43
Standard deviation			0.24		0.28		0.50

Table 5.9 Comparisons of the Amin-SM, Amin-FM and Lopez's models with the experimental data, disregarding the mixes M2-3S, and M3-1DEH, at the *w*=2.5 mm

Mix	Exp.	Amin-SM (2015)		Amin-FM (2015)		Lopez et al. (2016)	
	σ_t (MPa) -A-	σ_t (MPa) -B-	B/A	σ_t (MPa) -C-	C/A	σ_t (MPa) -D-	D/A
M1-S2	2.24	2.65	1.18	2.85	1.27	1.97	0.88
M4-2EH/S2	3.05	1.68	0.55	2.35	0.77	2.01	0.66
M5-2EH/S	3.02	3.49	1.16	3.30	1.09	3.56	1.18
Mean			0.96		1.04		0.91
COV			0.37		0.24		0.29
Standard deviation			0.36		0.25		0.26

Figure 5.10 compares predictions of Amin-SM, and Lopez's models with experimental data. These specific models are selected because they are both intended for design purposes. It can be seen that both models coincide with the experimental data very well, whereby the Amin-SM has a slightly better performance overall. Moreover, it is noted that neither of Amin's models are restricted to UHPFRCC only. On the other hand, Lopez's model can capture a complete tensile behavior, including a strain-hardening phase. Amin's models on the other hand are intended only for the softening behavior or stress-crack opening displacement response.

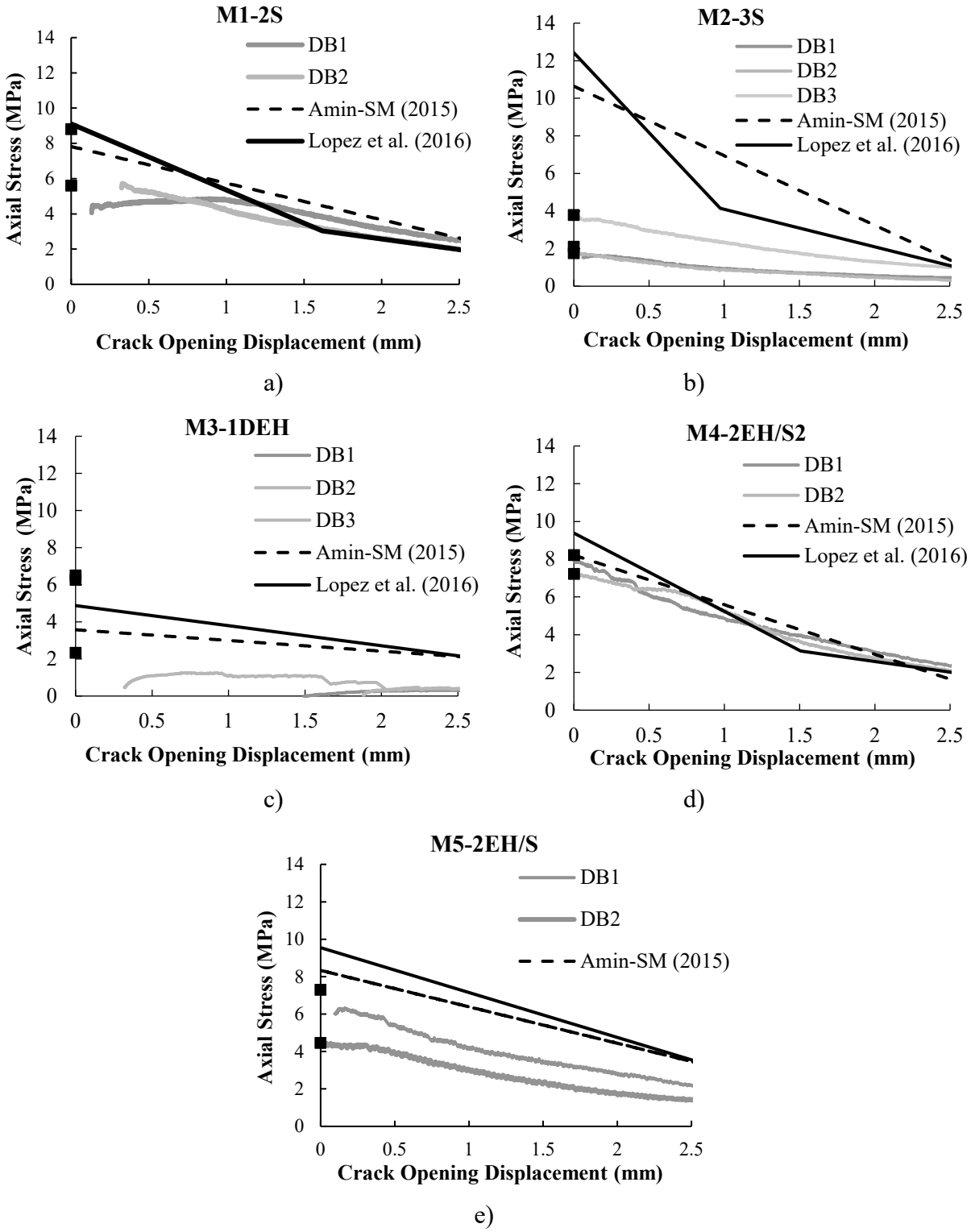

Figure 5.10 Comparison of two design models (Amin-SM and Lopez's) with the experimental data from uniaxial tests: a) M1-S2, b) M2-3S, c) M3-1DEH, d) M4-2EH/S2, and e) M5-2EH/S

Chapter 6 - Summary, conclusions, and future research

6.1. Summary and conclusions

Fiber reinforced cementitious composites are advanced materials that offer new opportunities for civil infrastructure preservation and future development. Nonetheless, a lack of research and industry confidence has resulted in a slow uptake and application of these resilient and sustainable materials in elements other than non-critical members. Thus, the main motivation for this research was to provide more detailed evaluation of fiber effects on the full-fledged response of these materials including the inception of strain localization in HPFRCC as well as the complete tensile behavior of UHPFRCC.

In Chapter 3 the diagnostic strain localization analysis was performed in order to quantify effects of fibers on failure precursors in HPFRCC. To this end, a combined numerical/analytical model that can capture a stress-strain response prior to a macro crack localization was developed and implemented. Although the experimental data were available for four different volumetric fiber contents (0%, 1%, 1.5%, and 2%), the data for only three fiber contents (0%, 1%, and 2%) were used during calibration of the selected constitutive models. Predictions of a homogeneous stress-strain response were successfully validated against the experimental data for HPFRCC.

Furthermore, the strain localization diagnostics provided quantitative assessments of the effects of fibers on the OSL, and orientation and mode of the accompanying deformation bands. Results showed that presence of fibers delayed the onset of strain localization in all uniaxial tests. In particular, the inception of strain localization coincided closely with the onset of yielding in the plain and reinforced cementitious composites in UT tests. Nevertheless, the onset of yielding in HPFRCC was delayed as compared to that in the plain mortar. In UC tests, the

predicted OSL in the plain mortar and HPFRCCs coincided closely with peak stresses, which were increased by about 25% in HPFRCCs compared to the plain mortar.

While ductility and peak stresses increased in all tests on HPFRCC, mechanisms through which fibers affected the stress-strain responses in plane stress UT and UC tests differed. Results of the diagnostic strain localization analysis indicate that a significant increase in ductility was achieved in UT tests on HPFRCC as compared to a non-reinforced cementitious composite. Furthermore, the analysis indicates that this was most likely accomplished through a distributed cracking that delayed a macro crack localization and increased the peak load, which is in agreement with experimental findings. In UC tests, increased toughness was achieved through a delayed OSL and more significant strain hardening. Therefore, addition of fibers affected the compressive stress-strain response similarly to an increase in a confining pressure.

Results also showed that an increase in the volumetric fiber content made deformation bands in UC tests flatter and more contractant while fibers affected neither the critical localization angle nor the mode of deformation bands in the UT tests. Thus, deformation bands remained perpendicular to the principal stress direction in UT tests. Furthermore, they were all pure dilation bands, thus resembling the crack mode I in fracture mechanics.

In Chapter 4 the experimental program was devised and performed to characterize primarily the post cracking characteristics of UHPFRCC. The experiments were carried out on five different mixes whereby water to binder ratio, type of fibers, and volumetric fiber content were the testing variables. The purpose of the material characterization was determination of compressive and tensile properties of UHPFRCC through tests performed in this study.. Experiments conducted on the UHPFRCC specimens include uniaxial compression tests, direct tension tests, and indirect four-point prism bending tests.

It was found from uniaxial compression tests that increase in the volumetric fiber content slightly increased the compressive strength of the specimens. Specifically, the compressive strengths varied between 143 and 177 MPa, while the value of the Young's modulus was consistent, around 44 GPa.

Tensile test methods gave an indication of the tensile cracking strength of UHPFRCC. A direct tension test provided realistic and more detailed information about the UHPFRCC behavior under a tensile load. The direct tension tests were performed on the specially designed dog-bone specimens. The FE analyses were conducted during the specimen design process to evaluate the effects of different specimen geometries and loading arrangements on the uniformity of a tensile stress field over a large area that should be unaffected by the loading arrangement and specimen shape. After taking into account all recommendations, prerequisites and FE results, the elongated dog-bone specimen with the overall length of 700 mm, width of 75 mm, and the mid prismatic part of the specimen that increased gradually to 150 mm at the end of the transition spline was selected. The values of the Young's moduli obtained from direct tension tests on UHPFRCC ranged between 37.6 and 55.1 GPa depending on the volumetric fiber content and fiber type. These values are somewhat higher or lower than those obtained from uniaxial compression tests depending on the mix tested. The tensile cracking stress of UHPFRCC ranged between approximately 5 to 9 MPa. Two different post-cracking behaviors were observed in direct tension tests, softening and strain hardening accompanied with multiple cracking.

On the other hand, results from the prism bending tests were less scattered than the ones obtained from direct tension tests. Specifically, the results indicate that flexural strength depends strongly on the volumetric fiber content and water to binder ratio. More precisely, higher values

of the material toughness, first crack, peak, and residual loads are obtained for higher volumetric fiber contents. Moreover, the mix M4-2EH/S2 had the highest water to binder ratio (w/c=0.19), thus causing the ASTM strength results to be lower than for the other mixes having equal volumetric fiber contents but less water added to the mix.

In Chapter 5, modeling of the post-cracking response of UHPFRCC in UT was conducted in order to determine whether a prism bending test could be used as an alternative to a standard direct test. To this end, the three most recent inverse analysis models were used: 1) Amin's full model, 2) Amin's simplified model, and 3) Lopez's model. Reported values of COVs indicate that the corresponding predictions correlate well with the experimental data from the uniaxial tension tests. This indicates that the inverse problem solutions of four-point prism bending tests could be used as a viable alternative to uniaxial testing when determining the post-cracking σ-w relationship of UHPFRCC. This is very helpful for practitioners, and to all of those who need to conduct on-site quality control in a construction project. On the other hand, a direct tension test is still the most appropriate characterization method for researchers and material engineers, especially when more detailed investigations of material behavior of UHPFRCC is needed.

In summary, there is no single material solution to all current and future infrastructure problems, but advanced materials can help. Specifically, UHPFRC has a strong potential to help the revitalization of infrastructure, and in the building of new infrastructure that is sustainable, resilient and long-lasting. However, adoption of UHPFRC in the U.S. has been slow in comparison to Europe and Asia, notably Australia, China, France, Germany, Iran, and Japan. This dissertation is a contribution to a concerted effort that is required to accelerate the usage of HPFRCC and UHPFRCC in the U.S. construction industry.

6.2. Recommendations for the future research

There is a strong need to establish a consensus in regard to test specimens and material characterization methods to be applied in conjunction with material level physical testing of FRCCs. The direct tension test results on the newly designed dog-bone specimens showed very good results in that they developed multiple cracking in the mid-section of the specimens without any cracks being observed close to gripping sections. However, experimental results that would include a larger variety of different mixes are needed for a more complete validation of the inverse analysis models presented herein. Moreover, Amin's models are based on the assumption of development of a single major crack in prism bending tests. This may not cover all scenarios, especially not those exhibiting a pronounced deflection hardening during which multiple cracking may take place. Should the additional testing exhibit this type of behavior Amin's models would likely require further modifications.

In order to develop a more complete and improved plasticity models for HPFRCC and especially UHPFRCC, it would be necessary to devise and conduct a complete experimental characterization of HPFRCC and UHPFRCC. The testing program should include a series of triaxial compression tests at different confining stress levels, UC, UT, and prism bending tests. In addition, to evaluate effects of fiber distribution and fiber orientation it is highly recommended that X-ray imaging be an integral part of the experimental program.

A full-fledged experimental program described above would enable a more thorough material characterization, based on which new design methods and physics based regularized computational models for HPFRCC and UHPFRCC could be developed, thus advancing the use of HPFRCC and UHPFRCC in the engineering practice.

References

[1] A. E. Naaman, "Tensile strain-hardening FRC composites: Historical evolution since the 1960," in *Advances in Construction Materials 2007*, Berlin, Springer Berlin Heidelberg, 2007, pp. 181-202.

[2] S. Qian and V. C. Li, "Simplified Inverse Method for Determining the Tesile Properties of SHCCs," *Journal of Advanced Concrete Technology,* vol. 6, no. 2, pp. 353-363, 2008.

[3] A. E. Namaan and H. W. Reinhardt, "Chapter 3," in *High Performance Fiber Reinforced Cement Composites 2*, London, E. & F.N. Spon., 1995, pp. 232-269.

[4] R. F. Zollo, "Fiber-reinforced concrete: an overview after 30 years of development," *Cement and Concrete Composites,* vol. 19, no. 2, pp. 107-122, 1997.

[5] Y. Voo and S. Foster, Reactive Powder Concrete: Analysis and Design of RPC Girders, LAP Lambert Academic Publishing, 2010.

[6] V. C. Li, "From Micromechanics to Structural Engineering – The Design of Cementitious Composites for Civil Engineering Applications," *Journal of Structural Mechanics and Earthquake Engineering,* vol. 10, no. 2, 1993.

[7] J. A. Lopez, P. Serna, J. Navarro-Gregori and H. Coll, "A simplified five-point inverse analysis method to determine the tensile properties of UHPFRC from unnontched four-point bending test," *Composited Part B,* vol. 8, no. 91, pp. 189-204, 2016.

[8] A. C496/C496M, "Standard Test Method for Splitting Tensile Strength of Cylindrical Concrete Specimens," ASTM International, West Conshohocken, PA, 2004.

[9] R. T. 1.-T. 2003., "Test and design methods for steel fibre reinforced concrete: final recommendations, σ-ε design method.," *Materials and Structures,* vol. 36, pp. 560-567, 2003.

[10] A. C. I. (. C. 544, "Report on fiber reinforced concrete ACI 544.1R-96," American Concrete Institute, Detroit, 1996.

[11] J. S. o. C. E. (JSCE), "Recommendations for design and construction of high performance fiber reinforced cement composites with multiple fine cracks (HPFRCC)," 2008.

[12] A. F. d. G. Civil, "Bétons fibrés à ultra-hautes performances – ultra high performance fibre-reinforced concretes, recommandations provisoires – Interim

recommendations," Association Francaise de Genie Civil Service d'etudes techniques des routes et autoroutes, 2002.

[13] M. Saafi, H. A. Toutanji and Z. Li, "Behavior of concrete columns confined with fiber reinforced polymer tubes," *ACI Materials Journal,* vol. 96, no. 4, pp. 500-509, 1999.

[14] P. N. Balaguru and S. P. S.P. Shah., Fiber reinfroced cement composites, New York: McGraw- Hill, 1992.

[15] F. Shirmohammadi, A. Esmaeily and Z. Kiaeipour, "Stress-Strain Model for Circular Concrete Column Confined by FRP and Conventional Lateral Steel," *Engineering Structures,* vol. 84, pp. 395-405, 2015.

[16] F. Shirmohammadi, Effect of load pattern and history on performance of reinforced concrete columns, PhD thesis, Kanas State Univeristy, Manhattan, KS, USA, 2015.

[17] A. Amin, S. Foster and M. Watts, "Modelling the tension stiffening effect in SFR-RC," *Magazine of Concrete Research,* vol. 68, no. 7, pp. 339-352, 2016.

[18] A. Amin and S. Foster, "Shear strength of steel fibre reinforced concrete beams with stirrups," *Engineering Structures,* vol. 111, pp. 323-332, 2016.

[19] J. Romualdi and G. Batson, "Behaviour of reinforced concrete beams with closely spaced reinforcemen," *ACI Journal Proceedings,* vol. 60, no. 6, pp. 775-789, 1963.

[20] J. P. Romualdi and J. A. Mandel, "Tensile Strength of Concrete Affected by Uniformly Distributed and Closely Spaced Short Lengths of Wire Reinforcement," *ACI Journal Proceedings,* vol. 61, no. 6, pp. 657-671, 1964.

[21] V. Ramakrishnan, T. Brandshaug, W. V. W.V. Coyle and E. K. Schrader, "A Comparative Evaluation of Concrete Reinforced with Straight Steel Fibers and Deformed End Fibers Glued Together into Bundles," *ACI Journal Proceedings,* vol. 77, no. 3, p. 135–143, 1980.

[22] H. H. Bache, "Densified Cement/Ultra-Fine Particle-Based Materials," in *2nd International Conference on Superplasticizers in Concrete*, 1981.

[23] P. Richard and M. Cheyrezy, "Composition of reactive powder concretes," *Cement and Concrete Research,* vol. 25, no. 7, pp. 1501-1511, 1995.

[24] I. Markovic, J. C. Walraven and J. G. M. van Mie, "Development of Performance Hybrid Fibre Concrete," in *4th International RILEM Workshop on High Performance Fiber Reinforced Cement Composites (HPFRCC4)*, 2003.

[25] R. Barnard, Mechanical Properties of Flyash/Slag Based Geopolymer Concrete with the addition of Macro fibres, M.Eng. Thesis, Stellenbosch University, Stellenbosch, South Africa, 2014.

[26] A. E. Naaman, "Engineered Steel Fibers with Optimal Properties for Reinforcement of Cement Composites," *Journal of Advanced Concrete Technology,* vol. 1, no. 3, p. 241–252, 2003.

[27] A. P. Fantili, H. Mihashi and T. Nishiwaki, "Tailoring hybrid strain-hardening cementitious composites," *ACI Materials Journal ,* vol. 111, no. 2, pp. 211-218, 2014.

[28] L. Betterman, C. C. Ouyang and S. P. Shah, "Fiber-Matrix Interaction in Microfiber-Reinforced Mortar," *Advanced Cement Based Materials,* vol. 2, no. 2, pp. 53-61, 1995.

[29] K. Wille, D. J. Kim and A. E. Naaman, "Strain-hardening UHP-FRC with low fiber contents," *Materials and Structures,* vol. 44, no. 3, p. 583–598, 2011.

[30] M. di Prisco, G. Plizzari and L. Vandewalle, "Fibre reinforced concrete: new design perspectives," *Materials and Structures,* vol. 42, pp. 1261-1281, 2009.

[31] A. Spasojevic, "Structural Implications of Ultra-High Performance Fibre-Reinforced Concrete in Bridge Design," Ph.D. Dissertation, École Polytechnique Fédérale De Lausanne, Lausanne, Switzerland, 2008.

[32] A. Amin, Postcracking behaviour if steel fibre reinforced concrete: from material to sturcture, Ph.D. Thesis, University of New South Wales, Sydney, Australia, 2015.

[33] K. Wille, S. El-Tawil and A. Naaman, "Properties of strain hardening ultra high performance fiber reinforced concrete (UHP-FRC) under direct tensile loading," *Cement & Concrete Composites,* pp. 53-66, 2014.

[34] J. Yin, S. Zhou, Y. Xie, Y. Chen and Q. Yan, "Investigation on compounding and application of C80–C100 high-performance concrete," *Cement and Concrete Research,* vol. 32, no. 2, pp. 173-177, 2002.

[35] B. A. Graybeal, "Material Property Characterization of Ultra-High Performance Concrete," 2006.

[36] A. Naaman and H. W. Reinhardt, "Proposed Classificationof HPFRC Composites Based on their Tensile Response," in *Proceedings of a Symposium honoring S. Mindess*, University of British Columbia, 2005.

[37] Z. Jiang and N. Banthia, "Size Effects in Flexural Toughness of Fiber Reinforced Concrete," *Journal of Testing and Evaluation,* vol. 38, no. 3, pp. 1-7, 2009.

[38] J. Dugat, N. Roux and B. J., "Mechanical properties of reactive powder concrete," *Materials and Structures,* vol. 29, no. 4, p. 233–240, 1996.

[39] T. Vande Voort, M. Suleiman and S. Sritharan, "Design and Performance Verification of UHPC Piles for Deep Foundations," Center for Transportation Research and Education, Iowa State Univeristy, Ames, IA, 2008.

[40] G. J. Parra-Montesinos, "High-Performance Fiber-Reinforced Cement Composites: An Alternative for Seismic Design of Structures," *ACI Structural Journal,* vol. 102, no. 5, p. 668–675, 2005.

[41] B. A. Canbolat, G. Parra-Montesinos and J. K. Wight, "Behavior of Precast High-Performance Fiber Reinforced Cement Composite Coupling Beams Under Large Displacement Reversals," in *Proceedings of the 13th world conference on earthquake engineering*, Vancouver, B.C., Canada, 2004.

[42] B. Canbolat, G. J. Parra-Montesinos and J. K. Wight, "Experimental Study on Seismic Behavior of High-Performance Fiber-Reinforced Cement Composite Coupling Beams," *ACI Structural Journal ,* vol. 102, no. 1, pp. 159-166, 2005.

[43] G. J. Parra-Montesinos and K. Kim, "Seismic Behavior of Low-Rise Walls Constructed With Strain-Hardening Fiber Reinforced Cement Composites," in *Proceedings of the 13th world conference on earthquake engineering*, Vancouver, B.C., Canada, 2004.

[44] G. Parra-Montesinos, S. Peterfreund and S. H. Chao, "Highly Damage-Tolerant Beam–Column Joints Through Use of High-Performance Fiber-Reinforced Cement Composites," *ACI Strctural Journal,* vol. 102, no. 3, pp. 487-497, 2005.

[45] G. J. Parra-Montesinos and P. Chompreda., "Deformation Capacity and Shear Strength of Fiber-Reinforced Cement Composite Flexural Members Subjected to Displacement Reversals," *Journal of Structural Engineering,* vol. 133, no. 3, p. 421–431, 2007.

[46] S. H. Chao, A. E. Naaman and P.-M. G. J., "Bond Behavior of Reinforcing Bars in Tensile Strain-Hardening Fiber-Reinforced Cement Composites," *ACI Structural Journal,* vol. 106, no. 6, p. 897–906, 2009.

[47] H. H. Bache, "Densified Cement/Ultra-Fine Particle-Based Materials," in *2nd International Conference on Superplasticizers in Concrete*, 1981.

[48] H. H. Bache, "The New Strong Cements: Their Use in Structures," *Physics in Technology,* vol. 19, pp. 43-50, 1988.

[49] H. H. Bache, "Concrete and Concrete Technology in a Broad Perspective," in *Nordic Symposium on Modern Design of Concrete Structures*, Aalborg Univeristy, Denmark, 1995.

[50] P. Rossi, "Ultra High Performance Fibre Reinforced Concrete (UHPFRC): An overview," in *5th RILEM Symposium on Fibre-Reinfroced Concrete (FRC)*, Lypon, France, 2000.

[51] P. Rossi, "Development of new cement composite materials for construction," *Journal of Materials: Design and Applications,* vol. 219, no. 1, pp. 67-74, 2005.

[52] M. M. V. Cheyrezy and L. Frouin, "Microstructural Analysis of RPC (Reactive Powder Concrete)," *Cement and Concrete Reasearch,* vol. 25, no. 7, p. 1491–1500, 1995.

[53] N. Roux, C. Andrade and M. A. Sanjuan, "Experimental Study of Durability of Reactive Powder Concretes," *Journal of Materials in Civil Engineering,* vol. 8, no. 1, pp. 1-6, 1996.

[54] P. Acker and M. Behloul, "Ductal Technology: a Large Spectrum Of Properties, a Wide Range of Applications," in *Proceedings of International Symposium on UHPC*, 2004.

[55] P. Aıtcin, M. Lachemi, R. Adeline and P. Richard, "The Sherbrooke Reactive Powder Concrete Footbridge," *Structural Engineering International,* vol. 8, no. 2, pp. 140-144, 1998.

[56] H. G. Russell and B. A. Graybeal, "Ultra-High Performance Concrete: A State-of-the-Art Report for the Bridge Community," U.S. Departement of Transportation, Federal Highway Administration, 2013.

[57] A. Malik and S. Foster, "Behaviour of Reactive Powder Concrete Columns without Steel Ties," *Journal of Advanced Concrete Technology,* vol. 6, no. 2, p. 377–386, 2008.

[58] M. Soutsos, S. Millard and K. Karaiskos, "Mix Design, Mechanical Properties, and Impact Resistance of Reactive Powder Concrete (RPC).," in *International RILEM Workshop on High Performance Fiber Reinforced Cementitious Composites (HPFRCC) in Structural Applications*, Honolulu, Hawaii, USA, 2005.

[59] A. Astarlioglu, T. Krauthammer and C. Felice, "State-of-the-Art Report on Fiber Reinforced Ultra-High Performance Concrete," Report CIPPS-TR-003-2010, University of Florida, Gainesville, FL, 2010.

[60] S. Piotrowski and M. Schmidt, "Life Cycle Cost Analysis of a UHPC-Bridge on Example of Two Bridge Refurbishment Designs," in *Proceedings of Hipermat 2012 3rd International Symposium on UHPC and Nanotechnology for High Performance Construction Materials*, Kassel, Germany, 2012.

[61] K. Sirijaroonchai, A macro-scale plasticity model for high performance fiber reinforced cement composites, Ph.D. Dissertation, The University of Michigan, Ann Harbour, USA, 2009.

[62] H. Stang, Z. Li and S. P. Shah, "Pullout Problem Stress versus Fracture Mechanic Approach," *Journal of Engineering Mechanics,* vol. 116, no. 10, pp. 2136-2150, 1990.

[63] C. K. Y. Leung and P. Y. Geng, "Micromechanical modeling of softening behavior in steel fiber reinforced cementitious composites," *International Journal of Solids and Structures,* vol. 35, pp. 4205-4222, 1998.

[64] J. Alwan, A. Naaman and W. Hansen, "Pull-out Work of Steel Fibers from Cementitious Composites: Analytical Investigation," *Cement and Concrete Composites,* vol. 13, no. 4, pp. 247-255, 1991.

[65] C. Sujivorakul, Development of High Performance Fiber Reinforced Cement Composites using Twisted Polygonal Steel Fibers, Ph.D. Dissertation, University of Michigan, Ann Harbour, USA, 2002.

[66] J. E. J. Bolander and S. Saito, "Discrete Modeling of Short-fiber Reinforcement in Cementitious Composites," *Advanced Cement Based Materials,* vol. 6, no. 3-4, pp. 76-86, 1997.

[67] J. van Mier, Concrete fracture: a multiscale approach, Boca Raton, Florida: CRC Press, 2013, p. 448.

[68] H. Stang and J. F. Olesen, "On the interpretation of bending tests on FRCmaterials," *Fracture Mechanics of Concrete Structures,* vol. 1, pp. 511-520, 1998.

[69] M. Jirasek and B. Patzak, "Models for Quasibrittle Failure: Theoretical and Computational Aspects," in *European Conference on Computational Mechanics*, Cracow, Poland, 2001.

[70] A. C. T. Chen and W. F. Chen, "Constitutive Relations for Concrete," *Journal of Engineering Mechanics Division,* vol. 101, no. 4, pp. 465-481, 1975.

[71] T. Y. Chang, H. Taniguchi and W. F. Chen, "Nonlinear Finite Element Analysis of Reinforced Concrete Panels," *Journal of Structural Engineering,* vol. 113, no. 1, pp. 122-140, 1987.

[72] P. Lade, "Three-parameter Failure Criterion for Concrete," *Journal of the Engineering Mechanics Division,* vol. 108, pp. 850-863, 1982.

[73] P. Grassl, "Modelling of dilatation of concrete and its effect in triaxial compression," *Finite Elements in Analysis and Design,* vol. 40, no. 9-10, pp. 1021-1033, 2004.

[74] S. S. Hsieh, E. C. Ting and W. F. Chen, "Elastic-Fracture Model for Concrete," in *Proceeding ASCE Engineering Mechanics Division Specification Conference*, Austin, TX, USA, 1979.

[75] F. Barzegar and S. Maddipudi, "Three-dimensional modeling of concrete structures I: Plain concrete," *Journal of Structural Engineering,* vol. 123, no. 10, pp. 1339-1346, 1997.

[76] P. Pivonka, R. Lacknew and H. A. Mang, "Concrete Subjected to Triaxial Stress States: Application to Pull-Out Analyses," *Journal of Engineering Mechanics,* vol. 130, no. 12, pp. 1486-1498, 2004.

[77] S. S. Smith, K. J. William, K. H. Gerstle and S. Sture, "Concrete over the Top, or: Is There Life After Peak?," *ACI Material Journal,* vol. 86, no. 5, pp. 491-497, 1989.

[78] I. Imran and S. J. Pantazopoulou, "Plasticity Model for Concrete under Triaxial Compressions," *Journal of Engineering Mechanics,,* vol. 127, no. 3, pp. 281-290, 2001.

[79] R. Hill, The Mathematical Theory of Plasticity, Oxford,: Clarendon Press, 1950.

[80] W. Prager, "A new method of analyzing stresses and strains in work hardening plastic solids," *Journal of Applied Mechanics,* vol. 23, pp. 493-496, 1956.

[81] P. Hodge, "A new method of analyzing stresses and strains in work hardening plastic solids," *Journal of Applied Mechanics,* vol. 24, p. 482–483, 1957.

[82] S. Pietruszczak and G. Xu, "Brittle response of concrete as a localization problem," *International Journal of Solids Structures,* vol. 32, no. 11, pp. 1517-1533, 1995.

[83] M. R. Salari, S. Saeb, K. J. Willam, J. S.Patchet and R. Carrasco, "A coupled elastoplastic damage model for geomaterials," *Computer Methods in Applied Mechanics and Engineering,* vol. 193, pp. 2652-2643, 2004.

[84] S. Beizaee, "Constitutive modeling and numerical implementation of brittle and ductile material behavior with the aid of inelastic XFEM and damage-plasticity models," PhD thesis, University of Houston, Houston, 2013.

[85] F. Baby, B. Graybeal, P. Marchand and F. Toutlemonde, "Proposed flexural test method and associated inverse analysis for Ultra High Performance Fiber Reinforced Concrete," *ACI Materials Journal,* vol. 109, no. 5, pp. 545-556, 2012.

[86] A. Hillerborg, "Analysis of fracture by means of the fictitious crack model, particularly for fibre reinforced concrete," *International Journal of Cement Composites,* vol. 2, pp. 177-184, 1980.

[87] J. van Mier, Fracture Processes of Concrete. Assessment of Material Parameters for Fracture Models, Boca Raton, FL: CRC Press, 1997, p. 446.

[88] A. Kooiman, "Modelling steel fibre reinforced concrete for structural design.," PhD Dissertation, Delft University of Technology, Delft, Netherlands, 2000.

[89] J. van Mier and M. van Vliet, "Uniaxial tension test for the determination of fracture parameters of concrete: state of the art," *Engineering Fracture Mechanics,* vol. 69, pp. 235-247, 2002.

[90] I. Markovic, "High-performance hybrid-fibre concrete: development and utilisation," PhD Dissertation. Delft University of Technology, The Netherlands, Delft, Netherlands, 2006.

[91] M. R. A. van Vliet, Size Effect in Tensile Fracture of Concrete and Rock, Ph.D. Thesis, Delft University of Technology, Delft, Netherlands, 2000.

[92] A. E. Naaman and J. R. Homrich, "Tensile stress-strain properties of SIFCON," *ACI Materials Journal,* vol. 86, pp. 244-251, 1989.

[93] J. G. Rots and R. de Borst, "Analysis of concrete fracture in 'direct' tension," *International Journal of Solids and Structures,* vol. 25, no. 12, pp. 1381-1394, 1989.

[94] D. AS5100.5., "Draft for public comment: Australian standars, bridge design part 5: concrete. Standards Australia," 2014.

[95] S. P. Shah, J. I. Daniel, S. H. Ahmad, M. Arockiasamy, P. N. Balaguru, C. G. Ball, H. P. J. Ball, G. B. Batson, A. Bentur, R. J. Craig, M. E. Criswell, S. Freedman, R. E. Galer, M. A. Galinat, V. S. Gopalaratnam and A. J. Guerra, "Measurement of

properties of fibre reinforced concrete," *ACI Materials Journal,* vol. 85, no. 6, pp. 583-593, 1988.

[96] M. di Prisco, M. Colombo and D. Dozio, "Fibre-reinforced concrete in fib Model Code 2010: principles, models and test validation," *Structural Concrete,* vol. 14, pp. 342-361, 2013`14.

[97] I. Markovic, j. Waleaven and J. G. M. van Mier, "Tensile behaviour of high performance hybrid fibre concrete," in *Proceedingd of the 5th International Conference on Fracture of Concrete and Concrete Structures (FraMCoS-V)*, Vail, 2004.

[98] Y. Uchida, N. Kurihara, K. Rokugo and W. Koyanagi, "Determination of tension softening diagrams of various kinds of concrete by means of numerical analysis," in *Proceedings of the 2nd International Conference on Fracture Mechanics Concrete and Concrete Structures (FraMCoS-2)*, Zurich, 1995.

[99] A. Hillerborg, M. Modeer and P. E. Petersson, "Analysis of crack formation and crack growth in concrete by means of fracture mechanics ad finite elements," *Cement and Concrete Research,* vol. 6, no. 6, pp. 773-778, 1976.

[100] F. Laranjeira, "Design-oriented constitutive model for steel fiber reinforced concrete," PhD Thesis, Universitat Politècnica de Catalunya, Barcelona, 2010.

[101] H. L. V. C. Stang, "Classification of fibre reinfroced cementitious mateirals for structural applications," in *Proceedings of 6th RILEM Symposium on Fiber-Reinfroced Concrete* , Varenna, Italy, 2004.

[102] D. 2012., "Richtlinie Stahlfaserbeton (Directive for SFRC)," Deutscher Ausschuss fur Stahlbeton, Germany, 2012.

[103] N. 3. 2006., " Concrete structures standard," Standards New Zealand, 2006.

[104] M. Miletić and D. Perić, "Onset of Strain Localization in Fiber Reinforced Composites Subjected to Plane Stress Loading," in *Bifurcation and Degradation of Geomaterials in the New Millennium, Proceedings of the 10th International Workshop on Bifurcation and Degradation in Geomaterials*, Hong Kong, 2015.

[105] M. Miletić and D. Perić, "Strain Loclization Analysis of an Elastic-Plastic Model for High Performance Fiber Reinforced Cementitious Composites," in *Proceedings of the 9th International Conference on Fracture Mechanics of Concrete and Concrete Structures (FraMCoS-9)*, Berkeley, CA, 2016.

[106] J. W. Rudnicki and J. R. Rice, "Conditions for the localization of deformation in pressure-sensitive dilatant materials," *Journal of the Mechanics and Physics of Solids,* vol. 23, pp. 371-394, 1975.

[107] K. Runesson, N. S. Ottosen and D. Perić, "Discontinuous bifurcations of elastic-plastic solutions at plane stress and plane strain," *International Journal of Plasticity,* vol. 7, pp. 99-121, 1991.

[108] ABAQUS, Version 6.13-1., Providence, RI: Dassault Systemes Simulia Corporation, 2013.

[109] W. Yin, E. Su, M. Mansour and T. Hsu, "Biaxial tests on plain and fiber concrete," *ACI Materials Journal,* vol. 86, no. 3, pp. 236-243, 1989.

[110] X. D. Hu, R. Day and P. Dux, "Biaxial failure model for fiber reinforced concrete," *Journal of Materials in Civil Engineering (ASCE),* vol. 15, no. 6, pp. 609-615, 2003.

[111] Y. Zhang, Study on uniaxial compressive constitutive relationship and uniaxial tensile behavior of steel-polypropylene hybrid fiber reinforced concrete, Wuhan, China: Ph.D. thesis, Wuhan University, 2010.

[112] Y. Chi, L. Xu and H. Yu, "Constitutive modeling of steel-polypropylene hybrid fiber reinforced concrete using a non-associated plasticity and its numerical implementation," *Composite Structures,* vol. 111, no. 5, pp. 497-509, 2014.

[113] AS1012.9, "Methods of Testing Concrete - Determination of the compressive strength of concrete specimens," Standards Australia, 1999.

[114] AS1012.17, "Methods of Testing Concrete - Determination of the static chord modulus of elasticity and Poisson's ratio of concrete specimens," Standards Australia, 1997.

[115] H. A. Moghadam and O. A. Khoshbin, "Effect of Water-Cement Ratio (w/c) on Mechanical Properties of Self-Compacting Concrete (Case Study)," *World Academy of Science, Engineering and Technology, International Journal of Civil, Environmental, Structural, Construction and Architectural Engineering,* vol. 6, no. 5, pp. 317-320, 2012.

[116] M. Schmidt, E. Fehling, T. Teichmann, K. Bunje and R. Bornemann, "Ultra-High Performance Concrete: Perspective for the Precast Concrete Industry," *Concrete Precasting Plant and Technology,* vol. 69, no. 3, pp. 16-29, 2003.

[117] O. Bonneau, M. Lachemi, E. Dallaire, J. Dugat and P. C. Aïtcin, "Mechanical Properties and Durability of Two Industrial Reactive Powder Concretes," *ACI Materials Journal,* vol. 94, no. 4, pp. 286-290, 1997.

[118] M. Reda, N. Shrive and J. E. Gillott, "Microstructural Investigation of Innovative UHPC," *Cement and Concrete Research,* vol. 29, no. 3, pp. 323-329, 1999.

[119] G. M. H. S. Herold, "Measurement of porosity of Ultra High Strength Fibre Reinforced Concrete," in *Proceedings of the International Symposium on Ultra-High Perofrmance Concrete*, Kassel, Germany, 2004.

[120] A. C. I. (ACI), "Report on High-Strength Concrete (ACI 363R-92)," ACI , Farmington Hills, Michigan, 1992.

[121] M. Kakizaki, H. Edahiro, T. Tochigi and T. Niki, "Effect of Mixing Method on Mechanical Properties and Pore Structure of Ultra High-Strength Concrete," in *Fly Ash, Silica Fume, Slag, and Natural Pozzolans in Concrete: Proceedings, Fourth International Conference*, Istanbul, Turkey, 1992.

[122] S. Sritharan, B. Bristow and V. Perry, "Characterizing an Ultra-High Performance Material for Bridge Applications under Extreme Loads," in *Proceedings of the 3rd International Symposium on High Performance Concrete*, Orlando, Florida, 2003.

[123] B. Graybeal, "Compressive behavior of ultra-high-performance fiber-reinforced concrete," *ACI Materials Journal,* vol. 104, no. 2, pp. 146-152, 2007.

[124] J. Ma, M. Orgass, F. Dehn, D. Schmidt and N. V. Tue, "Comparative Investigations on Ultra-High Performance Concrete with and without Coarse Aggregates," in *Proceedings of the International Symposium on Ultra-High Performance Concrete*, Kassel, Germany, 2004.

[125] B. A. Graybeal, "FHWA-HRT-06-103: Material Property Characterization of Ultra-High Performance Concrete," Federal Highway Administration, Fairfax, Virginia, USA, 2006.

[126] H. Neuber, "Der zugbeanspruchte flachstab mit optimalem querschnittsubergang," *Forschung im Ingenieurwesen,* vol. 35, no. 1, pp. 29-30, 1969.

[127] S. D. P. Benson and B. L. Karihaloo, "CARDIFRC - Development and mechanical properties. Part III: Uniaxial tensile response and other mechanical properties," *Magazine of Concrete Research,* vol. 57, no. 8, pp. 433-443, 2005.

[128] A. C1609/C1609M-12, "Standard Test Method for Flexural Performance of Fiber-Reinforced Concrete (Using Beam With Third-Point Loading)".

[129] B. Parmentier, L. Vandewalle and F. Van Rickstal, "Evaluation of the scatter of the postpeak behaviour of fibre reinforced concrete in bending: a step towards reliability," in *Proceedings of 7th RILEM International Symposium on Fibre Reinforced Concrete – Design and Applications*, Chennai, 2008.

[130] M. di Prisco, G. Plizzari and L. Vandewalle, "Fibre reinforced concrete: new design perspectives," *Materials and Structures,* vol. 42, no. 9, pp. 1261-1281, 2009.

[131] S. Foster, T. Htut and T. Ng, "High performance fibre reinforced concrete: fundamental behaviour and modelling," in *Proceedings of the 8th International Conference on Fracture Mechanics Concrete and Concrete Structures (FraMCoS-8)*, Toledo, Spain, 2013.

[132] J. Y. L. Voo and S. J. Foster, "Tensile fracture of fibre reinforced concrete: variable engagement model," in *Proceedings of 6th Rilem Symposium on Fibre-reinforced Concrete (FRC)*, Varenna, Italy, 2004.

[133] G. G. Lee and S. J. Foster, "Modelling of shear-fracture of fibre reinforced concrete," in *International fib Symposium*, 2008.

[134] T. S. Ng, T. N. S. Htut and S. J. Foster, "UNICIV report R-460: Fracture of steel fibre-reinforced concrete – the unified variable engagement model," School of Civil & Environmental Engineering, Univeristy of New South Wales, Sydney, Australia, 2012.

[135] A. Amin, S. J. Foster and A. Muttoni, "Derivation of the σ-w relationship for SFRC from prism bending tests," *Structural Concrete,* vol. 16, no. 1, pp. 93-106, 2015.

[136] S. C. Lee, J. Cho and F. J. Vecchio, "Diverse embedment model for steel fibre-reinforced concrete in tension: model development," *ACI Materials Journal,* vol. 108, no. 5, pp. 516-525, 2011.

[137] E. 1990:2002, "Eurocode: Basis of Structural Design," CEN, Brussels, 2001.

Appendix A - Experimental data – material characterization

A.1. Raw compressive strength data

A.1.1. M1-2S

Table A. 1 Compressive strength results M1-2S

Specimen No.	1	2	3
D_1 (mm)	99.8	100.1	99.8
D_2 (mm)	99.6	99.8	100.0
D_3 (mm)	99.4	100.0	100.0
D_{avg} (mm)	99.6	100.0	99.9
Area (mm^2)	7793.4	7846.7	7843.5
Height (mm)	196.4	197.1	200.0
Mass (g)	3678.0	3711.0	3693.0
Max Load (kN)	1325.0	1320.0	1325.0
Density (kg/m^3)	2403	2400	2354
Strength (MPa)	170.0	168.2	168.9
Mean Compressive Strength (MPa)		**169.1**	

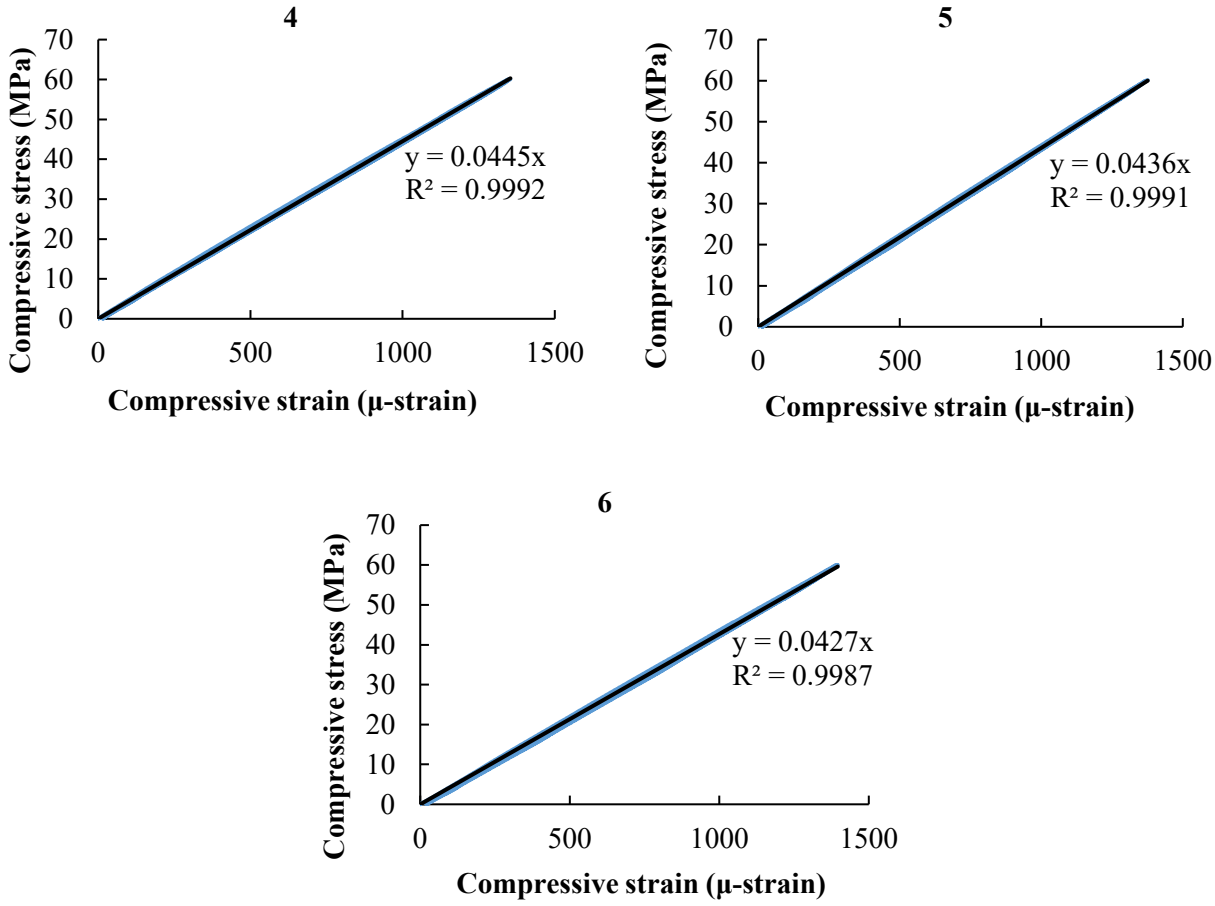

Figure A.1 Compressive stress-strain curve M1-2S

Table A. 2 Young's modulus results M1-2S

Specimen	Young's modulus, *E* (GPa)
4	44.5
5	43.6
6	42.7
Mean	**43.6**

A.1.2. M2-3S

Table A.3 Compressive strength results M2-3S

Specimen No.	C1	C2	C3
D_{avg} (mm)	99.6	99.9	99.5
Area (mm^2)	7791.3	7838.3	7775.6
Height (mm)	201.6	196.5	199.5
Mass (g)	3856.8	3763.2	3804.8
Max Load (kN)	1418.2	1382.5	1356.9
Density (kg/m^3)	2455	2443	2453
Strength (MPa)	182.0	176.4	174.5
Mean Compressive Strength (MPa)		**177.6**	

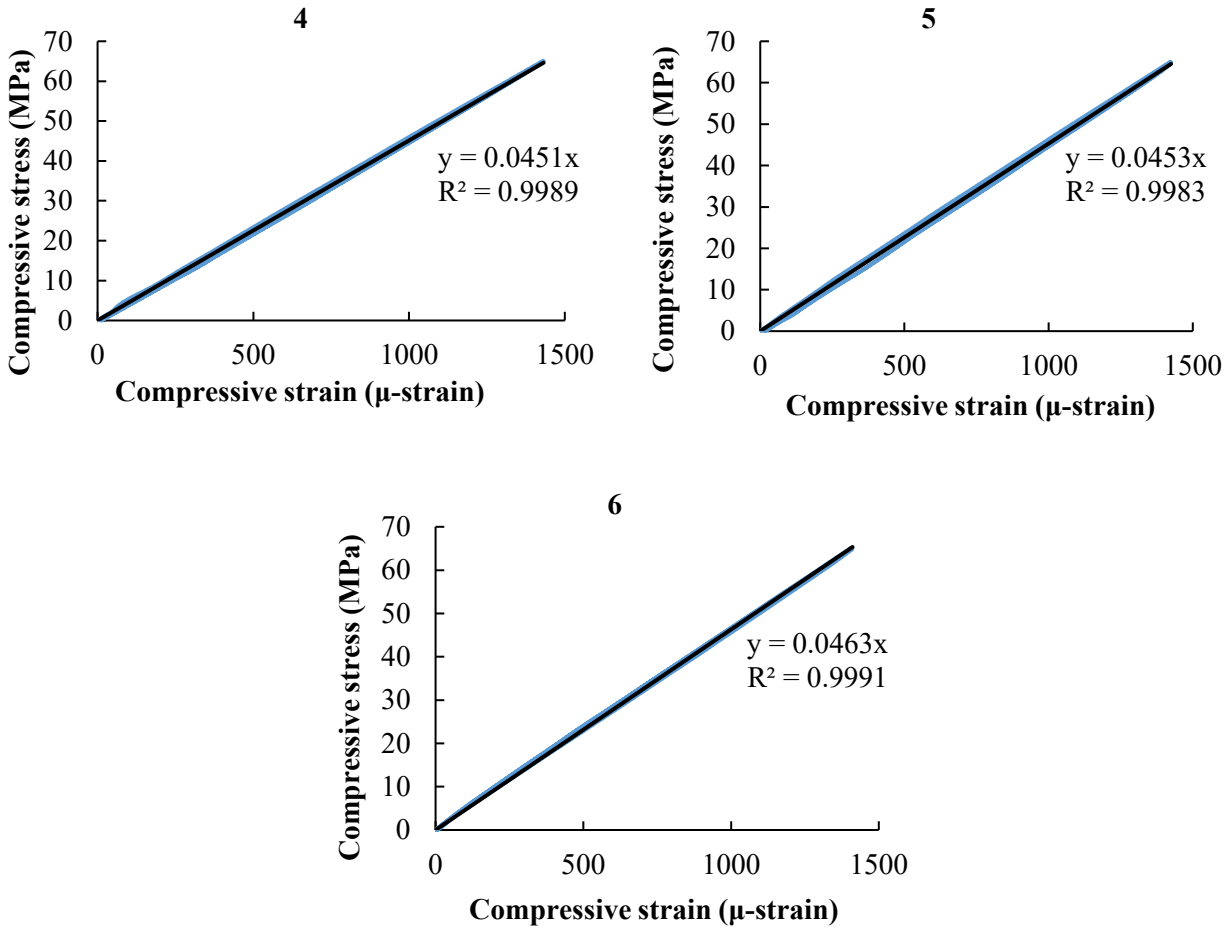

Figure A.2 Compressive stress-strain curve M2-3S

Table A.4 Young's modulus results M2-3S

Specimen	Young's modulus, *E* (GPa)
4	45.1
5	45.3
6	46.3
Mean	**45.6**

A.1.3. M3-1DEH

Table A.5 Compressive strength results M3-1DEH

Specimen No.	C1	C2	C3
D_{avg} (mm)	100	100.5	100.3
Area (mm^2)	7854.0	7932.7	7901.2
Height (mm)	198.9	196.9	199.3
Mass (g)	3656.2	3704.2	3711
Max Load (kN)	1058.7	1182.0	1143.1
Density (kg/m^3)	2340	2372	2357
Strength (MPa)	134.8	149.0	144.7
Mean Compressive Strength (MPa)		**142.8**	

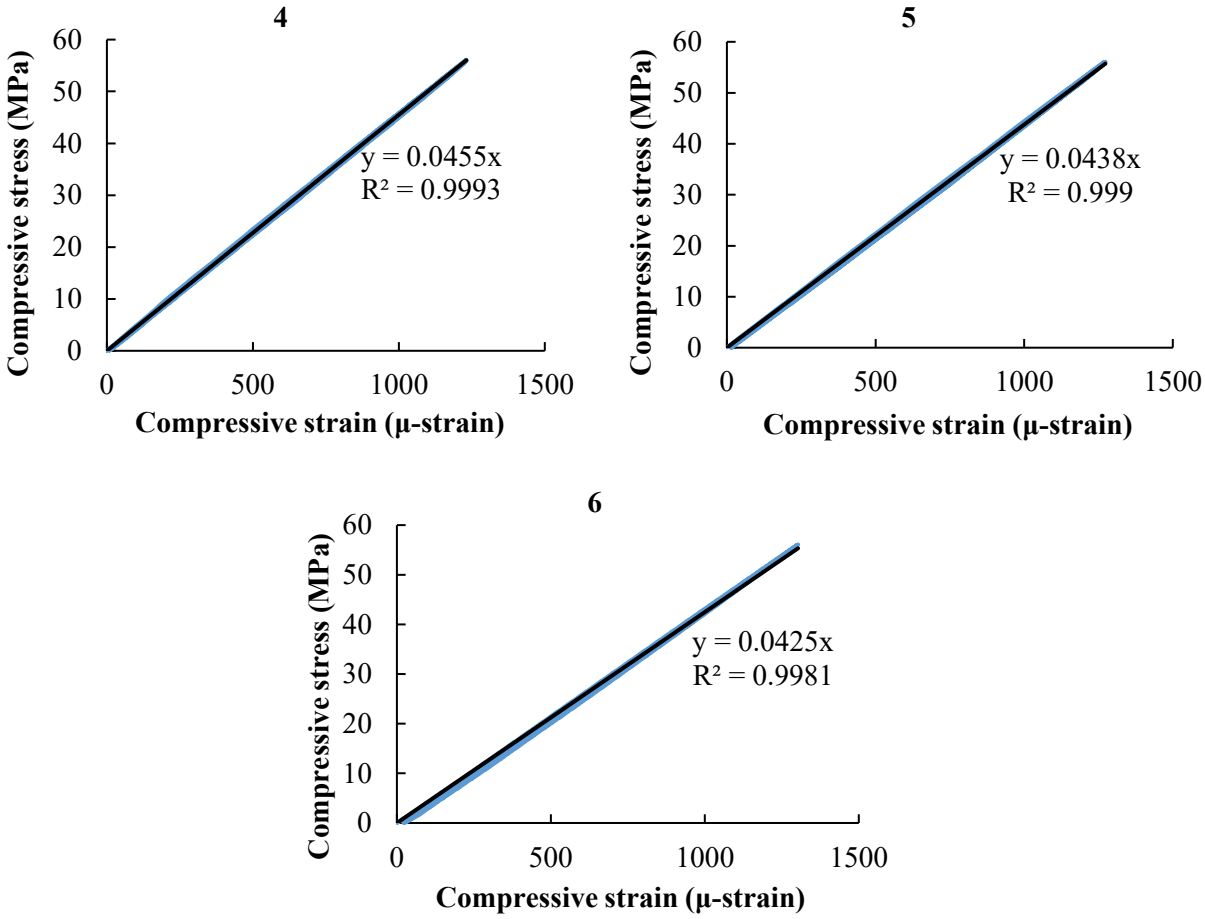

Figure A.3 Compressive stress-strain curve M3-1DEH

Table A.6 Young's modulus results M3-1DEH

Specimen	Young's modulus, *E* (GPa)
4	45.5
5	43.8
6	42.5
Mean	**43.9**

A.1.4. M4-2EH/S2

Table A.7 Compressive strength results M4-2EH/S2

Specimen No.	C1	C2	C3
D_{avg} (mm)	99.87	99.77	100.07
Area (mm2)	7833.6	7817.9	7864.9
Height (mm)	195.7	197.1	198.9
Mass (g)	3609	3623	3667
Max Load (kN)	1210	1220	1225
Density (kg/m^3)	2354	2351	2344
Strength (MPa)	154.5	156.1	155.8
Mean Compressive Strength (MPa)		**155.4**	

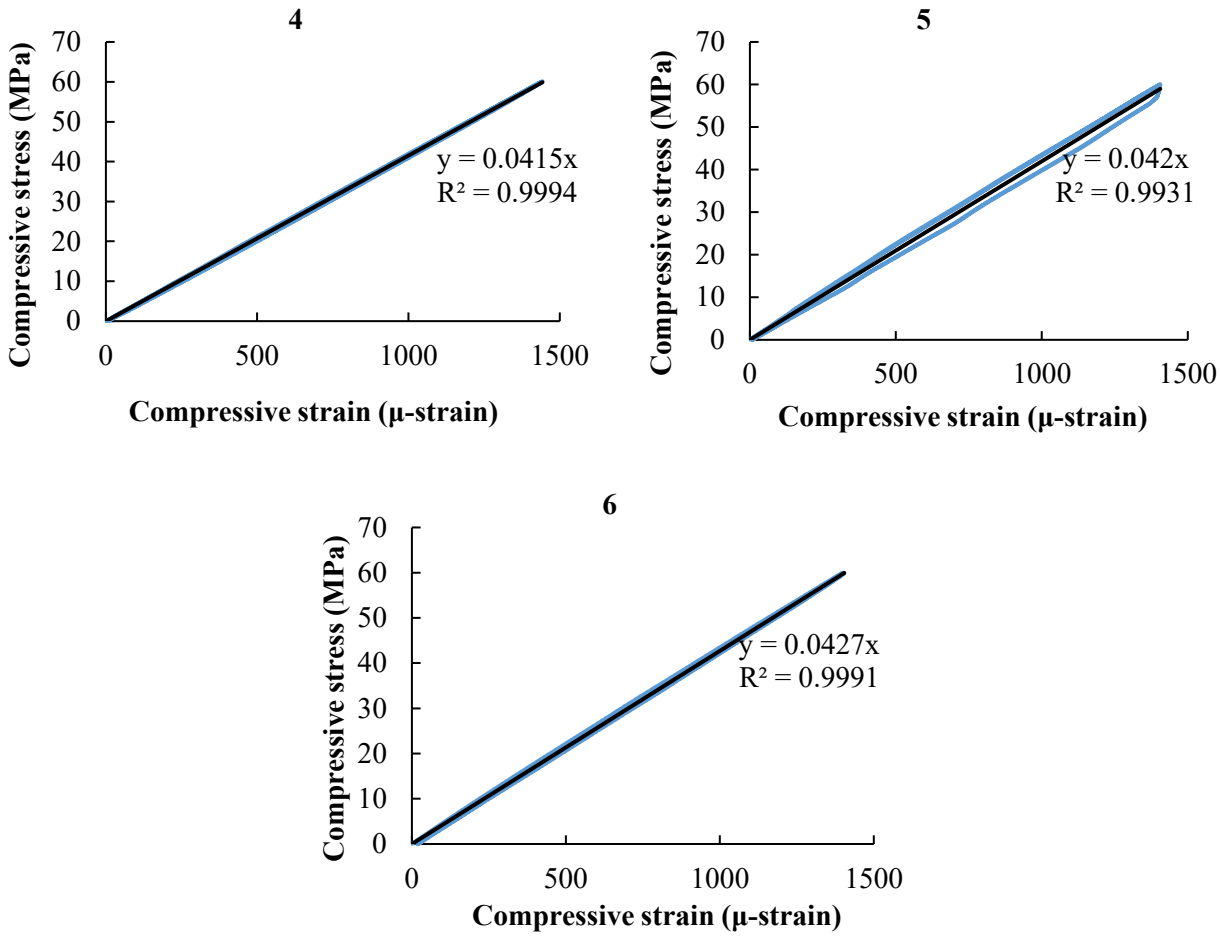

Figure A.4 Compressive stress-strain curve M4-2EH/S2

Table A.8 Young's modulus results M4-2EH/S2

Specimen	Young's modulus, *E* (GPa)
4	41.5
5	42.0
6	42.7
Mean	**42.1**

A.1.5. M5-2EH/S

Table A.9 Compressive strength results M5-2EH/S

Specimen No.	C1	C2	C3
D_{avg} (mm)	99.6	99.5	99.4
Area (mm^2)	7791.3	7775.6	7760.0
Height (mm)	199.8	199.2	198.6
Mass (g)	3720	3719	3691
Max Load (kN)	1345.0	1320.0	1280.0
Density (kg/m^3)	2389.7	2401.0	2395.0
Strength (MPa)	172.6	169.8	164.9
Mean Compressive Strength (MPa)		**169.1**	

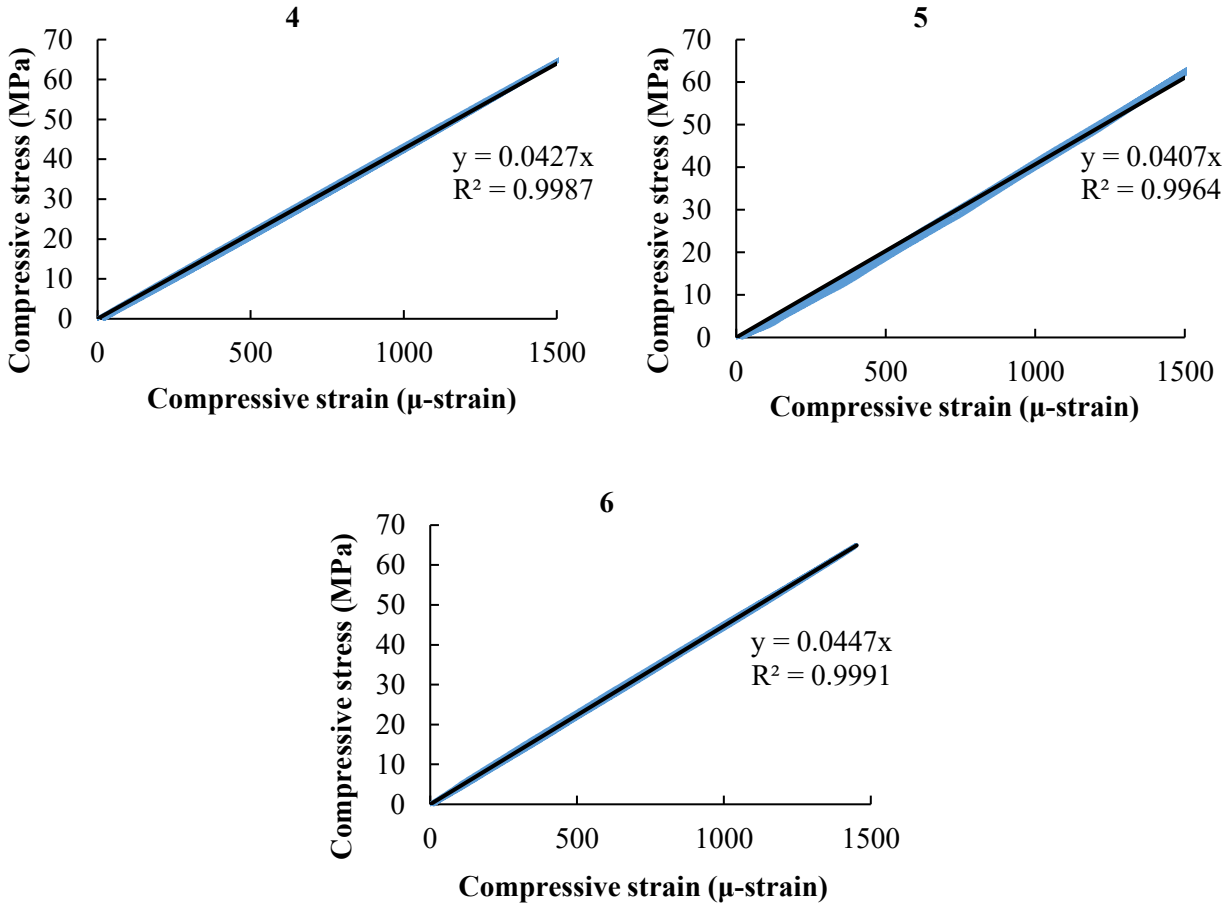

Figure A.5 Compressive stress-strain curve M5-2EH/S

Table A. 10 Young's modulus results M5-2EH/S

Specimen	Young's modulus, *E* (GPa)
4	42.7
5	40.7
6	44.7
Mean	**42.7**

A.2. LSCT and LVDT readings from uniaxial tests at w = 1.5mm

Table A.11 LSCT and LVDT readings from uniaxial tests at w = 1.5mm

Mix	Specimen No.	North LSCT-7 (mm)	South LSCT-8 (mm)	East LVDT-1 (mm)	West LVDT-2 (mm)	Out-of-plane rotations* (rad)	In-plane rotations** (rad)
M1-2S	DB1	0.00	3.52	1.57	1.60	-0.03357	-0.00017
	DB2	0.76	2.44	1.30	1.84	-0.01602	-0.00300
M2-3S	DB1	1.51	1.55	1.54	-	-0.00036	-
	DB2	1.02	2.81	1.79	-	-0.01709	-
	DB3	1.76	1.77	1.71	-	-0.00010	-
M3-1DEH	DB1	2.09	1.06	-	-	0.00977	-
	DB2	1.17	1.81	1.75	1.35	-0.00609	0.00222
	DB3	-	-	-	-	-	-
M4-2EH/S2	DB1	4.71	0.62	2.37	2.58	0.03889	-0.00117
	DB2	1.30	3.86	2.00	3.13	-0.02441	-0.00627
M5-2EH/S	DB1	-	-	0.32	2.89	-	-0.01428
	DB2	-	-	3.08	2.96	-	0.00065

* The horizontal distance between LVDT-1 and LVDT-2 is 180 mm

** The horizontal distance between LSCT-7 and LSCT-8 is 105 mm